MULTIMODAL STATISTICAL ANALYSIS OF BRAIN CONNECTOME WITH APPLICATION TO ALZHEIMER'S DISEASE

by

Demet Yüksel Dal

B.S., Electrical & Electronics Engineering, Bahçeşehir University, 2009

M.S., Electrical & Electronics Engineering, Boğaziçi University, 2014

Submitted to the Institute for Graduate Studies in
Science and Engineering in partial fulfillment of
the requirements for the degree of
Master of Science

Graduate Program in Electrical & Electronics Engineering

Boğaziçi University

2024

ACKNOWLEDGEMENTS

First and foremost, I would like to express my deepest gratitude to my advisor, Prof. Dr. Burak Acar, for their invaluable guidance, encouragement, and expertise throughout my research journey. Their patience and insightful feedback have been instrumental in shaping both my thesis and my academic growth.

I am deeply grateful to Doç. Dr. Alkan Kabakçıoğlu for his constructive feedback, valuable discussions, and role as a member of my thesis committee. I also extend my sincere thanks to Prof. Dr. Murat Saraçlar and Prof. Dr. Arzucan Özgur for their insightful comments, time, and dedication as committee members. Their expertise and support have been essential to the successful completion of this research.

I extend my heartfelt thanks to my colleagues and friends in the Volumetric Analysis & Visualization Group (VAVlab) for their unwavering support and for creating a collaborative and inspiring environment. I am especially grateful to Abdülkadir Yazıcı and Göktekin Durusoy for their insightful discussions, feedback, and friendship. I would also like to express my sincere gratitude to Kaan Ege Özgün, Abdullah Karaaslanlı, Zeynep Kahraman, Fatih Soğukpınar, and Dr. Okan İrfanoğlu for their invaluable contributions to preprocessing and the BraiNet application, and to Gurur Gamgam and Güneş Bayır for bringing a machine learning perspective to this work.

I acknowledge my deep sense of gratitude and indebtedness to all researchers who take part in the VAVlab BRAINet project at Istanbul Faculty of Medicine, Istanbul University. Their collaborative efforts made this thesis possible. Among them, I would like to thank especially Prof. Hakan Gürvit, and Zerrin Yıldırım for their contributions to the neurological discussions in this thesis. I would like to thank Tamer Demiralp, Haşmet Hanağası, Bedia Samancı, Çiğdem Ulaşoğlu-Yıldız, Elif Kurt, Erhan Özacar, Evren Özarslan, Aslı Demirtaş-Tatlıdede and Başar Bilgiç for their contributions in data collection and clinical assessment.

I wish to express my deepest gratitude to my parents, Halil and Gülnaz Yüksel, for their unwavering support, boundless love, and encouragement throughout my life. I am also immensely thankful to my siblings—Mehmet Edip and Şeyma Yüksel, Fatma and Ahmet Kuran, Elif and Cenk Kalava, İbrahim and Burcu Yüksel, Emine Yüksel, Şeyma Yüksel, and İsmail Yüksel—for their endless support and all they have done.

Last but certainly not least, I would like to thank my beloved partner, Bulut Rahmi Dal, for his unwavering moral and emotional support, and his patience with my countless hours of solitude devoted to this thesis. A warm embrace to my children, Ece and Ali, whose presence brought both joy and delightful interruptions to my work. To my dear family, who brought joy during the most challenging times, even as we faced immense difficulties together throughout this long journey.

This work was in part supported by the Turkish Directorate of Strategy and Budget under the TAM Project number 2007K12-873, TÜBİTAK-ARDEB 1003 Programme under Grant #114E053, Bogazici University Research Fund Grant #16862.

ABSTRACT

MULTIMODAL STATISTICAL ANALYSIS OF BRAIN CONNECTOME WITH APPLICATION TO ALZHEIMER'S DISEASE

Clinical cognitive decline, often culminating in Alzheimer's Disease Dementia (ADD), has traditionally been viewed as a disconnection syndrome affecting the brain's structural and functional organization. Despite extensive research focusing on changes in brain connectome models, particularly in the functional domain, a coherent understanding of underlying mechanisms and robust biomarkers remains elusive. Evidence suggests that the brain undergoes spatially non-stationary and non-monotonous structural and functional changes across the clinical decline continuum. In this thesis, these changes across different stages of clinical cognitive decline were examined in the context of local structural and functional reorganization in the brain. For this purpose, nodal assortativity was used as a quantitative metric. The findings reveal statistically significant local reorganization patterns in both structural and functional domains, which transition with the progression of cognitive decline and differ in nature between structure and function. Specifically, hypo-assortativity tends to prevail in the initial phases for both structural and functional aspects, transitioning to hyper-assortativity in later stages. Notably, functional reorganization is more pronounced in the early stages, while structural reorganization becomes prominent later. Despite some common regions that undergo both structural and functional reorganization, a significant variation was observed in regions affected from functional and structural perspectives. It is underscored that analyzing both spatial and temporal dimensions is crucial for a comprehensive understanding of clinical cognitive decline leading to ADD. The preliminary findings suggest a complex and variable reorganization process, potentially indicative of simultaneous active degenerative and compensatory mechanisms.

ÖZET

ALZHEİMER HASTALIĞINA UYGULANAN BEYİN KONNEKTOMUNUN ÇOK MODLU İSTATISTİKSEL ANALİZİ

Genellikle Alzheimer Hastalığı Demansı (AHD) ile sonuçlanan klinik bilişsel gerileme beyin yapısının ve işlevselliğinin etkilendiği bir bağlantı kopukluğu sendromu olarak kabul edilmektedir. Özellikle işlevsel alanda, beyin konnektom modellerindeki değişikliklere odaklanan kapsamlı araştırmalara rağmen, altta yatan mekanizmaların ve sağlam biyobelirteçlerin anlaşılması konusunda tutarlı bir anlayış hâlâ eksik kalmaktadır. Kanıtlar, beynin klinik gerileme sürecinde mekansal olarak durağan ve monoton olmayan yapısal ve işlevsel değişikliklerden geçtiğini göstermektedir. Bu tezde, beyin yapısı ve işlevselliğindeki değişikliklerin klinik bilişsel gerileme ile ilişkisi düğümsel assortativite kullanılarak incelenmiştir. Bulgular, hastalığın ilerlemesiyle birlikte beynin lokal yeniden organizasyonunda önemli değişiklikler olduğunu ortaya koymuştur. Bu modeller, bilişsel gerilemenin ilerlemesiyle değişmekle kalmayıp, beynin doğası gereği yapısal ve işlevsel olarak da farklılık göstermektedir. Özellikle, yapısal ve işlevsel beyin ağlarında erken evrelerde hipo-assortativite yaygınken, sonraki evrelerde hiper-assortativiteye geçiş gözlenmektedir. İşlevsel yeniden organizasyon erken aşamalarda gözlemlenirken, yapısal yeniden organizasyon daha sonraki aşamalarda gözlemlenmiştir. Yapısal ve işlevsel yeniden organizasyona uğrayan bazı ortak bölgeler bulunmakla birlikte, işlevsel ve yapısal açıdan etkilenen bölgelerde belirgin farklılıklar gözlemlenmiştir. Bu çalışma, AHD'ye yol açan klinik bilişsel gerilemeyi tam anlamıyla anlamak için hem mekânsal hem de zamansal boyutların analiz edilmesinin kritik olduğu vurgulanmaktadır. Özetle, bu çalışmanın öncül bulguları, karmaşık ve değişken bir yeniden organizasyon sürecini işaret etmekte olup, muhtemelen eş zamanlı aktif dejeneratif ve telafi edici mekanizmaların varlığını göstermektedir.

TABLE OF CONTENTS

ACKNOWLEDGEMENTS iii
ABSTRACT v
ÖZET vi
LIST OF FIGURES ix
LIST OF TABLES xv
LIST OF SYMBOLS xvi
LIST OF ACRONYMS/ABBREVIATIONS xviii
1. INTRODUCTION 1
2. LITERATURE REVIEW AND CONTRIBUTION 5
2.1. Brain Network as a Graph 7
2.2. Global and Nodal (Local) Network Measures 9
2.3. Applications of Network Measures to Brain Connectomes in Alzheimer's Disease Dementia Research 11
2.3.1. Structural Networks 11
2.3.2. Functional Networks 12
2.4. Applications of Local Brain Connectome Measures in Alzheimer's Disease Dementia 14
2.5. Contribution of The Thesis 15
3. METHODOLOGY 17
3.1. Brain Connectome Construction 17
3.1.1. Data Preprocessing 19
3.1.2. Connectome Node Definition 23
3.1.3. Structural Networks 24
3.1.4. Functional Networks 29
3.2. Brain Connectome Measures 31
3.2.1. Basic Measures 33
3.2.2. Measures of Segregation 34
3.2.3. Measures of Centrality 34

3.2.4. Measures of Resilience 35
3.3. Statistical Anaylsis 36
3.3.1. Hypothesis Testing and Feature Selection 37
3.3.2. Classification, Validation, and Robustness Assessment 38
4. EXPERIMENTS 40
4.1. Data 40
4.1.1. Cohort and Clinical Assessment 40
4.1.2. Data Acquisition 41
4.2. Multi-scale Analysis 42
4.2.1. Global (Complete Network) Scale 44
4.2.2. Mesoscale (Subnetwork) Scale 46
4.2.3. Local (Nodal) Scale 48
4.3. Measurements Analysis 49
4.3.1. Nodal Degree 50
4.3.2. Nodal Strength 54
4.3.3. Nodal Clustering Coefficient 59
4.3.4. Nodal Betweenness Centrality 64
4.3.5. Nodal Assortativity 69
4.4. Global and Nodal Network Measures as a Diagnostic Biomarker 74
5. DISCUSSION 78
6. CONCLUSION 85
REFERENCES 88
APPENDIX A: AGE EFFECTS ON NODAL ASSORTATIVITY ACROSS COGNITIVE STAGES 101

LIST OF FIGURES

Figure 1.1. Pathological Changes of Alzheimer's Disease [7]. 3

Figure 2.1. Brain network visualization using BrainNet-viewer tool [13]. 8

Figure 3.1. The analysis pipeline is composed of data collection, connectome construction, characterization, feature computation, feature selection, and classifier training/testing [37]. $r_{(i)}$ refers to the node ID with importance ranking i and $p_{r_{(i)}}$ is the corresponding p-value computed by t-test. 18

Figure 3.2. Preprocessing Pipeline [39]. The utilization of the Tortoise, FreeSurfer, and FSL programs is depicted by red, purple, and blue boxes, respectively. Parc refers to the Schaefer-400 Atlas parcellation. . . . 19

Figure 3.3. Pre-FreeSurfer Pipeline Block Diagram [43]. 20

Figure 3.4. FreeSurfer pipeline block diagram [43]. 21

Figure 3.5. Graph measures. The yellow node indicates a high degree (a hub for local communication), the red node indicates high betweenness centrality (a bridge for information flow), and the green node indicates a high clustering coefficient (local cluster formation). (b) The blue node represents disassortative connections, while the maroon node represents assortative connections. 32

Figure 4.1. Distributions of global assortativity coefficients (r) of (A) sNETs, and (B) fNETs in each group for Schaefer 200. sNETs show assortative structure, while fNETs are primarily disassortative. sNETs did not differ significantly between SCI and MCI ($p > 0.248$), but differed significantly between MCI and ADD ($p = 0.021$). For fNETs, no significant differences are observed across stages ($p > 0.83$). . . 44

Figure 4.2. Distributions of global assortativity coefficients (r) of (A) sNETs, and (B) fNETs in the ADD, MCI and SCI groups for Schaefer 400. sNETs show assortative structure, while fNETs are primarily disassortative. There is no statistically significant difference between different stages of clinical cognitive decline ($p > 0.291$). 45

Figure 4.3. Distributions of global assortativity coefficients (r) of (A) sNETs, and (B) fNETs in the ADD, MCI and SCI groups for Schaefer 800. sNETs show assortative structure, while fNETs are primarily disassortative, with no significant differences across cognitive decline stages ($p > 0.054$). 45

Figure 4.4. Differential nodal degree maps of the statistically significant sNET and fNET locations for SCI-vs-MCI (1st and 3rd row) and MCI-vs-ADD (2nd and 4th row) discrimination, displayed from lateral/medial views of right/left hemispheres, respectively, on inflated brain surface (BrainSurfer) [74]. Cortical regions with statistically significant degree increases/decreases are shown in red/blue, respectively. 50

Figure 4.5. Distributions of the nodal degree of the top 5 most discriminative sNET nodes are shown for SCI-vs-MCI ($p < 0.011$) at the top panel and for MCI-vs-ADD ($p < 0.001$) at the bottom panel. A significant nodal degree increase is observed in the transition from SCI to MCI. In contrast, a statistically significant decrease is observed in the transition from MCI to ADD. 52

Figure 4.6. Distributions of the nodal degree of the top 5 most discriminative fNET nodes are shown for SCI-vs-MCI ($p < 0.011$) at the top panel and for MCI-vs-ADD ($p < 0.003$) at the bottom panel. A significant nodal degree increase is observed in the transition from SCI to MCI and MCI to ADD, albeit at mutually exclusive sets of nodes (cortical regions). 53

Figure 4.7. Differential nodal strength maps of the statistically significant sNET locations for SCI-vs-MCI (1st row), MCI-vs-ADD (2nd row) discrimination and fNET locations for SCI-vs-MCI (3rd row), MCI-vs-ADD (4th row) discrimination. The cortical regions with a statistically significant increase/ decrease in strength with increasing cognitive decline are depicted in red/blue, respectively. 55

Figure 4.8. Distributions of nodal strength of the top 5 most discriminative sNET nodes are shown for SCI-vs-MCI ($p < 0.001$) at the top panel and for MCI-vs-ADD ($p < 0.008$) at the bottom panel. A statistically significant increase in nodal strength is observed in the transition from SCI to MCI. In contrast, a statistically significant decrease is observed in the transition from MCI to ADD. 57

Figure 4.9. Distributions of nodal strength of the top 5 most discriminative fNET nodes are shown for SCI-vs-MCI ($p < 0.006$) at the top panel and for MCI-vs-ADD ($p < 0.001$) at the bottom panel. A statistically significant increase in nodal strength is observed throughout the disease progression in fNET, albeit at mutually exclusive sets of nodes (cortical regions). 58

Figure 4.10. Differential nodal clustering coefficient maps of the statistically significant sNET locations for SCI-vs-MCI (1st row), MCI-vs-ADD (2nd row) discrimination and fNET locations for SCI-vs-MCI (3rd row), MCI-vs-ADD (4th row) discrimination. In the SCI-to-MCI transition, sNET shows substantial clustering changes with 36 significant nodes, while fNET has limited changes. 60

Figure 4.11. Distributions of nodal clustering coefficient of the top 5 most discriminative sNET nodes are shown for SCI-vs-MCI ($p < 0.011$) at the top panel and for MCI-vs-ADD ($p < 0.009$) at the bottom panel. A statistically significant increase in the nodal clustering coefficient is observed during the SCI to MCI transition, while a decrease is observed during the MCI to ADD transition. 62

Figure 4.12. Distributions of nodal clustering coefficient of the top 5 most discriminative fNET nodes are shown for SCI-vs-MCI ($p < 0.031$) at the top panel and for MCI-vs-ADD ($p < 0.003$) at the bottom panel. A statistically significant increase in nodal clustering coefficient is observed in the transition from SCI to MCI, and MCI to ADD, albeit at mutually exclusive sets of nodes. 63

Figure 4.13. Differential nodal betweenness centrality maps of the statistically significant sNET and fNET locations for SCI-vs-MCI (1st and 3rd row) and MCI-vs-ADD (2nd and 4th row) discrimination, respectively. Betweenness centrality increases in 36 sNET and 19 fNET significant nodes during the early disease stage, but decreases in 39 sNET and 12 fNET significant nodes during the later stage. 65

Figure 4.14. Distributions of nodal betweenness centrality of the top 5 most discriminative sNET nodes are shown for SCI-vs-MCI ($p < 0.02$) at the top panel and for MCI-vs-ADD ($p < 0.001$) at the bottom panel. A statistically significant increase in nodal clustering coefficient is observed in the transition from SCI to MCI, while a statistically significant decrease is observed in the transition from MCI to ADD. 67

Figure 4.15. Distributions of nodal betweenness centrality of the top 5 most discriminative fNET nodes are shown for SCI-vs-MCI ($p < 0.001$) and MCI-vs-ADD ($p < 0.01$), respectively. There is no consistent increase or decrease in nodal betweenness centrality during the SCI to MCI transition, while a statistically significant decrease is observed during the MCI to ADD transition, except one node. 68

Figure 4.16. Differential nodal assortativity maps of the statistically significant sNET and fNET locations for SCI-vs-MCI (1st and 3rd row) and MCI-vs-ADD (2nd and 4th row) discrimination, respectively. In general, nodal assortativity decreases early in cognitive decline, reflecting vulnerability, but increases later, indicating enhanced local connectivity and resilience. 71

Figure 4.17. Distributions of nodal assortativity coefficients of the top 5 most discriminative sNET nodes are shown for SCI-vs-MCI ($p < 0.018$) at the top panel and for MCI-vs-ADD ($p < 0.004$) at the bottom panel. A statistically significant decrease in nodal assortativity is observed in the transition from SCI to MCI, while a statistically significant increase is observed in the transition from MCI to ADD. 72

Figure 4.18. Distributions of nodal assortativity coefficients of the top 5 most discriminative fNET nodes are shown for SCI-vs-MCI ($p < 0.002$) at the top panel and for MCI-vs-ADD ($p < 0.012$) at the bottom panel. A statistically significant decrease in nodal assortativities is observed in the transition from SCI to MCI, while a statistically significant increase is observed in the transition from MCI to ADD. 73

LIST OF TABLES

Table 4.1. Summary of the cohort of participants. 40

Table 4.2. P-values and AUCs for assortativity of Yeo's 7 subnetworks sNETs and fNETs across the cognitive decline spectrum at 200, 400, and 800 scales. 47

Table 4.3. Classification accuracies for different disease stages (SCI-MCI, MCI-ADD) and spatial scales of the Schaefer atlas (200, 400, and 800). The accuracies of linear SVM classifiers computed over leave-one-out experiments for SCI-vs-MCI and MCI-vs-ADD tasks on sNETs and fNETs, using $5D$ feature vectors composed of nodal assortativity of the statistically most significant nodes. 49

Table 4.4. Linear SVM accuracies were computed for SCI-vs-MCI, MCI-vs-ADD, and SCI-vs-ADD tasks on sNETs and fNETs using $5D$ (specific node features) and $400 - D$ (full connectome) feature vectors (Nodal Assortativity/NA, Clustering Coefficient/CC, Betweenness Centrality/BC, Node Strength/NS, Node Degree/ND). † Results of random shuffling experiments are reported only for nodal assortativity. 76

Table A.1. Linear regression and Pearson's correlation analysis results for the relationship between age and assortativity in sNET and fNET, comparing SCI vs MCI and MCI vs ADD. 101

LIST OF SYMBOLS

$\mathbf{A}$	Adjacency Matrix
a_{ij}	The binarized form of w_{ij}
B_i	Betweenness centrality of node i
C_i	Clustering coefficient of node i
$\mathbf{D}$	Diffusion tensor matrix
d_i	Degree of node i
$\mathbf{E}$	Eigenvector matrix
e_1	The direction of the principal diffusion
e_k	End point of the kth fiber
$\mathbf{G_m^{s/f}}$	Undirected sNET or fNET at scale m
$\mathbf{L_m^{s/f}}$	Sets of links in sNET or fNET at scale m
N	Number of nodes in a network
$\mathbf{N_m^{s/f}}$	Sets of nodes in sNET or fNET at scale m
P_i	i^{th} parcel in brain
R^2	Coefficient of determination
r	Global assortativity
r_i	Local assortativity
s_i	Strength of node i
T_i	Number of triangles associated with a node i
V_i	Volume of parcel P_i
w_{ij}	Weight of the connection between nodes i and j
W_{ik}	Association between i^{th} parcel and k^{th} fiber
x_j	j^{th} voxel position
α	Coefficients of the predictor variables in the model
δ_i	The mean difference between the degree of a node and those of its neighbors

γ	Controls the balance between L1 (Lasso) and L2 (Ridge) penalties
$\mathbf{\Gamma_{st}}$	The set of all possible paths between nodes s and t
λ_1	The maximum eigenvalue derived from the diffusion tensor
$\hat{\rho_{ij}}$	Partial correlation coefficients
θ_i	The weight associated with the observation x_i

LIST OF ACRONYMS/ABBREVIATIONS

3D	Three Dimensional
$400-D$	400 Dimensional
$5-D$	Five Dimensional
$A\beta$	Amyloid-Beta
AAL	Automated Anatomical Labeling
AC	Anterior Commissure
ADD	Alzheimer's Disease Dementia
AHD	Alzheimer Hastalığı Demansı
BBR	Boundary-Based Registration
BCT	Brain Connectivity Toolbox
BC	Betweenness Centrality
BOLD	Blood Oxygenation Level-Dependent
CC	Clustering Coefficient
CON	Control Network
CSF	Cerebrospinal Fluid
DAN	Dorsal Attention Network
DMN	Default Mode Network
dMRI	Diffusion Magnetic Resonance Imaging
DWI	Diffusion-Weighted Imaging
DTI	Diffusion Tensor Imaging
FA	Fractional Anisotropy
fMRI	Functional Magnetic Resonance Imaging
fNET	Functional Network
HC	Healthy Control
HCP	Human Connectome Project
LOOCV	Leave-One-Out Cross-Validation
MCI	Mild Cognitive Impairment
MRI	Magnetic Resonance Imaging

ND	Node Degree
NS	Node Strength
PC	Posterior Commissure
pCunPCC	Precuneus Posterior Cingulate Cortex
PDD	Principal Diffusion Direction
PET	Positron Emission Tomography
PFCl	Lateral Prefrontal Cortex
RK4	4th order Runge-Kutta
ROI	Regions of Interest
rs-fMRI	Resting-State Functional Magnetic Resonance Imaging
SCI	Subjective Cognitive Impairment
SMN	Somatomotor Network
sNET	Structural Network
SVD	Singular Value Decomposition
SVD-RG	Singular Value Decomposition Region Growing
SVN	Salience/Ventral Attention Network
SVM	Support Vector Machine
T1w	T1-weighted
T2w	T2-weighted
VN	Visual Network
WHO	World Health Organization

1. INTRODUCTION

According to the World Health Organization (WHO), the worldwide population of individuals affected by dementia is expected to grow from 55 million in 2019 to 139 million by 2050 [1]. ADD constitutes $60 - 80\%$ of all dementia cases, resulting in substantial economic and social challenges [1, 2].

The economic challenges arise due to the high costs of care and treatment of ADD, creating a substantial burden. According to the National Alzheimer's Association, the estimated per-person costs are $\$52,481$ in the United States [2]. It is also reported the average Medicare payments for individuals aged 65 and older with ADD is nearly three times higher than payments for beneficiaries without these conditions, and Medicaid payments are over 22 times higher. It is estimated that the total costs for healthcare, long-term care, and hospice services for people aged 65 and older with dementia in 2024 will reach \$360 billion. Although no cure has been found to reverse this degeneration, it is widely accepted that lifestyle has a significant impact on the pace of progress in dementia, if not prevent it [1]. Hence, prognosis and early diagnosis of ADD can facilitate timely intervention to lifestyle choices easing the aforementioned burden on society and individuals. Furthermore, it would enable assessing the outcome of clinical trials of novel treatments by monitoring the progress of cognitive decline.

Additionally, ADD is a significant global health issue with high mortality rates. According to Nichols et al., dementia, including ADD, was reported as the fifth leading cause of death globally in 2016 [3]. Similarly, Conceiccao et al. also emphasized that ADD was the fifth leading cause of death globally in 2018 [4].

In light of the substantial economic burden and worldwide implications of ADD, it is essential to comprehend the complex neural connections in the brain that play a vital role in cognitive functions. With approximately 100 billion neurons and 100 trillion synapses, the healthy adult brain enables the transmission of signals crucial for

various cognitive abilities including memory, thinking, perception, emotions, physical movements, and skills.

ADD is a type of brain disorder that arises due to gradual degradation and loss of neurons [5]. These pathological changes have been observed together with the accumulation of tau protein extracellular neurofibrillary tangles and of intracellular amyloid beta ($A\beta$) protein plaques [6]. Figure 1.1 demonstrates the structural differences between a normal brain and a brain affected by ADD [7]. In a normal brain (Figure 1.1a), the cerebral cortex and hippocampus remain intact, and neurons are healthy. However, in an ADD brain (Figure 1.1b), there is notable shrinkage of the cerebral cortex and hippocampus, enlarged ventricles, and the presence of pathological changes such as tau neurofibrillary tangles and $A\beta$ plaques. They lead to increasing cognitive decline across the spectrum of dementia. Neurologists indicate that pathological alterations begin 20 years or more before the preclinical stage such as memory, language, and thinking problems.

In recent years, advancements in neuroimaging techniques such as magnetic resonance imaging (MRI) and positron emission tomography (PET) have provided unprecedented insights into the complexities of brain connectomes, paving the way for a deeper understanding of neurological disorders, including ADD. Research into brain connectomes is crucial for understanding the mechanism behind the development of ADD. It plays a pivotal role in advancing prognostic capabilities, facilitating early diagnosis, and fostering the development of effective treatment strategies. Integrating multiple imaging modalities, known as multimodal brain connectome analysis, offers a more holistic view of the complex structural and functional changes that occur in the brain during AD progression. To capture the holistic changes in the brain connectome among individuals with Alzheimer's disease, constructing structural (sNET) and functional (fNET) networks using diffusion MRI (dMRI) and functional MRI (fMRI) data is essential.

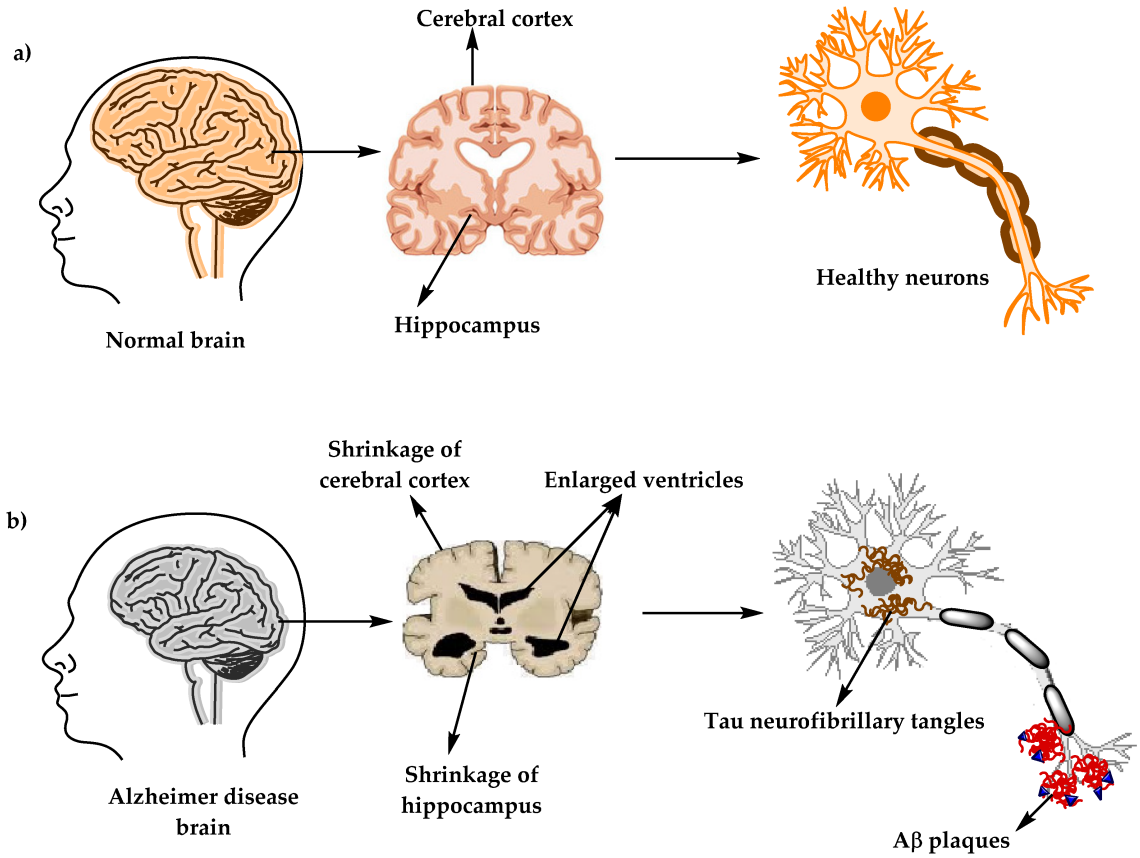

Figure 1.1. Pathological Changes of Alzheimer's Disease [7].

Evidence reported in the literature suggests that ADD is a type of *disconnectivity syndrome* [8, 9]. This syndrome is thought to be consistent with the negative effects of neuronal degeneration and loss in ADD on structural connections between brain regions, potentially leading to the observed disruption in functional relationships/connections. Hence, studying the structural and functional connections of the brain, a.k.a. connectomics, has attracted attention in the research community.

This thesis explores the local topological changes in structural and functional connectivity across the spectrum of clinical cognitive decline. The goal is to offer a spatially and temporally localized perspective to understand the disease progression better and develop effective biomarkers in addition to gaining further insight into the

underpinnings of dementia. In Section 2, a brief literature review contextualizes the studies in the subsequent sections. Section 3 focuses on methodology, which includes the construction of brain connectomes through data preprocessing, node definition, and the generation of structural and functional networks. It is followed by an examination of connectome measures and the statistical analysis process. Section 4 details experiments encompassing cohort, and clinical assessments, data acquisition, statistical analysis of multiple topological and spatial scales, and classification results. Section 5 discusses the results from both neurological and data science perspectives. Section 6 gives the concluding remarks and suggestions for future work.

2. LITERATURE REVIEW AND CONTRIBUTION

The concept of the "connectome" was first introduced in 2005 as a comprehensive representation of neural connections within the brain, and has since become a fundamental framework for comprehending the structural and functional organization of the brain [10]. It plays a crucial role in understanding the structure and function of the brain, offering insights into the intricate network of synaptic connections that form the basis of brain function.

The connectome represents the structural and functional pathways that enable communication between neurons and various brain areas. It encompasses short- and long-range connections, providing a holistic view of how different brain parts are linked. Studying the brain connectome is crucial for understanding neural circuits, information processing, and the basis of various cognitive functions. Advances in neuroimaging techniques, such as dMRI and fMRI, have significantly contributed to mapping and exploring the complexities of the brain connectome.

The human brain is a complex structure in which different regions perform various functions and communicate through specialized pathways known as white matter tracts. Advancements in dMRI techniques, such as tractography, provide maps of the white matter tracts by measuring the movement of water molecules within the brain. This technique offers a more comprehensive understanding of white matter connectivity and related issues through white matter fiber tractography [11].

In contrast to dMRI, fMRI measures changes in blood flow associated with neural activity, offering real-time insights into brain function. This technique has numerous applications, including the investigation of working memory tasks in patients with psychiatric disorders. Studies utilizing fMRI have revealed distinct brain responses, particularly in regions like the default mode network (DMN), during tasks in individuals with schizophrenia and major depressive disorder. Additionally, resting-state fMRI

allows researchers to explore functional connectivity by analyzing the synchronization of neural activity in different brain regions. This technique utilizes the temporal similarity of blood oxygenation level-dependent (BOLD) signals to investigate intrinsic brain networks and functional connectivity patterns [12].

Utilizing multimodal brain connectome analysis with fMRI and dMRI data helps to understand the intricate workings of the brain. This approach permits the exploration of brain connectivity, the relationships between brain structure and function, and alterations associated with various neurological conditions with exceptional detail. By combining these imaging modalities, we can gain a more comprehensive understanding of the intricate workings of the brain, paving the way for advancements in diagnosis, treatment, and our fundamental understanding of human cognition.

The connectome can be effectively modeled as a network, where brain regions represent the nodes and the connections between them represent the edges. A crucial element of the connectome is the connectivity matrix, which depicts the relationships between these nodes within the network. The representation of the structural or functional connectome as a connectivity matrix allows researchers to apply network parameters derived from graph theory to analyze the brain's organizational principles. Each parameter offers a unique perspective on the network's organization and functioning.

Global network measures, such as global efficiency, characteristic path length, global assortativity, transitivity, and small-worldness, offer a comprehensive view of the overall network structure and efficiency. Global efficiency indicates the network's ability to efficiently transfer information across all nodes. It quantifies how effectively information can flow between different regions of the network. Another measure that assesses network communication efficiency is the characteristic path length which represents the average shortest path between all pairs of nodes in the network, offering insights into the network's overall communication efficiency. Meanwhile, global assortativity measures the tendency of nodes in the network to connect with other nodes that have a similar degree. It reflects the network's preference for forming connec-

tions between nodes with similar connectivity levels. Small-worldness characterizes the balance between network segregation and integration. Overall, these global network measures offer valuable insights into the organizational principles and functional dynamics of complex networks.

On the other hand, nodal network measures, including degree, strength, clustering coefficient, betweenness centrality, and local efficiency, focus on the characteristics of individual brain regions, explaining the importance of specific nodes in facilitating communication and shaping local network structures. The degree represents the number of connections a node has in the network, reflecting its capacity to communicate information and its level of connectivity. Strength quantifies the aggregate weight of a node's connections, taking into account the intensity and quantity of connections and indicating the node's overall influence within the network. The clustering coefficient measures the extent to which a node's neighbors are interconnected, indicating the presence of local clusters or communities around the node. Betweenness centrality captures the influence of a node over information flow between other nodes in the network, highlighting nodes that act as critical bridges or mediators in communication pathways. Local efficiency characterizes the efficiency of parallel information transfer within a node's local neighborhood, reflecting how effectively information is exchanged among immediate neighbors. These nodal network measures play a crucial role in understanding the contributions of individual nodes to network communication, highlighting nodes that play key roles in information processing and network dynamics. The combination of global and nodal measures enhances our understanding of brain connectivity, shedding light on the principles governing network organization and the specific roles played by individual regions in complex cognitive processes.

2.1. Brain Network as a Graph

A brain connectome can be modeled as a network for analysis using graph theory, as depicted in Figure 2.1. In mathematical terms, this network is represented by an $\mathbf{N} \times \mathbf{N}$ adjacency matrix, where $\mathbf{N}$ refers to the total number of nodes in the network,

with each node corresponding to a specific brain region. This matrix, denoted as $\mathbf{A} = w_{ij}$, is square and symmetric, with each element w_{ij} representing the weight of the connection between nodes i and j. These connections (edges), can be either weighted or unweighted. The weights reflect the strength or significance of the connections, providing a comprehensive depiction of the network's connectivity. In structural networks, the weight might reflect the size, density, or coherence of the anatomical tracts connecting two brain regions. In contrast, functional networks' weights represent the strength of correlation or causal interactions between brain regions. Weighted networks can be sparsified using various methods such as thresholding, proportional methods, or regularization techniques to avoid unwanted signals and reduce the complexity of the network. Thresholding involves setting a threshold value to remove weak connections that could be spurious and stem from noise in brain signals. Proportional methods involve adjusting the weights of connections by a specific proportion, thereby decreasing the density of the network. Regulation methods introduce constraints or penalties to encourage sparsity in the network, such as promoting zero values in the weights or enforcing specific patterns of connectivity. These sparsification methods help simplify and reduce the complexity of weighted networks while retaining essential information for analysis and interpretation.

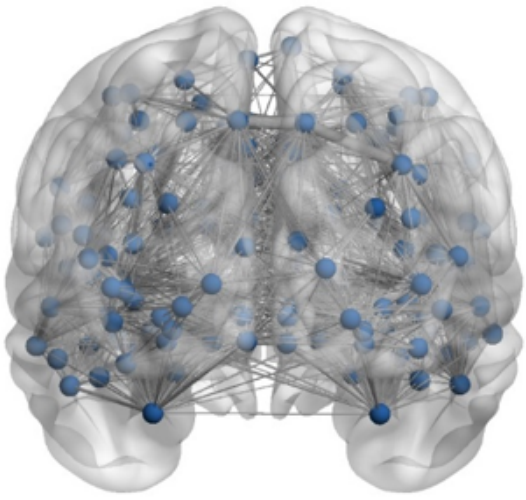

Figure 2.1. Brain network visualization using BrainNet-viewer tool [13].

2.2. Global and Nodal (Local) Network Measures

Global and nodal network measures are essential for understanding various aspects of brain network connectivity, integration, and resilience. These measures, each serving a distinct analytical role, provide insight into the brain's ability to process information efficiently both across the entire network and within localized regions.

Measures of integration, such as characteristic path length and global efficiency, offer insights into the efficiency of information transfer across the network. The characteristic path length represents the average shortest distance between all pairs of nodes in a network and is a fundamental measure of connectivity and efficiency. A shorter characteristic path length in a brain graph reflects improved communication efficiency among brain regions, whereas a longer path length suggests diminished information flow efficiency. Global efficiency, another measure of integration, is calculated as the average inverse of the shortest path length between all pairs of nodes. This metric evaluates the overall efficiency of information transfer within the network. High global efficiency in a brain graph indicates effective information flow across regions, supporting robust network function. Conversely, reduced global efficiency may signal impaired communication and integration within the network, often associated with disruptions in cognitive processing and connectivity.

Measures of segregation, such as the clustering coefficient and local efficiency, assess the brain's ability to form specialized local communities or modules. The clustering coefficient measures the degree to which nodes tend to cluster, indicating the presence of tightly interconnected groups. A higher clustering coefficient implies a strong degree of local specialization, highlighting the brain's ability to form cohesive circuits that support specialized functions. A lower clustering coefficient, on the other hand, may suggest weaker local connectivity, potentially impacting the brain's ability to support modular processing. Local efficiency assesses how well the immediate neighbors of a node communicate when that node is removed from the network. In brain graphs, this metric focuses on the efficiency of information processing within localized networks.

An increase in local efficiency indicates enhanced communication within local circuits, while a decrease may reflect reduced efficiency in processing information within specific brain regions.

Centrality measures, such as betweenness centrality, reveal the importance of specific nodes in maintaining effective communication across the network. Betweenness centrality measures the frequency with which a node lies on the shortest path between other nodes, positioning it as a critical connector within the network. Nodes with high betweenness centrality facilitate efficient communication across network regions, acting as bridges that maintain overall connectivity. Disruption of these central nodes can significantly impact the network's ability to maintain efficient information transfer, potentially leading to degraded network function.

Resilience measures, including the assortativity coefficient, provide insights into the network's robustness and adaptability. The assortativity coefficient measures the tendency of nodes to connect with other nodes that are similar in terms of degree or other attributes. A high assortativity coefficient suggests that nodes with similar characteristics preferentially connect with each other, enhancing the network's resilience to targeted disruptions by maintaining connectivity even if specific nodes are impacted. A low assortativity coefficient, in contrast, may indicate a more vulnerable network structure, where connections between dissimilar nodes could increase the risk of network fragmentation under stress.

Small-worldness is a property of networks characterized by high clustering and short path lengths. A high level of small-worldness in brain graphs reflects an optimal balance between local clustering and global connectivity, supporting effective information processing across the network. A decrease in small-worldness may indicate disruptions in this balance, potentially leading to reduced efficiency in both local and global information flow.

The systematic application of these network measures enables a comprehensive understanding of the brain's neural architecture and its role in supporting cognitive functions, providing valuable insights into how the brain achieves both local specialization and global integration.

2.3. Applications of Network Measures to Brain Connectomes in Alzheimer's Disease Dementia Research

Brain connectomes, representing the complex network of connections within the brain, are actively used to explore the brain's organization [14]. These connectomes are categorized into structural and functional networks, reflecting the structural connections among predetermined cortical regions and their corresponding functional associations. Graph theory has emerged as a prominent and established tool for analyzing networks, offering a strong framework to explore local and global measures. It helps capture different aspects of brain connectomes, contributing to a nuanced understanding of the brain's intricate architecture. These networks enhance our ability to dissect and interpret complex brain relationships, revealing insights into their structural and functional dynamics.

2.3.1. Structural Networks

sNETs are constructed using diffusion-weighted imaging (DWI) data and are primarily based on tractography. Tractography provides a coarse view of the architecture of white matter connections by exploiting constrained diffusion within myelinated axon fibers. sNETs represent structural connections between predefined brain (cortical) regions based on this coarse architectural model.

sNETs are much less studied and the associated literature is scarce. Compared with the HC group, decreased global sNET efficiency was observed in ADD [15, 16]. These studies used the Automated Anatomical Labeling (AAL) atlas [17]. These decreases signify disruptions in network efficiency and integration, reflecting the impact

of ADD on brain connectivity and information processing. Coninck et al. reported a higher average path length in sNETs for ADD cases compared to the HC group using AAL atlas [18]. Fischer et al. and Lo et al. revealed an unchanged clustering coefficient and a higher average path length in sNETs for ADD cases compared to the HC group using Harvard-0xford[1] and AAL atlas, respectively [15, 19]. Pereira et al. and Wang et al. reported a higher clustering coefficient and average path length in sNETs for ADD cases compared to the HC group using Desikan-Killiany Atlas and AAL atlas [20, 21]. The observed increase in average path length in these studies suggests that there may be increased distances or steps required for information to travel between different brain regions in individuals with ADD compared to Healthy Controls (HC). Additionally, the higher clustering coefficient seen in ADD cases compared to HCs may reflect network organization and efficiency disruptions, highlighting changes in local connectivity patterns within the brain's structural networks.

When examining the small-world topology, a combination of clustering coefficient and average path length, particularly in local connections, studies have shown that both ADD patients and HCs exhibit a small-world topology in sNETs [18, 21, 22]. While the overall small-world organization may be preserved, changes in the parameters that constitute it indicate that there are topological changes in the brain in ADD to maintain the small-world property. This demonstrates that alterations related to ADD, which cannot be detected when focusing on parameters at the global brain network level, become apparent when examined locally. Furthermore, this detailed investigation underscores the necessity of analyzing local parameters to understand that beneath unchanged global parameters lies a distinct topology.

2.3.2. Functional Networks

The majority of connectomics research on ADD focused on fNETs. fNETs represent functional associations between predefined brain (cortical) regions quantified as pairwise temporal correlations between regional BOLD signals.

[1] https://surfer.nmr.mgh.harvard.edu/

Primarily, statistical assessments of the clustering coefficient, path length, and small-worldness of fNETs between healthy and ADD cases were studied. Statistically significant changes in fNET small-worldness, indicating a disruption in efficiency in communication, have been reported repeatedly for ADDs compared to HCs [23–26]. Supekar et al. employed wavelet correlation to create correlation matrices from the regional fMRI time series data to assess functional connectivity [23]. They found a decrease in the global clustering coefficient in ADD, indicating a decrease in overall efficiency in communication between brain regions. However, the average path length remained unchanged, suggesting that the overall distance for information to travel was not affected. Sanz et al. used synchronization likelihood to create a functional connectivity matrix by quantifying the similarity in neural activity patterns between different brain regions [24]. They reported no significant change in the global clustering coefficient, but a decrease in average path length, indicating that the brain may adapt by shortening pathways between regions to ensure efficient communication.

Xiang et al. reported a decrease in the global clustering coefficient and an increase in path length using partial correlation, and Li et al. reported a decrease in the global clustering coefficient using Pearson correlation in ADDs compared to HC [27,28]. Xiang et al. and Li et al. report decreased clustering in ADD, supporting Supekar et al.'s findings of reduced interconnectedness. Additionally, Li et al. and Xiang et al. results decreased global fNET efficiency and increased clustering in ADD further highlighting the complex and potentially compensatory nature of fNET alterations in this condition.

Conversely, Zhao et al. and Liu et al. observed a higher global clustering coefficient and average path length for ADDs compared to HC using Pearson and partial correlation, respectively [24–26]. This suggests a potential compensatory mechanism where increased connectivity within specific regions and longer paths between them might attempt to maintain efficient information processing despite underlying neural deficits.

Luo et al. reported an increased global fNET assortativity coefficient for ADD, indicating a potential reorganization of functional brain networks in this population. [29]. They have also shown that local measures such as degree centrality, clustering coefficient, and local efficiency were significantly altered in ADD and Mild Cognitive Impairment (MCI) compared with healthy groups in the frontal gyrus and cerebellum regions indicating local changes. These specific regions are known to be associated with cognitive functions frequently impaired in ADD, making them strategically chosen areas. In a rare study of weighted fNETs, Filippi et al. showed decreasing nodal strength and local efficiency in ADD cases [30]. These studies used the AAL atlas.

These findings collectively suggest that there are alterations in functional connectivity patterns in individuals with ADD compared to HC. The variations in the results could be attributed to differences in the methodologies employed, such as the choice of correlation analysis (e.g., Wavelet, Pearson, and Partial correlation), which can influence the outcomes regarding global network measures. The inconsistencies in findings highlight the complexity of understanding functional connectivity changes in neurodegenerative disorders such as ADD and highlight the importance of considering various factors and examining localized when interpreting connectivity data.

2.4. Applications of Local Brain Connectome Measures in Alzheimer's Disease Dementia

A significant portion of the current literature on brain connectomes focuses on studying global changes in the brain connectomes through global network measures. While global measures have demonstrated high sensitivity in detecting neurodegenerative diseases, they may not fully capture the localized changes that could indicate different stages of ADD characterized by local neural degeneration and regeneration. These localized changes are likely to manifest across various topological scales. It has been observed that in some instances, individuals exhibit normal cognitive function despite the presence of amyloid plaque deposition – a key physiological indicator of ADD – suggesting the possibility of local resistance to the disease [31].

In the context of addressing these challenges, limited research in the literature has introduced diagnostic classifiers trained on specific local connectome features. However, these studies often grapple with the "curse of dimensionality," which arises from using high-dimensional feature spaces with small datasets, resulting in a sparse coverage of these high-dimensional feature spaces. Schouten et al. computed nodal strength, degree, clustering coefficient, and betweenness-centrality for all 110 nodes of the sNET they had built, to discriminate 77 ADDs and 173 controls [32]. Ebadi et al. employed 11 local sNET features computed for the 41 Brodmann areas to classify a cohort of 15 ADD, 15 MCI, and 15 HCs [33]. They reported optimal performance when 430 features were used for ADD-MCI and AD-HC classifications and 110 features for the MCI-HC classification. Khazaee et al. used global and local graph measures of fNETs, such as global/local efficiency and betweenness centrality from fNET, to discriminate 20 ADDs from 20 HCs [34]. They achieved the best performance diagnostic performance using a set of 21 local and global features.

These prior research results in the literature strongly suggest the existence of structural and functional organizational changes in the human brain across the spectrum of dementia, that are captured by fNETs and to a lesser degree by sNETs. However, a coherent and consistent picture of these alterations is challenging due to conflicting results.

2.5. Contribution of The Thesis

This thesis addresses a critical gap in understanding the complex mechanisms underlying cognitive decline in Alzheimer's Disease (AD). This research hypothesizes that clinical cognitive decline is not a monotonic process in the sense that the changes in the brain are not progressive and involve compensatory changes as well. To investigate this, the study focuses on analyzing sNETs and fNETs using nodal assortativity as a measure to capture how connections are reorganized across different areas of the brain and spectrum of clinical cognitive decline.

The findings provide evidence that structural and functional changes in the brain are highly localized and change in nature across the stages of cognitive decline. In the early stages (SCI to MCI), both sNET and fNET show a decrease in assortativity, reflecting a shift to more varied and flexible connections that may help the brain cope with early signs of damage. As the disease progresses from MCI to ADD, assortativity increases, indicating a move toward more uniform and rigid connectivity, particularly in structural networks. This shift likely marks a decline in the brain's ability to adapt as neurodegeneration advances. Functional changes are more noticeable in the early stages, while structural changes become prominent in later stages.

By revealing distinct patterns of structural and functional reorganization, this research offers alternative perspectives on brain resilience and vulnerability. This approach may help identify early signs of Alzheimer's, providing a foundation for further research on how the brain attempts to adapt while simultaneously losing resilience throughout disease progression.

3. METHODOLOGY

3.1. Brain Connectome Construction

The proposed methodology for investigating local brain connectome alterations across the cognitive decline spectrum involves a comprehensive pipeline, summarized in Figure 3.1.

The pipeline commences with neuroimaging data acquisition, including DWI, T1-weighted (T1w), T2-weighted (T2w), and resting-state functional magnetic resonance imaging (rs-fMRI). The T1w images are parcellated using the Schaefer atlas, which divides the brain into 400 cortical regions of interest (ROIs) [35]. sNETs are constructed using deterministic Principal Diffusion Direction (PDD) tractography with 4th order Runge-Kutta (RK4) regularization using DTI (Diffusion Tensor Imaging) derived from the acquired DWI data [36]. fNETs are constructed using regularized partial correlation coefficients using elastic net between parcel-wise summary BOLD signals. Details for both connectome construction are explained in the subsequent sections.

Both sNETs and fNETs are characterized using the graph theoretical nodal assortativity measure. Nodal assortativity quantifies the tendency of nodes with similar connectivity patterns to connect to each other. The nodal assortativity values for each region are used as features to represent the local connectivity patterns of the brain. To discriminate between groups (SCI (Subjective Cognitive Impariment) vs MCI and MCI vs ADD), feature selection identifies the most informative regions based on their assortativity values. By analyzing these values across 400 regions for each dementia stage, the study aims to pinpoint regions exhibiting localized changes in connectivity patterns over time. This approach is crucial for understanding disease progression by capturing spatial and temporal variations in discriminative features, surpassing traditional feature selection methods.

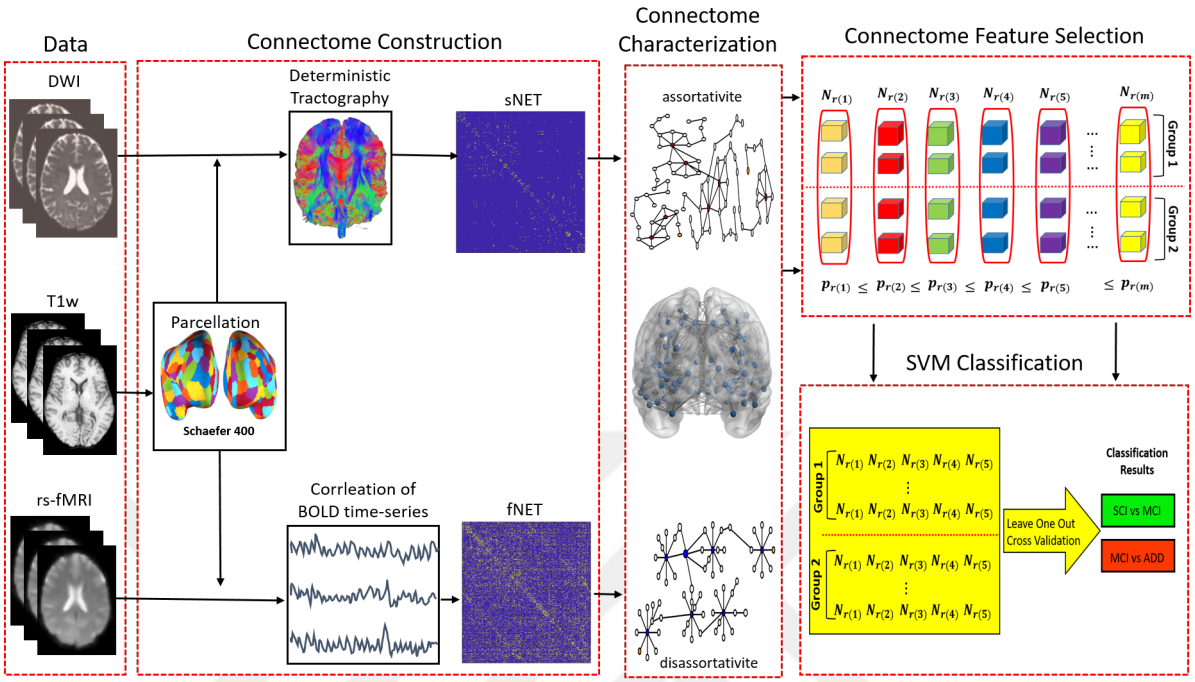

Figure 3.1. The analysis pipeline is composed of data collection, connectome construction, characterization, feature computation, feature selection, and classifier training/testing [37]. $r_{(i)}$ refers to the node ID with importance ranking i and $p_{r_{(i)}}$ is the corresponding p-value computed by t-test.

An SVM classifier is trained on the selected regions based on nodal assortativity values to classify individuals into different groups using their local connectome features. Due to the limited sample size, leave-one-out cross-validation (LOOCV) is utilized to rigorously evaluate the model's classification performance on new cases and prevent overfitting to the training data. This approach ensures the model's broader applicability and effectiveness across diverse scenarios.

This comprehensive methodology allows for a detailed investigation of local brain connectome alterations in clinical cognitive decline, providing insights into the complex relationship between structural and functional connectivity changes and their association with cognitive decline. Analyzing data focusing on local variations, combined

with temporal analysis and multi-modal data integration, provides a novel perspective on the underlying mechanisms of clinical cognitive decline and potential biomarkers for early disease progression detection and monitoring.

3.1.1. Data Preprocessing

Since structural and functional networks will be evaluated as one-to-one overlapping network structures, fMRI, dMRI (DWI - Diffusion Weighted Images, DTI - Diffusion Tensor Images), anatomical T1w, T2w, Parcellation, and Segmentation (Brain white/grey matter and cerebrospinal fluid (CSF) segmentation mask) data. They are all co-registered to the MNI152 space at 1mm isotropic resolution [38]. In addition to aligning the data across modalities to this standard, addressing noise and motion effects during data cleaning is imperative.

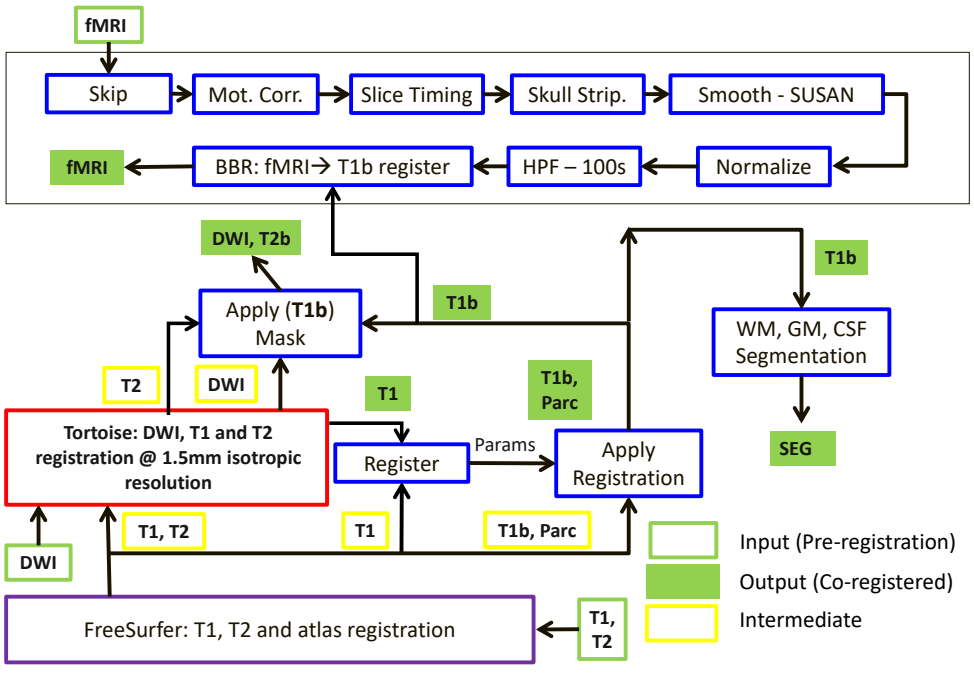

Figure 3.2. Preprocessing Pipeline [39]. The utilization of the Tortoise, FreeSurfer, and FSL programs is depicted by red, purple, and blue boxes, respectively. Parc refers to the Schaefer-400 Atlas parcellation.

The preprocessing pipeline utilizes the widely used FSL (FMRIB Software Library) [40], FreeSurfer [41], and Tortoise [42] applications for performing the processes as mentioned above. This fully automated pipeline, depicted in Figure 3.2, has been implemented on the CAPA dataset using an in-house preprocessing pipeline[2] . Within the FreeSurfer section of the pipeline, T1w and T2w data serve as inputs, yielding processed T1w and T2w images with or without the skull, in addition to the corresponding Schaefer Atlas parcellation. This segment encompasses two key procedures delineated by Glasser et al. as the pre-FreeSurfer (Figure 3.3) and FreeSurfer (Figure 3.4) pipelines [43]. The scripts are derived from the Human Connectome Project (HCP) pipeline [44].

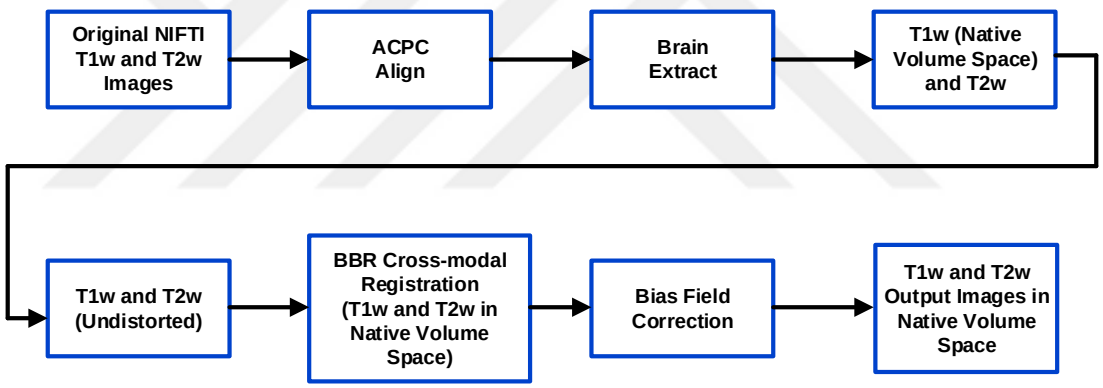

Figure 3.3. Pre-FreeSurfer Pipeline Block Diagram [43].

In the pre-FreeSurfer pipeline, the initial input comprises the original T1-weighted (T1w) and T2-weighted (T2w) images. These images undergo a series of preprocessing steps to prepare them for further analysis. First, AC-PC Alignment is performed to align the images based on the Anterior Commissure (AC) and the Posterior Commissure (PC), ensuring standardized orientation. Then, Brain Extraction is conducted to separate brain tissue from non-brain structures. The images are then transformed into

[2]The preprocessing and co-registration python script is available at https://vavlab.boun.edu.tr/brainet-structural-and-functional-brain-network-analysis

native volume space, providing the most accurate representation of the subject's brain size and shape. Subsequently, distortion correction is performed on the T1w and T2w images. A Boundary-Based Registration (BBR) Cross-modal Registration is applied to align the T1w and T2w images in native volume space [45]. Bias Field Correction is then carried out to address intensity variations caused by non-uniformities in the MRI scanner's magnetic field. Finally, the preprocessed T1w and T2w images are exported in their native volume space, maintaining their original orientation and dimensions as captured by the scanner. This ensures that the images are prepared for subsequent analysis without altering their spatial properties.

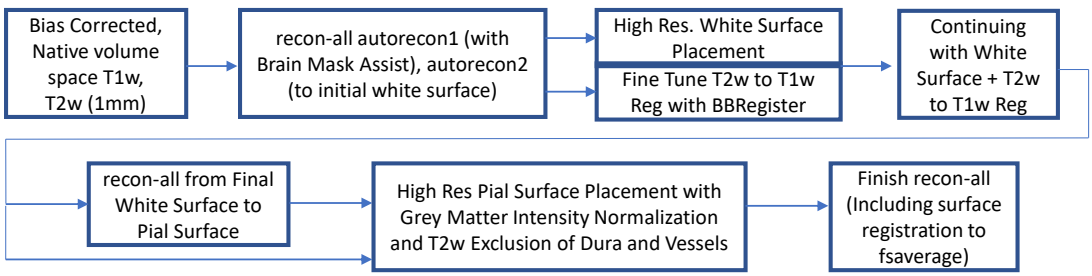

Figure 3.4. FreeSurfer pipeline block diagram [43].

The FreeSurfer pipeline focuses on a detailed analysis of brain structure, with a particular emphasis on cortical regions. The pipeline involves several critical steps to accurately reconstruct cortical surfaces and segment subcortical structures from structural MRI data. First, the Bias Corrected T1w and T2w images in native volume space are utilized as inputs. The FreeSurfer's *recon-all* process which is composed of *autorecon1* with Brain Mask Assist and *autorecon2*, is run on these images to initially reconstruct the white matter surface [46]. Subsequently, high-resolution white surface placement is conducted, followed by fine-tuning of the T2w image to the T1w image using BBR to improve alignment accuracy. Continuing with the white surface and

T2w to T1w registration, the *recon-all* process progresses from the final white surface to the pial surface. High-resolution pial surface placement is achieved with grey matter intensity normalization and exclusion of dura and vessels based on the T2w image. Ultimately, *recon-all* is finalized with surface registration to a standardized brain template. These meticulous steps ensure the precise generation of detailed cortical surface reconstructions and subcortical segmentations.

The Tortoise program employs two essential stages, DIFF PREP and DIFF CALC software, to process structural data. These steps encompass tasks such as image resampling, correction of motion distortion, re-orientation to a standardized space, and error analysis. Upon the conclusion of these processes, the resulting images have a resolution of 1.5 mm for DWI, T1w, and T2w data.

The registration parameters necessary for the preprocessing pipeline are obtained using the FSL program, leveraging both a 3D (Three Dimensional) T1w with 1 mm isotropic resolution from FreeSurfer and a T1w with 1.5 mm resolution from Tortoise. Registration with these parameters is applied to the T1-weighted image with the skull stripped (T1b) and the Schaefer atlas parcellation. The refined version of T1b is then utilized for the segmentation of white matter, gray matter, and CSF. Moreover, T1b serves as a crucial component for extracting the brain in T2-w images, yielding T2-weighted images with the skull stripped (T2b), and for processing DWI data outputted from Tortoise. Furthermore, T1b is essential for fMRI data registration, marking the last step in its comprehensive analysis.

The preprocessing of fMRI data was conducted utilizing the FSL program to ensure its optimization and standardization for subsequent analysis. Initially, a strategic exclusion of the first 5 volumes was implemented to stabilize the MRI scanner and allow participants to adapt. Subsequently, rigorous correction of motion artifacts and timing discrepancies was performed through Motion Correction and Slice Timing Correction procedures, respectively. Further refinement involved the meticulous elimination of non-brain tissues via Skull Stripping and the application of Spatial Smoothing

using the SUSAN algorithm to diminish noise [47]. The standardization of data across subjects was ensured through Data Normalization, while the removal of low-frequency noise was achieved using a Gaussian high-pass temporal filter with a cutoff frequency of 0.01 Hz. The culmination of the preprocessing pipeline involved the precise registration of fMRI data to the T1w volume using BBR, ensuring alignment accuracy.

3.1.2. Connectome Node Definition

A brain connectome node is an abstract representation of a distinct cortical region or parcel. These nodes form the foundation of brain network models, representing the fundamental units of the brain's interconnected structure.

The construction of a brain connectome begins with the parcellation of the cortex using a brain atlas. This process divides the brain into defined regions, each becoming a node in the connectome. The definition of nodes is identical for both sNETs and fNETs, ensuring a consistent comparison between physical and functional connections. The connections between these nodes, referred to as network edges, represent structural or functional relationships between brain regions.

One of the fundamental steps in constructing brain connectomes is the precise definition of nodes, which serve as the fundamental units representing distinct brain regions. The choice of atlas for node definition plays a pivotal role in shaping the subsequent analysis and interpretation of brain network data. Integration of the Schaefer atlas with Yeo's 7 subnetworks provides a robust framework to achieve this goal [48]. This combined approach facilitates a detailed segmentation of the brain into numerous regions, each preassigned to one of the seven large-scale network definitions in the Schaefer-Yeo atlas [35].

Furthermore, the flexibility of the Schaefer atlas in conjunction with Yeo's 7 subnetworks is underscored by its application across various studies to define connectome nodes at different spatial resolutions, ranging from 100 to 1000 nodes [49–52]. This

wide range of spatial resolutions of the Schaefer atlases allows researchers to tailor node definitions to the specific requirements of their investigations, ensuring alignment with the objectives of the study.

In summary, integrating the Schaefer atlas with Yeo's 7 subnetworks provides a comprehensive and adaptable framework for defining nodes in a connectome. Its ability to capture the complex functional organization of the brain, improve spatial resolution, and align with functional networks positions it as a valuable tool for investigating brain connectivity patterns and conducting diverse analyses. For a detailed list of the anatomical regions defined by the Schaefer atlas, along with their corresponding node IDs, abbreviations, and full node names which can be found on Github [53].

The node definition process forms the basis for constructing both sNETs and fNETs. Once the nodes are defined, undirected sNETs and fNETs are represented as $\mathcal{G}_m^{s/f} = \{N_m^{s/f}, L_m^{s/f}, \mathbf{A_{m \times m}}^{s/f}\}$. N and E are sets of nodes and links (edges), respectively, while $\mathbf{A}$ is a square and symmetric adjacency matrix that carries the weights of the edges. Nodes correspond to cortical regions defined by a given brain atlas that partitions the cortex into m non-overlapping volumes. The Schaefer atlases with 200, 400, and 800 nodes are used, each corresponding to a different spatial scale. These varying scales were applied to identify the most suitable resolution for conducting the analysis.

3.1.3. Structural Networks

sNETs are constructed using DWI data, primarily through tractography. DWI is an MRI technique that measures the anisotropic diffusion of water molecules within brain tissue, particularly along white matter fibers. This anisotropy arises from the structural constraints imposed by myelinated axons, which restrict water diffusion to specific directions.

DTI, a more advanced application of DWI, quantifies water diffusion using a mathematical construct called the diffusion tensor. Mathematically, the **D** is a $3x3$ symmetric positive-definite matrix, that captures how diffusion occurs across all possible directions at a given point. This tensor allows us to compute the principal axes of diffusion (eigenvectors) and the corresponding diffusivities (eigenvalues), which together describe the anisotropy and orientation of diffusion in tissues like white matter. The diffusion tensor can be expressed as:

$$\mathbf{D} = \begin{pmatrix} D_{xx} & D_{xy} & D_{xz} \\ D_{xy} & D_{yy} & D_{yz} \\ D_{xz} & D_{yz} & D_{zz} \end{pmatrix} \tag{3.1}$$

where, D_{xx}, D_{yy}, and D_{zz} represent the diffusivity along the x, y, and z axes, respectively. The off-diagonal elements D_{xy}, D_{xz}, and D_{yz} indicate the degree of correlation between diffusivities along different axes, capturing any anisotropic diffusion behavior. The eigenvalue decomposition of **D** is represented as:

$$\mathbf{D} = \mathbf{E} \cdot \Lambda \cdot \mathbf{E}^{-1} \tag{3.2}$$

where the eigenvector matrix **E** is :

$$\mathbf{E} = \begin{pmatrix} e_{1x} & e_{2y} & e_{3z} \\ e_{1y} & e_{2y} & e_{3z} \\ e_{1z} & e_{2z} & e_{3z} \end{pmatrix} \tag{3.3}$$

and the eigenvalues are organized into the diagonal matrix $\mathbf{\Lambda}$:

$$\mathbf{\Lambda} = \begin{pmatrix} \lambda_1 & 0 & 0 \\ 0 & \lambda_2 & 0 \\ 0 & 0 & \lambda_3 \end{pmatrix} \tag{3.4}$$

In this decomposition, $\mathbf{\Lambda}$ contains the eigenvalues, λ_1, λ_2 and λ_3, which correspond to the diffusivities along the principal directions defined by the eigenvectors in $\mathbf{E}$. The matrix $\mathbf{E}$ provides the orientation of these directions in 3D space, while the eigenvalues $\lambda_1 \geq \lambda_2 \geq \lambda_3$ indicate the magnitude of diffusion along each axis. The primary eigenvector, $\mathbf{e_1} = (e_{1x}, e_{2y}, e_{3z})$, represents the direction of the principal diffusion, indicating where the diffusion is strongest.

DTI is a second-order diffusion model that represents local diffusion structures using a 3D Gaussian distribution. The eigenvectors obtained from the eigenvalue decomposition of $\mathbf{D}$, which can be regarded as the covariance matrix of the Gaussian distribution, represent the principal diffusion directions along with the associated eigenvalues indicating the amount of diffusion along those directions.

Multiple DWI must be acquired across various gradient directions to estimate the diffusion tensor accurately. DTI protocols typically utilize around 30 to 120 gradient directions. Although estimating the tensor with as few as six gradient directions is mathematically feasible, using a higher number of directions improves the signal-to-noise ratio (SNR) and enhances the precision of the tensor estimation. Therefore, DTI was reconstructed [3] from multi-shell (b-values: $0 - 3000 s/mm^2$) DWI data using the dual tensor basis solution to the Stejskal-Tanner equations [54].

Through the analysis of the eigenvalues and eigenvectors of the DTI tensor, metrics such as fractional anisotropy (FA), mean diffusivity, axial diffusivity, and radial diffusivity can be derived. These metrics provide insights into tissue integrity, fiber orientation, and connectivity within the brain. The FA value serves as an indicator of whether a pathway traverses a voxel and is defined by the following formula:

$$FA = \sqrt{\frac{1}{2}} \frac{\sqrt{(\lambda_1 - \lambda_2)^2 + (\lambda_1 - \lambda_3)^2 + (\lambda_3 - \lambda_2)^2}}{\sqrt{\lambda_1^2 + \lambda_2^2 + \lambda_3^2}} \tag{3.5}$$

[3] The *DiffusionTensor3DReconstructionImageFilter* from ITK v6.0.0 is used.

where $\lambda_{1,2,3}$ represent the eigenvalues of diffusion tensor. FA is a key measure from DTI that quantifies the directionality of water diffusion in tissues, particularly white matter. FA values range from 0 (isotropic diffusion) to 1 (highly anisotropic diffusion). High FA values above 0.5 indicate highly directional water diffusion, typically seen in well-organized white matter tracts with myelinated axons. The principal diffusion direction aligns with the fibers, and the eigenvector corresponding to the largest eigenvalue represents this direction. Low FA values below 0.2 suggest more isotropic diffusion, often indicating disorganized or damaged white matter, such as in regions with crossing fibers or pathological conditions. This makes it harder to define clear fiber orientations. FA values are critical for accurate tractography. High FA regions allow for reliable reconstruction of white matter pathways, while low FA areas may lead to inaccuracies due to unclear fiber orientation or tissue complexity.

Deterministic tractography algorithms based on DTI create pathways by progressing along the PDD indicated by the eigenvector $\mathbf{e_1}$, which corresponds to the maximum eigenvalue λ_1 derived from $\mathbf{D}$. The tractography process starts from a specified seed point and continues until stopping conditions are met. Given the anatomical knowledge that pathways within the white matter interconnect gray matter regions, seed points are selected from within the white matter. For this purpose, gray matter, white matter, and CSF (Cerebrospinal Fluid) masks, generated using FSL during preprocessing, are used. Both gray matter and white matter areas are considered for seed selection to mitigate potential errors in seed selection due to segmentation inaccuracies in FSL. The FA value indicates whether a pathway traverses a given voxel. All white-matter voxels with $FA \geq 0.15$ were seeded 30 times, initiating bi-directional tractography. This threshold was selected because very low FA values may indicate the absence of fiber or the presence of multiple crossing fibers, making the diffusion tensor unable to reliably indicate a preferred direction. This limitation is inherent to deterministic DTI tractography, especially in regions with complex fiber configurations. Despite these challenges, DTI tractography remains a widely used method in neuroimaging research and is utilized in this thesis as well.

Among commonly used methods, the tractography algorithm employing the 4th order RK4 method is a popular choice for deterministic tractography with 0.15 minimum FA, $0.7mm$ stepsize, $20mm$ minimum fiber length and 35° maximum angle as a curvature threshold [36].

The ith parcel and the kth fiber association is represented by $\mathbf{W_{ik}}$ which is defined based on the probability of a diffusing particle originating from the endpoint of kth fiber (located at e_k) to end up at any point (x_j in P_i) in the ith parcel. The points x_j that are too far away from the kth fiber's endpoint ($|x_j - e_k| > 2\sigma$) are discarded. This process can be expressed as:

$$W_{ik} = \sum_{\substack{x_j \in P_i \\ |x_j - e_k| \leq 2\sigma}} \frac{1}{(2\pi)^{3/2}\sigma^3} \exp\left(\frac{-|x_j - e_k|^2}{2\sigma^2}\right) \tag{3.6}$$

where e_k denotes the endpoint of the kth fiber, and x_j represents the position of the jth voxel within the ith parcel P_i. The optimal value of σ has been determined as 0.155 for 30 seeds per voxel, using the kernel density estimation method outlined in [55].

sNETs were formed by computing connectivity values among network nodes identified from parcellation maps. The connectivity values, which are associated with fiber counts were utilized to define edge weights between parcels/nodes P_i and P_j are defined as follows:

$$e_{ij}^{n} = \frac{2}{V_i + V_j} \sum_{k} W_{ik} W_{jk} \tag{3.7}$$

where V_i and V_j represent volumes in mm^3, n represents normalized weighted (related to fiber counts).

3.1.4. Functional Networks

Understanding the complex functions of the brain relies heavily on analyzing how its different regions interact. In this study, we delve into the analysis of rs-fMRI data, where fluctuations in neural activity are reflected in BOLD signals. However, extracting meaningful insights from these inherently noisy signals requires the generation of region-specific summary signals. To address this challenge, three distinct methodologies are explored: averaging, Singular Value Decomposition (SVD), and SVD with Region Growing (SVD-RG).

The averaging method provides a simple yet effective way to compute the average BOLD signal across all voxels within a region. While straightforward, it may overlook spatial variations within the region. On the other hand, SVD takes a more sophisticated approach by constructing a matrix with voxels as columns and time points as rows [56]. By applying SVD, we uncover dominant temporal activity patterns across the region, with the first left singular vector serving as the summary signal, capturing essential temporal dynamics. SVD-RG integrates SVD with the concept of "region growing," starting with the analysis of the frequency content of BOLD signals using SVD. The dominant frequency pattern revealed by the leading left singular vector unveils the region's primary oscillatory rhythm. A single voxel exhibiting this rhythm acts as the seed for a growing region, gradually incorporating neighboring voxels with similar frequency signatures. Finally, SVD is applied to the BOLD signals within this refined region, yielding a summary signal encompassing both temporal and spatial aspects of activity.

The next crucial element in constructing a graph is defining edges connecting nodes. In functional networks, these connections represent statistical associations like correlation, coherence, or mutual information between pairs of ROIs' (regions of interest) time-series regional signals. The network's adjacency matrix comprises these links, with the method applied to signals determining the network type, such as weighted (e.g., cross-correlation in the range of $[0, 1]$, partial correlation in the range of $[-1, 1]$),

binary (after thresholding), directed (e.g., Granger causality, lags), or undirected networks.

A variety of metrics have been employed to estimate or construct functional brain networks. Among these, Pearson's correlation coefficient is the most widely utilized method due to its simplicity and effectiveness in providing insights into the intrinsic functional organization of the brain. Partial correlation coefficients measure the direct relationships between pairs of brain regions while controlling for the influence of other regions, allowing for a clearer understanding of connectivity. While partial correlation offers the advantage of filtering out indirect effects caused by linear influences from distant brain regions, it also has some limitations. These limitations include requiring more observations than ROIs, the risk of overfitting, and potentially producing less stable estimates.

Regularized partial correlation coefficients using elastic net for constructing functional networks based on resting-state fMRI to overcome the limitation of the partial correlation coefficient [57]. The elastic net regularization which uses penalization of both a linear combination of L1 norm (Lasso) and L2 norm (Ridge) regularization can be formulated as an optimization problem:

$$min_{\beta_0,\beta} \frac{1}{N} \sum_{i=1}^{N} \theta_i l\left(y_i, \beta_0 + \beta^T x_i\right) + \lambda \left[\frac{1}{2}\left(1 - \alpha \left\|\beta\right\|_2^2\right) + \alpha \left\|\beta\right\|_1\right] \tag{3.8}$$

Additionally, the optimization of the coefficients can be expressed as:

$$\hat{\beta} = argmin_{\beta} \left\|\mathbf{y} - \mathbf{X}\beta\right\|^2 + \gamma \left[(1-\alpha)\left\|\beta\right\|^2 + \alpha \left\|\beta\right\|_1\right] \tag{3.9}$$

where $\mathbf{y}$ is the response variable (the summary signal of a brain region), $\mathbf{X}$ is the design matrix containing the predictors (summary signals of other parcels), β is the vector of coefficients to be estimated, l is the negative log-likelihood function, θ_i is the weight associated with the observation x_i, N is the total number of observations, γ controls the overall penalization of the model, α determines the relative weight placed on L1

regularization compared to L2 regularization. When minimizing the objective function (Equation 3.8), it is essential to optimize the parameters γ and α. For instance, If $\alpha = 1$, the model reduces to LASSO regression, which emphasizes sparsity in the coefficient estimates [58]. Conversely, if $\alpha = 0$, the model corresponds to ridge regression, focusing solely on L2 regularization [59]. To identify optimal parameter values, various methods can be employed, including grid search techniques, which systematically evaluate combinations of γ and α to determine the best-performing model.

After calculating regularized β coefficients with the optimized regularization parameters, partial correlation coefficients ($\hat{\rho_{ij}}$) are computed from these β values. The estimation and optimization processes are performed separately for each network. The partial correlation coefficients are computed as follows:

$$\hat{\rho_{ij}} = \begin{cases} \text{sign}\left(\hat{\beta}_j^{(i)}\right) \min\left\{1, \sqrt{\hat{\beta}_j^{(i)} \hat{\beta}_i^{(j)}}\right\} & \text{if sign}\left(\hat{\beta}_j^{(i)}\right) = \text{sign}\left(\hat{\beta}_i^{(j)}\right) \\ 0 & \text{otherwise.} \end{cases} \tag{3.10}$$

3.2. Brain Connectome Measures

Following the establishment of multiscale sNETs and fNETs, the subsequent phase involves extracting valuable insights from these network structures, serving both scientific and clinical objectives. The adoption of "complex network theory," which originated from statistical physics research and has seen widespread applications across various fields over the past decade or so [60, 61], is particularly prevalent in brain research [62]. This theory enables researchers to quantitatively compare brain networks across different individuals and even within the same individual over time, offering a valuable tool for understanding the dynamic nature of brain connectivity.

This thesis utilized the Brain Connectivity Toolbox (BCT) (`https://sites.google.com/site/bctnet/`) to compute the aforementioned network measures described in Rubinov and Sporns [63]. The BCT offers a comprehensive range of graph-

theoretical measures designed to quantify different aspects of brain networks.

Among the many available measures, a specific subset was selected for this thesis based on their relevance and frequent use in brain connectivity studies. Section 2 introduces a variety of network measures, with a particular focus on those commonly used in the literature, especially in studies related to ADD. These metrics are recognized for their ability to capture key aspects of network topology, such as integration, segregation, centrality, and resilience. Nodal assortativity, which was the primary focus of this thesis, was used to localize significant topological changes throughout the progression of clinical cognitive decline. However, additional metrics were also included for comparison in the classification analysis to evaluate their effectiveness. The comparison provides valuable insights into the most effective metrics for identifying disruptions in brain connectivity, shedding light on their potential application in future research on neurological disorders.

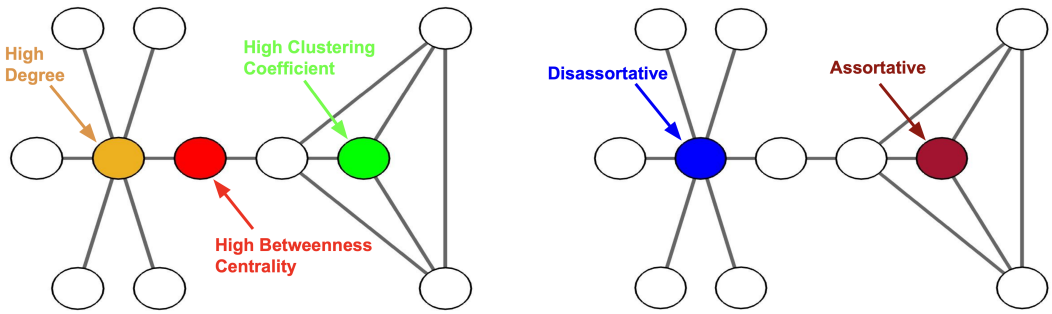

Figure 3.5. Graph measures. The yellow node indicates a high degree (a hub for local communication), the red node indicates high betweenness centrality (a bridge for information flow), and the green node indicates a high clustering coefficient (local cluster formation). (b) The blue node represents disassortative connections, while the maroon node represents assortative connections.

3.2.1. Basic Measures

Degree is the number of connections that a node has with other nodes in the network. In the context of brain networks, a node's degree reflects how interconnected a particular brain region is with other regions. This metric is particularly useful for understanding the role and influence of individual brain regions in the overall network structure. A high degree suggests a brain region plays a significant role in communication and information flow, while a lower degree might indicate a more specialized or isolated function. Node degree is formulated as:

$$d_i = \sum_{j=1}^{N} a_{ij} \tag{3.11}$$

where d_i represents the degree of node i, N is the total number of nodes in the network, and a_{ij} is the binarized from of w_{ij}, indicating the connection status between nodes i and j: $a_{ij} = 1$ when the link (i, j) exists; $a_{ij} = 0$ otherwise ($a_{ij} = 0$ for all $i = j$).

Strength is the total weight of connections linked to a specific node. It is a fundamental measure in network analysis, providing insights into the connectivity and centrality of individual nodes within the network. Measuring connection strength between brain regions helps understand information flow pathways and their efficiency in transmitting information. Additionally, altered connection strengths might be linked to the development or progression of neurological disorders. Node strength is calculated as:

$$s_i = \sum_{j=1}^{N} w_{ij} \tag{3.12}$$

where w_{ij} denotes the weight of the connection between nodes i and j and N is the total number of nodes in the network.

3.2.2. Measures of Segregation

Clustering coefficient quantifies the degree of interconnectedness or clustering among the immediate neighbors of a node within a network. It measures the likelihood that the neighbors of a particular node are also connected. A higher clustering coefficient indicates a greater amount of localized communication and information processing within specific brain regions, while a lower clustering coefficient suggests a more distributed or less specialized organization of brain regions in their interactions and communication. The clustering coefficient is expressed by Watts and Strogatz [61] through the following formula:

$$C_i = \frac{2T_i}{d_i(d_i - 1)} \tag{3.13}$$

where C_i is the clustering coefficient of node i and d_i is the degree of node i and T_i is the number of triangles associated a node i. T_i is calculated as :

$$T_i = \sum_{j \neq k} a_{ij} a_{jk} a_{ki} \tag{3.14}$$

where a_{ij} indicates whether there is a connection (1) or no connection (0) between node i and node j. a_{jk} indicates whether there is a connection (1) or no connection (0) between node j and node k. a_{ki} indicates whether there is a connection (1) or no connection (0) between node k and node i.

3.2.3. Measures of Centrality

Betweenness centrality quantifies the extent to which a node serves as a bridge along the shortest paths between other nodes in the network. This metric is crucial for identifying key nodes that connect or mediate within the network. An increase in betweenness centrality indicates that a node is becoming a critical connection point in the brain network, facilitating communication between various brain regions as information flows through it more frequently. Conversely, a decrease in betweenness centrality

suggests a decline in the node's role as a communication hub, potentially leading to a diminishing significance as a bridge for information exchange within the brain graph. Betweenness centrality is defined by the following formula [64]:

$$B_i = \sum_{s \neq i \neq t} \frac{\sigma_{st}(i)}{\sigma_{st}} \tag{3.15}$$

where B_i is the betweenness centrality of node i, σ_{st} represents the total number of shortest paths from node s to node t, and $\sigma_{st}(i)$ denotes the number of shortest paths from node s to node t that pass through node i. σ_{st} is calculated as:

$$\sigma_{st} = \min_{\Gamma_{st}} \sum_{(u,v) \in \Gamma_{st}} w_{uv} \tag{3.16}$$

where σ_{st} is the shortest path length between nodes s and t, $\mathbf{\Gamma_{st}}$ represents the set of all possible paths between nodes s and t, and w_{uv} is the weight of the connection between nodes u and v.

3.2.4. Measures of Resilience

Global Assortativity measures the tendency of nodes in a network to connect with other nodes that have a similar degree. An increase in global assortativity indicates a stronger preference for nodes with shared attributes to connect, potentially indicating a greater level of specialization or segregation in brain functioning. Conversely, a decrease in global assortativity suggests a more diverse or less structured connectivity pattern, potentially indicative of a more integrated brain functioning. Global assortativity is formally defined as [65],

$$r = \frac{\sum_{ij}(d_i d_j/N) - (\sum_{ij}(d_i + d_j/2N))^2}{\sum_{ij}(d_i^2 + d_j^2)/2N - (\sum_{ij}(d_i + d_j/2N))^2} \tag{3.17}$$

where double sums are over pairs of connected nodes, N is the total number of nodes in the network and d_i is the degree of ith node which is essentially the number of neighbors

in a binary network.

Local assortativity is a measure of the tendency of nodes in a network to form connections with nodes that have similar local characteristics. Unlike global assortativity, which considers the entire network, local assortativity focuses on the neighborhoods of individual nodes. Local assortativity in brain graphs plays a critical role in determining the resilience, efficiency, and organization of neural networks.Local assortativity of node i, $r_i \in [-1, 1]$, is defined as [66],

$$\delta_i = \frac{1}{d_i} \sum_{j \in \mathbf{N}_i} |d_j - d_i| \tag{3.18}$$

$$\bar{\delta}_i = \frac{\delta_i}{\sum_{j=1}^{N} \delta_j} \tag{3.19}$$

$$r_i = \frac{r+1}{N} - \bar{\delta}_i \tag{3.20}$$

where δ_i is the mean difference between the degree of a node and those of its neighbors, N is the number of nodes in the network.

3.3. Statistical Anaylsis

In order to pinpoint significant topological changes in brain networks, reflected by nodal assortativity, across the clinical cognitive decline spectrum, two key discrimination tasks were designed that focus on different stages of this spectrum: SCI-vs-MCI and MCI-vs-ADD. These tasks address specific points in the clinical cognitive decline continuum. SCI is considered a preclinical phase and is characterized by the subjective experience of cognitive decline without measurable clinical impairment. MCI represents a more advanced phase, marked by measurable cognitive deficits that surpass typical age-related decline but do not meet the criteria for dementia. Finally, ADD represents the fully developed clinical presentation of Alzheimer's disease, associated with severe cognitive impairment that impacts daily life. Focusing on these specific stages allows for the investigation of how brain network organization evolves with cognitive deterioration, thus offering a window into spatially localized reorganiza-

tion across brain regions as well as potential temporal progression in network changes. To systematically identify and verify the local brain regions that undergo significant structural and/or functional reorganization across different stages of cognitive decline, a two-stage approach was implemented.

3.3.1. Hypothesis Testing and Feature Selection

The first stage of the analysis involves feature selection and statistical testing to identify specific brain regions (nodes) that demonstrate significant changes in nodal assortativity across the stages of cognitive decline. For each node in the brain network, nodal assortativity was calculated. This metric reflects how a node connects to other nodes with similar degrees, providing insights into local network organization. To determine whether the changes in nodal assortativity between groups (SCI-vs-MCI and MCI-vs-ADD) were statistically significant, Welch's t-test was applied independently to each node. Welch's t-test was chosen due to its robustness in handling unequal variances and its suitability for unequal sample sizes, which are common in clinical datasets. The null hypothesis assumes that nodal assortativity values between the two groups (e.g., SCI and MCI) come from normal distributions with equal means. Nodes with a p-value ≤ 0.05 were considered statistically significant, indicating that observed differences in nodal assortativity are unlikely to have occurred by chance.

Limiting the feature set to only the most statistically significant nodes ensures that the analysis remains focused on the most relevant regions, thereby enhancing both the robustness and interpretability of the findings. To evaluate the influence of feature dimensionality, feature sets of increasing size, from 1D to N-D, were used, where N represents the number of nodes with p-value ≤ 0.05, ranked by their p-values for each discrimination task. This approach resulted in classifiers trained with incremental feature sets, starting from the top-ranked individual feature and extending up to the top N features.

3.3.2. Classification, Validation, and Robustness Assessment

From the prioritized list of nodes ranked by statistical significance, the top 5 nodes were selected for further analysis. This spatial localization of brain regions focuses on identifying key nodes that play a role in cognitive decline as it progresses from SCI to MCI and then to ADD. The dimension was fixed at 5 based on an experimental determination that it offers a good balance between capturing important changes in network structure and avoiding overfitting or the *curse-of-dimensionality*, which can arise when too many features are used in relation to the number of samples available for training a classifier.

In the second stage, the temporal relevance of these identified nodes was verified by training and testing a support vector machine (SVM) classifier using the Leave-One-Out Cross-Validation (LOOCV) method. LOOCV was chosen because it allows each sample to be tested individually, providing a robust estimate of classifier performance, especially in small datasets. This not only confirmed the spatial significance of the identified nodes but also validated their role in the temporal progression of the disease. By measuring classifier performance, specifically in terms of accuracy, empirical support is obtained for the hypothesis that these regions undergo meaningful organizational changes as cognitive decline advances.

To further confirm the robustness of the results, a random label shuffling experiment was conducted. Specifically, the class labels (SCI, MCI, and ADD) of all subjects were randomly shuffled, breaking the real underlying group structure and thus disrupting any temporal patterns in disease progression. The shuffling process was repeated 1000 times to ensure reliability. The Welch's t-tests were again conducted for each node, ranking the nodes and selecting the top 5 based on the shuffled labels, similar to the earlier analysis. These top 5 nodes were subsequently used to train and test SVM classifiers with LOOCV. The classification accuracy results were averaged across the 1000 shuffles to provide a mean accuracy score. If the classifier performance with true labels significantly exceeds this shuffled baseline, it provides strong evidence

that the selected nodes are genuinely associated with disease-related network changes, rather than being the result of random variation. This method acts as a null model to rule out overfitting and spurious associations, thereby providing strong support for the identified brain regions as critical components in the network changes associated with cognitive decline.

4. EXPERIMENTS

4.1. Data

4.1.1. Cohort and Clinical Assessment

The study cohort is composed of 88 participants signed up following a written consent in accordance with the ethical committee approval[4] . The participants were clinically assessed following the NIA-AA criteria and grouped into early-stage ADD (n = 16), mild cognitive impairment of the amnestic type (MCI) (n = 46), and SCI (n = 24) [67].

Table 4.1. Summary of the cohort of participants.

	SCI (n=24)	**MCI (n=46)**	**AD (n=18)**
Age	56.95 ± 7.54	62.04 ± 9.78	69.83 ± 8.52
Gender (F/M)	12/12	23/23	8/10
FCRST-CI	0.88 ± 0.10	0.68 ± 0.15	0.36 ± 0.21
FCRST-TFR	33.45 ± 3.85	20.63 ± 5.46	6.33 ± 7.23

Additionally, individuals with no recorded NIA-AA diagnostic criteria for AD, MCI, or SCI are also considered. Furthermore, individuals without memory impairment who are relatives of those meeting the NIA-AA criteria are included. Similarly, individuals without a family history of AD, MCI, or SCI, and who do not exhibit memory impairment themselves, are eligible. Lastly, volunteers must have been consistently taking neurological medications at the same dosage for the past three months. Table 4.1 provides a summary of the study cohort. In accordance with the NIA-AA criteria, the clinical diagnosis of amnestic type MCI is based on identifying an objective

[4]Istanbul University, Istanbul Faculty of Medicine, Ethics Committee Approval: 877/30.05.2014; Boğazici University, Ethics Committee Approval: 2014-1/17.02.2014

deficit in episodic memory with a total free recall score (TFR) of 27 or lower and a Cue Index (CI) of 0.67 or lower on the Free and Cued Selective Reminding Test (FCSRT) [68]. Participants scoring above 27 in TFR-FCSRT or above 0.67 in CI-FCSRT were classified as SCI. The chosen TFR cutoff of 27 was more liberal than 24, a highly sensitive predictor of future dementia in dementia-free individuals [69]. ADD participants met NIA-AA criteria for probable AD with an amnestic presentation [70]. SCI subjects were project volunteers responding to advertisements, scoring at least 1 on either Cognitive Functions Instrument – Subject form (CFI-S) or CFI – Study Partner form (CFI-SP) [71]. Comprehensive neurological and neuropsychological examinations, along with cranial magnetic resonance imaging (MRI), confirmed SCI, MCI, and ADD diagnoses by a panel of behavioral neurologists. The panel ensured that ADD participants had a Clinical Dementia Rating (CDR) score of 0.5 or 1, indicating very mild or mild dementia; MCI patients had a CDR score of 0.5 and CDR-Sum of Boxes (CDR-SOB) score of 0.5 or 1; and SCI subjects had a CDR score of 0. As such, SCI group serves as the control group within the scope of this study. Exclusion criteria encompassed a history of neurological or psychiatric disorders affecting cognition, alcohol or substance abuse, major head trauma with loss of consciousness, and white matter hyperintensities on MRI with a Fazekas score of 2 and 3. Participants with contraindications for MRI scanning were also excluded from the study.

4.1.2. Data Acquisition

T1 weighted MRI data was acquired using a 3D FFE (Fast Field Echo) pulse sequence with multi-shot TFE (Turbo Field Echo) imaging mode using the Philips Achieva 3T MRI system (Netherlands) with a 32-channel head coil at Istanbul University, Istanbul Faculty of Medicine, Neuroimaging Unit of Hulusi Behçet Life Sciences Research Laboratory. The acquisition parameters were $TE/TR = 3.8\,ms/8.3\,ms$, $flip\,angle = 8°, FOV = 220 \times 240\,mm^2$, $1.0\,mm^3$ isotropic voxels and 180 slices. Diffusion-weighted imaging (DWI) data was acquired with 120 gradient directions with a maximum gradient strength of $40\,mT/m$ and a high slew rate of $200\,mT/m/ms$, at 6 shells in q-space. FOV was $220 \times 236\,mm^2$ with imaging matrix 112×112 and 71 slices

with slice thickness of $2.27\,mm$. rs-fMRI data is acquired using the Fast Field Echo (FFE) technique in a multi-slice mode with a single-shot EPI sequence. The acquisition parameter were $TE/TR = 30\,ms/3000\,ms, flip\,angle = 80°, FOV = 212 \times 199\,mm^2$. 200 EPI volumes and 48 axial slices were acquired with eyes-closed.

4.2. Multi-scale Analysis

A large part of the current literature on brain connectomes is based on studies of global changes in the brain connectomes measured by global network parameters. Despite the high sensitivity reported in neurodegenerative diseases, the global parameters cannot capture local changes that may manifest ADD at different stages through local neural degeneration and regeneration [62]. Such changes are likely to be captured at different topological scales. Local changes in brain networks may occur due to neural degeneration and regeneration in specific regions, which might not significantly affect the overall network but could still play a crucial role in the cognitive decline associated with ADD. These localized changes are crucial for understanding how different brain areas may exhibit resilience or vulnerability to degeneration. For example, researchers indicate that the pathological process of $A\beta$ accumulation is indeed a gradual phenomenon that can precede clinical manifestations of dementia by decades of amyloid plaque deposition [72, 73]. However, the brain's compensatory mechanisms may postpone the appearance of clinical symptoms during the early stages of the disease, even in the presence of amyloid accumulation. This observation highlights the importance of studying brain network organization across different spatial and topological scales to capture both global and local changes.

The spatial scale of analysis is largely dictated by the resolution of the brain atlas used to construct the connectome. Brain atlases divide the brain into distinct regions (parcels or nodes), and the connectivity between these regions is modeled based on structural or functional data. The spatial resolution of an atlas can significantly impact the interpretability and reliability of the results. Atlases with low spatial resolution divide the brain into fewer regions, which may lead to poor spatial localization

of network changes. While low-resolution atlases might be useful for global assessments, they may miss localized changes critical for understanding disease progression in specific brain regions. On the other hand, atlases with high spatial resolution divide the brain into many smaller regions, allowing for finer spatial localization of network changes. However, this increased granularity can lead to lower SNR, which may result in unreliable connectome models. The trade-off between spatial localization and SNR becomes critical when selecting the optimal resolution for studying brain networks at different stages of ADD.

Given the trade-off between spatial resolution and reliability, it is important to assess how selected connectome parameters behave at different spatial scales. The optimal spatial scale may vary depending on the specific network parameters being studied, as well as the type of connectome (structural or functional). For example, some parameters may reveal more informative patterns at a coarse scale, while others might require a finer scale for detecting subtle changes. Thus, a multi-scale approach, where the connectome analysis is repeated across different spatial resolutions, is crucial to comprehensively capture the network changes associated with cognitive decline.

To explore the spatial scale dependency of the connectome parameters, a detailed analysis will be conducted using multiple brain atlases with varying resolutions. Specifically, the Schaefer atlas was used at three different resolutions: 200, 400, and 800 nodes. These resolutions represent progressively finer divisions of the brain, allowing for the study of network parameters at multiple spatial scales. The analysis will be conducted at three topological levels: global, mesoscale (subnetwork), and nodal (local).

Figure 3.1 depicts the complete pipeline from connectome construction to SVM training and testing. The complete pipeline was repeated for both sNETs and fNETs, at 3 different spatial scales, namely for $m = \{200, 400, 800\}$.

4.2.1. Global (Complete Network) Scale

At the global level, assortativity was calculated across all connectome nodes. This will provide insights into how overall network organization changes across the disease spectrum (SCI, MCI, ADD) as a function of spatial resolution. Global assortativity coefficients (r) of individual sNETs and fNETs, as reported in the literature, were calculated to serve as a baseline, for SCI, MCI, and ADD stages of clinical cognitive decline for 200, 400 and 800 spatial scales. These coefficients were benchmarked against the literature.

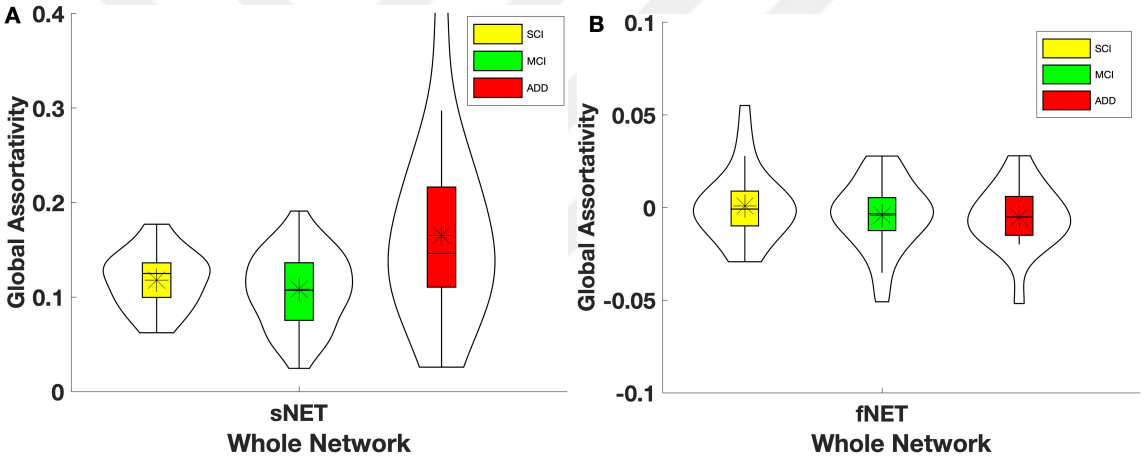

Figure 4.1. Distributions of global assortativity coefficients (r) of (A) sNETs, and (B) fNETs in each group for Schaefer 200. sNETs show assortative structure, while fNETs are primarily disassortative. sNETs did not differ significantly between SCI and MCI ($p > 0.248$), but differed significantly between MCI and ADD ($p = 0.021$). For fNETs, no significant differences are observed across stages ($p > 0.83$).

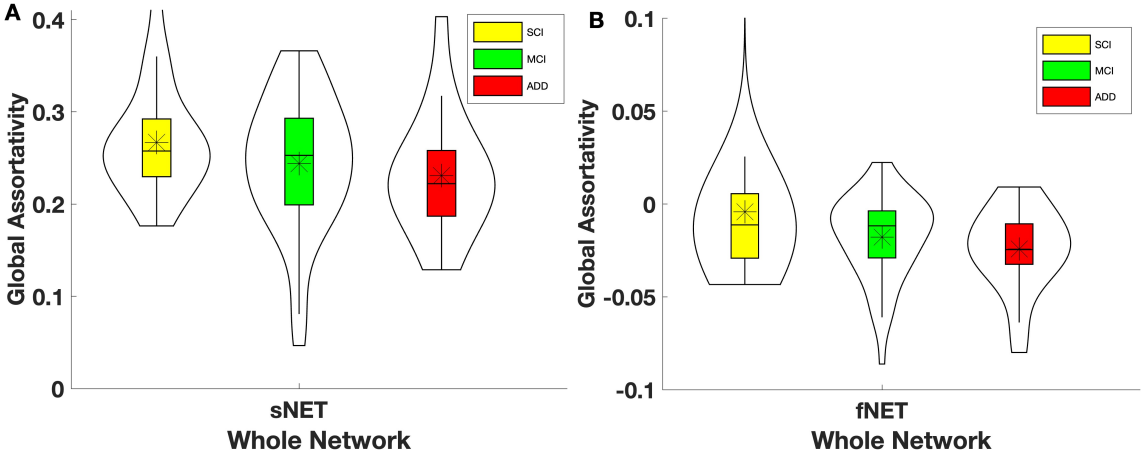

Figure 4.2. Distributions of global assortativity coefficients (r) of (A) sNETs, and (B) fNETs in the ADD, MCI and SCI groups for Schaefer 400. sNETs show assortative structure, while fNETs are primarily disassortative. There is no statistically significant difference between different stages of clinical cognitive decline ($p > 0.291$).

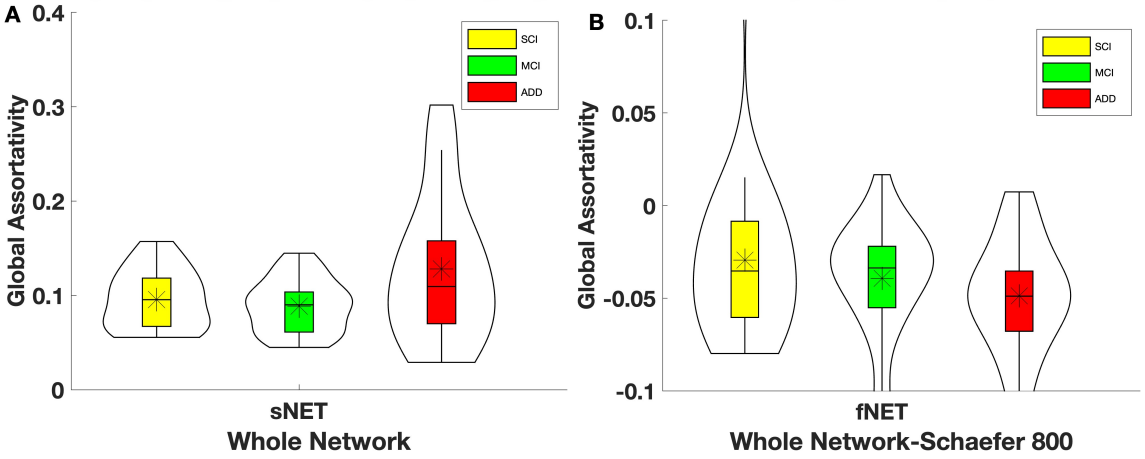

Figure 4.3. Distributions of global assortativity coefficients (r) of (A) sNETs, and (B) fNETs in the ADD, MCI and SCI groups for Schaefer 800. sNETs show assortative structure, while fNETs are primarily disassortative, with no significant differences across cognitive decline stages ($p > 0.054$).

Figures 4.1, 4.2 and 4.3 depict the global assortativity distributions for each group. In agreement with the literature, sNETs are assortative ($r > 0$), while fNETs' global assortativity coefficient is close to 0 and primarily shows disassortativity ($r < 0$) across the disease stages for any spatial scale. The consistent findings across different spatial scales suggest that the global assortativity properties are relatively robust to changes in parcellation resolution. This distinction between sNETs and fNETs aligns with findings from prior studies [57]. Despite this consistent difference between the global assortativity coefficients of sNETs and fNETs, neither one shows significant variability between the stages of clinical cognitive decline, except sNETs in the Schaefer 200 parcellation, where a significant difference is observed between MCI and ADD. The simple threshold classifier yields an AUC of 0.69.

4.2.2. Mesoscale (Subnetwork) Scale

Subnetwork assortativity refers to assortativity within a specific subset of an entire network. sNETs and fNETs were created for seven subnetworks according to the Schaefer atlas scale. Each region of Schaefer parcellation is associated with one of the subnetworks [48]. The dimensions of each subnetwork varied based on the Schaefer atlas scale:

- Schaefer 200: Visual (29x29), Somatomotor (35x35), Dorsal Attention (26x26), Salience/Ventral Attention (22x22), Limbic (12x12), Control (30x30), Default (46x46)
- Schaefer 400: Visual (61x61), Somatomotor (77x77), Dorsal Attention (46x46), Salience/Ventral Attention (47x47), Limbic (26x26), Control (52x52), Default (91x91)
- Schaefer 800: Visual (134x134), Somatomotor (151x151), Dorsal Attention (99x99), Salience/Ventral Attention (87x87), Limbic (54x54), Control (105x105), Default (170x170)

Table 4.2. P-values and AUCs for assortativity of Yeo's 7 subnetworks sNETs and fNETs across the cognitive decline spectrum at 200, 400, and 800 scales.

		Task		Visual	Somatomotor	Dorsal Attention	Salience/Ventral Attention	Limbic	Control	Default
Schaefer 200	**sNET**	**SCI-MCI**	**p**	0.382	0.193	0.675	0.756	**0.038** (↓)	0.912	0.520
			AUC	0.432	0.597	0.456	0.523	**0.630**	0.498	0.506
		MCI-ADD	**p**	0.664	0.147	0.505	**0.047** (↑)	0.131	0.820	0.145
			AUC	0.460	0.372	0.542	**0.623**	0.351	0.519	0.385
	fNET	**SCI-MCI**	**p**	0.515	0.522	0.254	0.918	0.916	0.878	0.569
			AUC	0.548	0.571	0.563	0.486	0.511	0.477	0.517
		MCI-ADD	**p**	0.870	**0.014** (↑)	0.802	0.590	0.757	0.606	0.984
			AUC	0.511	**0.707**	0.508	0.473	0.517	0.492	0.478
Schaefer 400	**sNET**	**SCI-MCI**	**p**	0.828	0.116	**0.042** (↓)	0.775	0.566	0.740	**0.022** (↓)
			AUC	0.444	0.630	**0.661**	0.493	0.549	0.484	**0.644**
		MCI-ADD	**p**	0.111	0.554	0.337	0.191	0.838	0.759	**0.049** (↓)
			AUC	0.615	0.393	0.411	0.356	0.508	0.517	**0.664**
	fNET	**SCI-MCI**	**p**	0.142	0.565	0.753	0.676	**0.016** (↓)	0.337	0.878
			AUC	0.603	0.553	0.511	0.472	**0.692**	0.447	0.563
		MCI-ADD	**p**	0.571	0.103	0.613	0.687	0.394	0.349	0.345
			AUC	0.505	0.623	0.556	0.523	0.531	0.552	0.556
Schaefer 800	**sNET**	**SCI-MCI**	**p**	0.786	0.444	0.056	0.480	0.835	0.989	0.228
			AUC	0.506	0.560	0.622	0.549	0.487	0.475	0.426
		MCI-ADD	**p**	0.139	0.820	0.078	0.491	0.425	0.473	0.199
			AUC	0.370	0.482	0.374	0.583	0.601	0.560	0.431
	fNET	**SCI-MCI**	**p**	0.283	0.634	0.624	**0.034** (↓)	0.765	0.563	0.319
			AUC	0.530	0.505	0.499	**0.636**	0.537	0.446	0.549
		MCI-ADD	**p**	0.659	**0.020** (↓)	0.830	0.400	0.152	0.934	0.818
			AUC	0.558	**0.681**	0.493	0.568	0.603	0.508	0.487

The assortativity coefficient was calculated for each subnetwork for sNETs and fNETs. Table 4.2 shows Welch's t-test p-value and simple threshold classifier AUC results of sNETs and fNETs. The analysis across different Schaefer scales reveals significant changes in assortativity in key brain networks during cognitive decline.

At the Schaefer 200 scale, sNET shows decreased nodal assortativity in the limbic network as the severity of cognitive decline increases from SCI to MCI (p-val= 0.038) and increased assortativity in the salience/ventral attention network from MCI to ADD (p = 0.047). In contrast, fNET shows increased assortativity in the somatomotor network from MCI to ADD (p = 0.014). At the Schaefer 400 scale, sNET exhibits decreased assortativity in the dorsal attention (p = 0.042) and default networks (p = 0.022) from SCI to MCI, and decreased assortativity in the default network from MCI to ADD. Additionally, fNET shows decreased assortativity in the limbic network (p = 0.016). At the Schaefer 800 scale, fNET displays decreased assortativity in the salience/ventral attention network from SCI to MCI (p = 0.034) and the somatomotor network from MCI to ADD (p = 0.020).

4.2.3. Local (Nodal) Scale

Table 4.3 demonstrates the classification performance achieved through leave-one-out (LOO) cross-validation across the cognitive decline spectrum at 200, 400, and 800 scales. These results suggest that the top 5 discriminating nodes across all group pairs for both sNETs and fNETs revealed that Schaefer 400 exhibited the lowest variance and the highest mean accuracy values, emphasizing its crucial role in ADD classification. Due to these observations, further analyses will concentrate on this specific scale to evaluate its potential as a diagnostic biomarker and to understand its robustness and reliability in clinical applications.

Table 4.3. Classification accuracies for different disease stages (SCI-MCI, MCI-ADD) and spatial scales of the Schaefer atlas (200, 400, and 800). The accuracies of linear SVM classifiers computed over leave-one-out experiments for SCI-vs-MCI and MCI-vs-ADD tasks on sNETs and fNETs, using $5D$ feature vectors composed of nodal assortativity of the statistically most significant nodes.

	Task	**Schaefer 200**	**Schaefer 400**	**Schaefer 800**
sNET	**SCI-MCI**	0.75	0.75	0.75
	MCI-ADD	0.75	**0.80**	0.70
fNET	**SCI-MCI**	0.75	**0.81**	0.72
	MCI-ADD	0.57	**0.75**	0.74

4.3. Measurements Analysis

The exploration of key nodal network measures—nodal degree, strength, clustering coefficient, betweenness centrality, and, most notably, assortativity—aims to capture distinct aspects of connectivity changes during clinical cognitive decline. Nodal assortativity stands out for its ability to reveal nuanced shifts in connectivity organization, highlighting patterns of network resilience and vulnerability that evolve as cognitive impairment progresses. Examining these measures independently across both sNET and fNET provides deeper insights into how specific network components respond as the disease advances from SCI to MCI and ultimately to ADD.

Each measure provides distinct theoretical insights into both local and global connectivity patterns, contributing uniquely to the comprehensive analysis of network structure. By systematically evaluating these measures, the analysis identifies those measures most capable of elucidating network resilience, vulnerability, and adaptability, providing a nuanced understanding of how various brain network components respond to the progression of neurodegeneration.

4.3.1. Nodal Degree

Figure 4.4 presents differential nodal degree maps depicting the results of Welch's t-test applied to assess significant differences in nodal degree between SCI-vs-MCI and MCI-vs-ADD stages within both sNET and fNET. The analysis specifically highlights the statistically significant nodes where connectivity alterations were observed across stages of cognitive decline. For the SCI-vs-MCI comparison, Welch's t-test identified 29 and 21 significant nodes ($p < 0.05$) out of 400 within sNETs and fNETs, respectively.In the MCI-vs-ADD comparison, a greater number of significant nodes—66 in sNETs and 71 in fNETs out of 400 (p-value < 0.05)—were identified. As the disease progresses, the impact becomes more widespread, affecting a larger number of nodes within both networks.

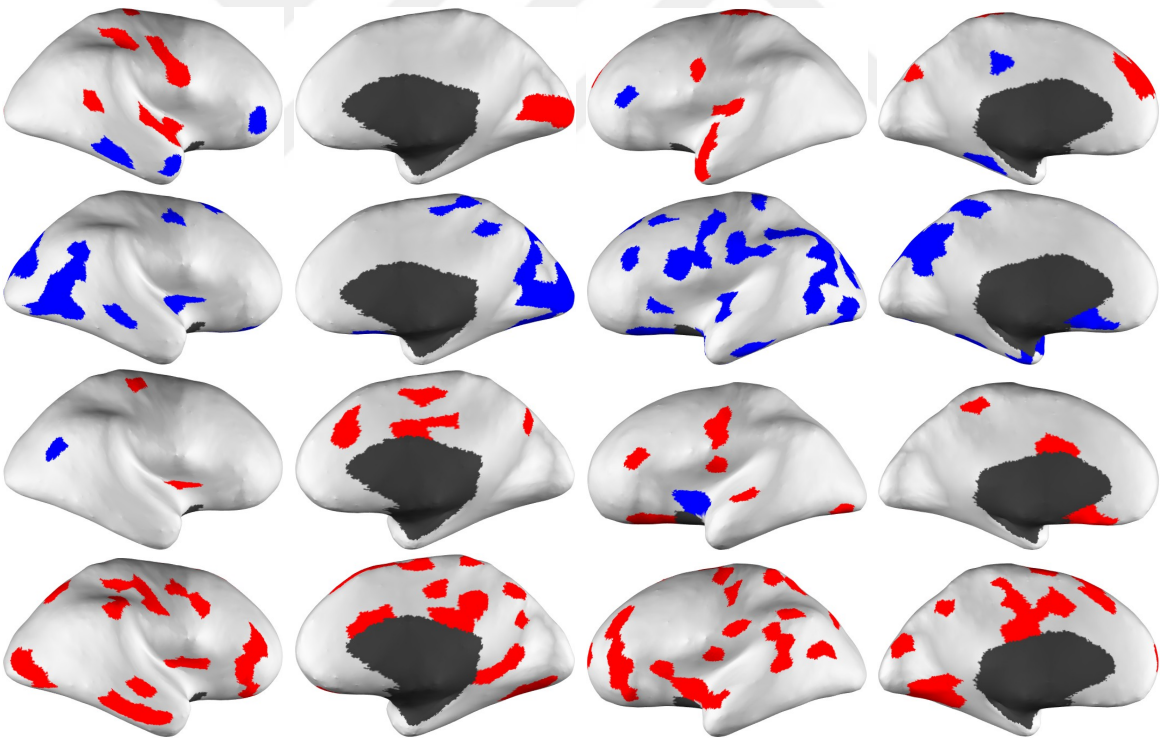

Figure 4.4. Differential nodal degree maps of the statistically significant sNET and fNET locations for SCI-vs-MCI (1st and 3rd row) and MCI-vs-ADD (2nd and 4th row) discrimination, displayed from lateral/medial views of right/left hemispheres, respectively, on inflated brain surface (BrainSurfer) [74]. Cortical regions with statistically significant degree increases/decreases are shown in red/blue, respectively.

The analysis of nodal degree in sNETs and fNETs across different stages of cognitive decline highlights a distinctive pattern. In both networks, nodal degree increases significantly as cognitive decline progresses from SCI to MCI, suggesting an early compensatory mechanism within the network. This increase in connectivity at specific nodes may indicate the brain's attempt to strengthen or form new connections to counterbalance early cognitive impairment. It could reflect compensatory mechanisms or the development of alternative pathways as the brain adapts to initial signs of neurodegeneration. However, as the disease advances from MCI to ADD, the trend diverges between sNETs and fNETs. In sNETs, there is a marked decrease in nodal degree, indicating a breakdown of compensatory mechanisms as Alzheimer's disease progresses. This reduction could signify the loss of connectivity as the neurodegenerative process disrupts established pathways. Conversely, in fNETs, nodal degree continues to increase from MCI to ADD, suggesting that these nodes may remain structurally intact longer or engage in continued reorganization even in advanced stages of disease. This divergence between sNETs and fNETs implies that different network components respond uniquely to advancing pathology.

Statistical assessment of the discriminative power of nodal degree revealed right somatomotor (16), left limbic temporal pole (6), left default prefrontal cortex (13), right somatomotor (34), right visual (19) as the top 5 significant sNET nodes, left somatomotor (13), left somatomotor (17), right control precuneus (1), left default temporal (8), left visual (6), as the top 5 significant fNET nodes for SCI-vs-MCI classification. The corresponding top 5 significant sNET and fNET nodes for MCI-vs-ADD classification are left visual (1), right visual (28), left dorsal attention posterior (3), left visual (6), right visual (26), and left visual (10), right default dorsal prefrontal cortex medial prefrontal cortex (13), left visual (11), right default temporal (2), right salience / ventral attention precentral (1), respectively.

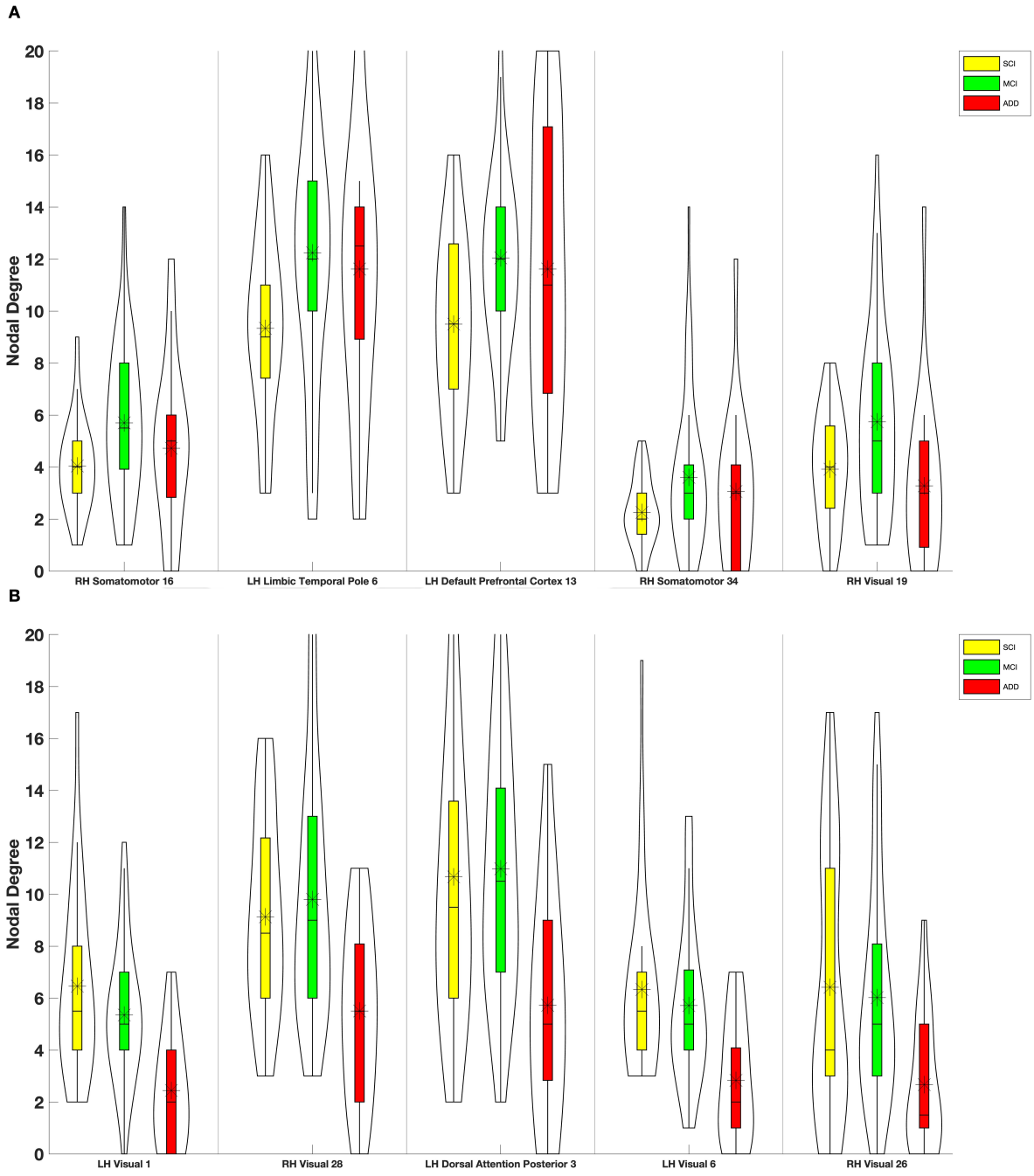

Figure 4.5. Distributions of the nodal degree of the top 5 most discriminative sNET nodes are shown for SCI-vs-MCI ($p < 0.011$) at the top panel and for MCI-vs-ADD ($p < 0.001$) at the bottom panel. A significant nodal degree increase is observed in the transition from SCI to MCI. In contrast, a statistically significant decrease is observed in the transition from MCI to ADD.

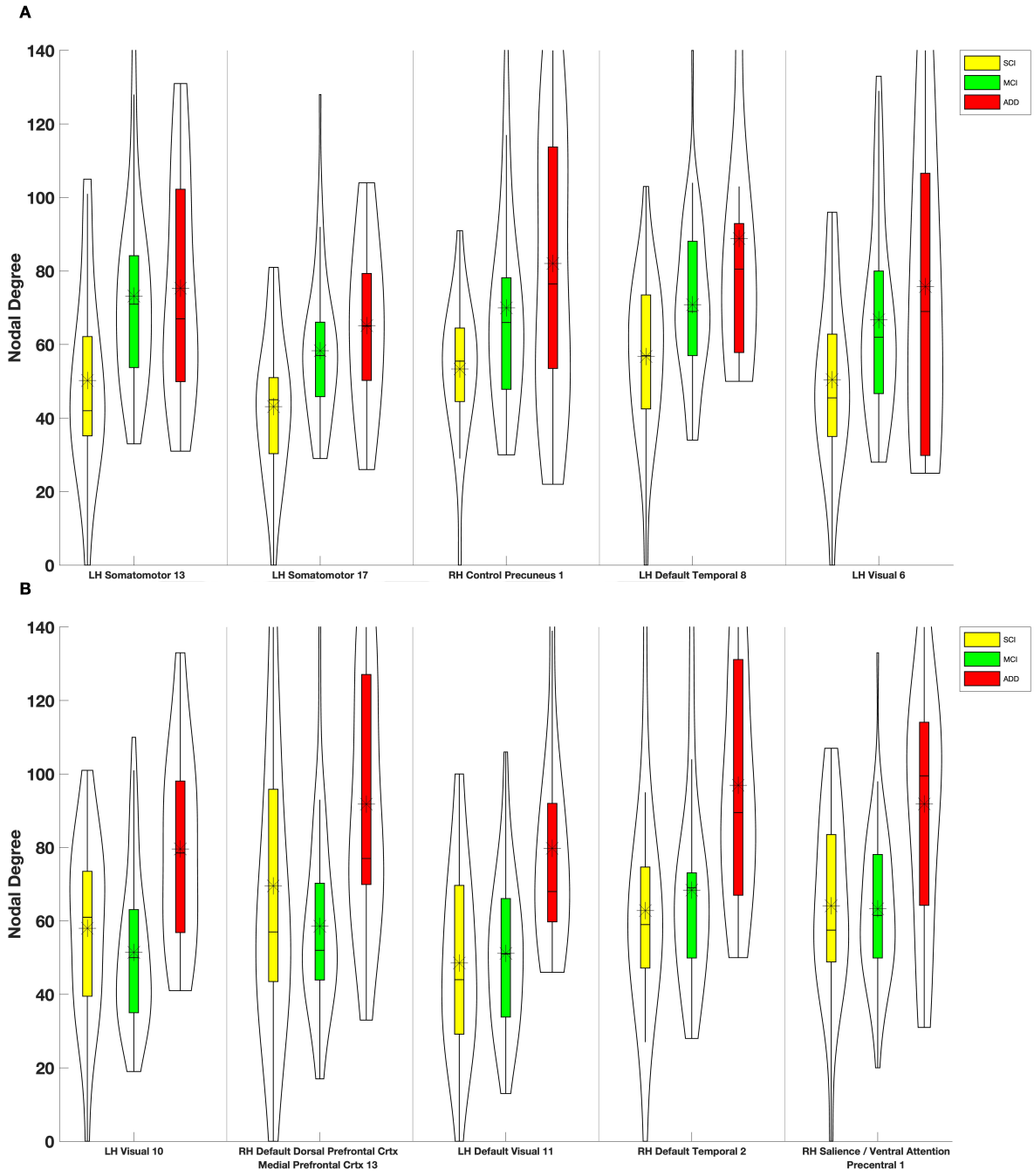

Figure 4.6. Distributions of the nodal degree of the top 5 most discriminative fNET nodes are shown for SCI-vs-MCI ($p < 0.011$) at the top panel and for MCI-vs-ADD ($p < 0.003$) at the bottom panel. A significant nodal degree increase is observed in the transition from SCI to MCI and MCI to ADD, albeit at mutually exclusive sets of nodes (cortical regions).

Figure 4.5 reports the distribution of the nodal degree of selected sNET nodes across all 3 groups. Figure 4.5A reveals a significant increase in the nodal degree as the severity of cognitive decline increases from SCI to MCI ($p < 0.011$) for all sNET nodes that are in the top 5 in terms of their statistical significance for SCI-MCI classification. The consistent upward trend observed in the early stages of the disease changes to a downward trend during the transition from MCI to ADD, the second stage of the disease. The top 5 sNET nodes with the highest discriminative power for MCI vs. ADD classification demonstrate a decrease from MCI to ADD ($p < 0.001$), as illustrated in Figure 4.5B. It is noteworthy that these two sets of nodes are mutually exclusive.

Figure 4.6 reports the identical statistical analysis of nodal degree for fNETs. Similarly to sNETs, data in Figure 4.6A reveals a statistically significant increase in the nodal degree of selected fNET nodes as the severity of cognitive decline increases from SCI to MCI ($p < 0.011$). Unlike sNET, the top 5 fNET nodes with the highest discriminative power for

4.3.2. Nodal Strength

Figure 4.7 visualizes statistically significant differences in nodal strength across SCI-vs-MCI and MCI-vs-ADD comparisons within both sNET and fNET. This figure highlights nodes where significant alterations in strength are observed, providing insights into the network-level changes associated with different stages of cognitive decline. In the sNET, the analysis identified 45 nodes with significant p-values ($p < 0.05$) for the SCI-vs-MCI comparison and 15 significant nodes ($p < 0.05$) for the MCI-vs-ADD comparison, out of 400 nodes. In the sNET, the analysis identified 45 nodes with significant p-values for the SCI-vs-MCI comparison, indicating areas where nodal strength changes significantly in the early transition from SCI to MCI. However, as the disease progresses from MCI to ADD, the number of significant nodes in the sNET decreases to 15, suggesting a more targeted yet intensified impact on specific structural connections as Alzheimer's pathology advances. This reduction could reflect the network's diminishing capacity for structural compensation.

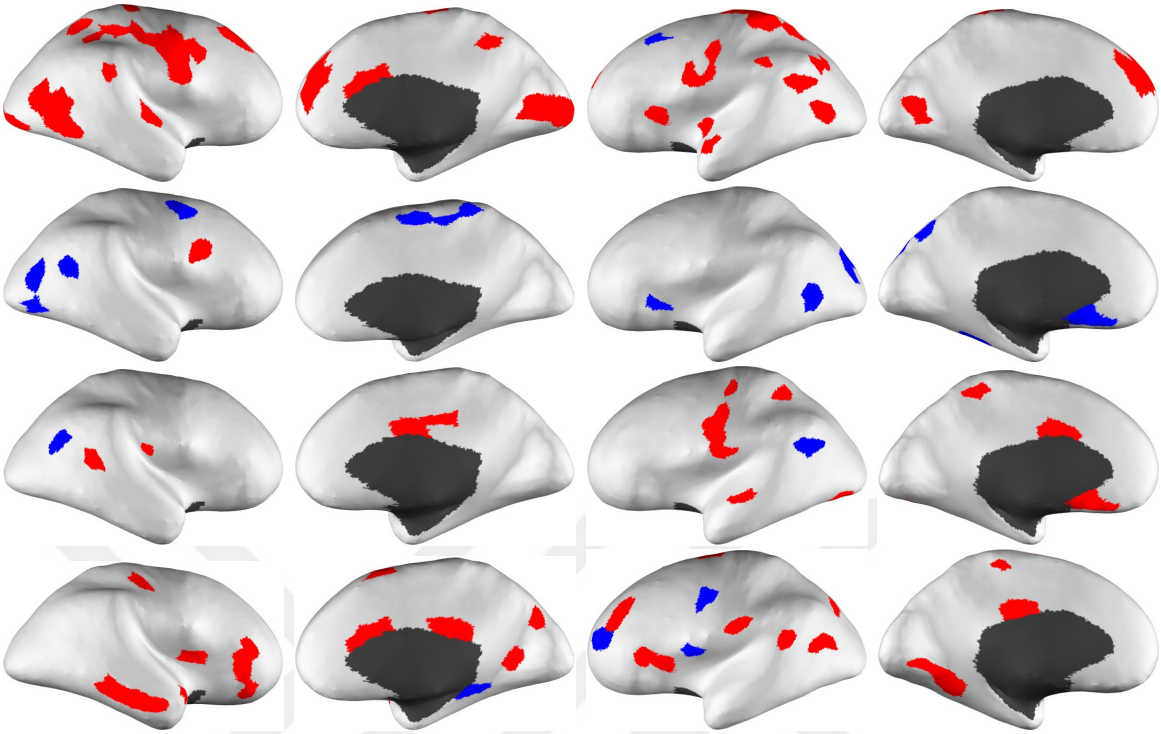

Figure 4.7. Differential nodal strength maps of the statistically significant sNET locations for SCI-vs-MCI (1st row), MCI-vs-ADD (2nd row) discrimination and fNET locations for SCI-vs-MCI (3rd row), MCI-vs-ADD (4th row) discrimination. The cortical regions with a statistically significant increase/ decrease in strength with increasing cognitive decline are depicted in red/blue, respectively.

In the fNET, Welch's t-test identified 17 and 30 significant nodes ($p < 0.05$) out of a total of 400 in the SCI-vs-MCI and MCI-vs-ADD comparisons, respectively, most of which show increased strength. This increase in significant nodes in the MCI-vs-ADD transition may indicate that functional connectivity continues to adapt, possibly through compensatory reorganization, even as structural connectivity begins to wane. The broader distribution of significant nodes in the fNET during later stages suggests that fNET may attempt to compensate by strengthening connectivity in certain regions to support cognitive processes that are increasingly impaired as the disease progresses.

The analysis of nodal strength, reflecting the cumulative weight of connections at each node, reveals a similar compensatory pattern to the nodal degree in early disease stages. For both sNETs and fNETs, there is a significant increase in nodal strength from SCI to MCI. This suggests that these nodes play a prominent role in early compensatory mechanisms, supporting cognitive function by enhancing connectivity. However, in sNETs, the trend reverses as the disease progresses from MCI to ADD, with nodal strength showing a notable decrease. This decline likely reflects the erosion of these previously strengthened connections, consistent with the progression of neurodegenerative damage in Alzheimer's disease. Interestingly, in fNETs, nodal strength continues to increase from MCI to ADD, indicating a different adaptation response in functional networks. This suggests that while structural networks may deteriorate, functional networks might retain or even enhance connectivity in an attempt to maintain cognitive function despite widespread network degeneration.

Statistical assessment of the discriminative power of nodal strength revealed left Somatomotor (35), right somatomotor (16), left somatomotor (31), right Somatomotor (39), right default dorsal prefrontal cortex medial prefrontal cortex (4), as the top 5 significant sNET nodes, left somatomotor (17), left somatomotor (13), left limbic orbital frontal cortex (4), left salience / ventral Attention Medial (6), left somatomotor (11) as the top 5 significant fNET nodes for SCI-vs-MCI classification. The corresponding top 5 significant sNET and fNET nodes for MCI-vs-ADD classification are left default precuneus posterior cingulate cortex (10), left visual (1), left somatomotor (33), left Visual (30), left Control Parietal (4) and left visual (10), right somatomotor (23), right default ventral prefrontal cortex (3), left somatomotor (23), right control temporal (1), respectively.

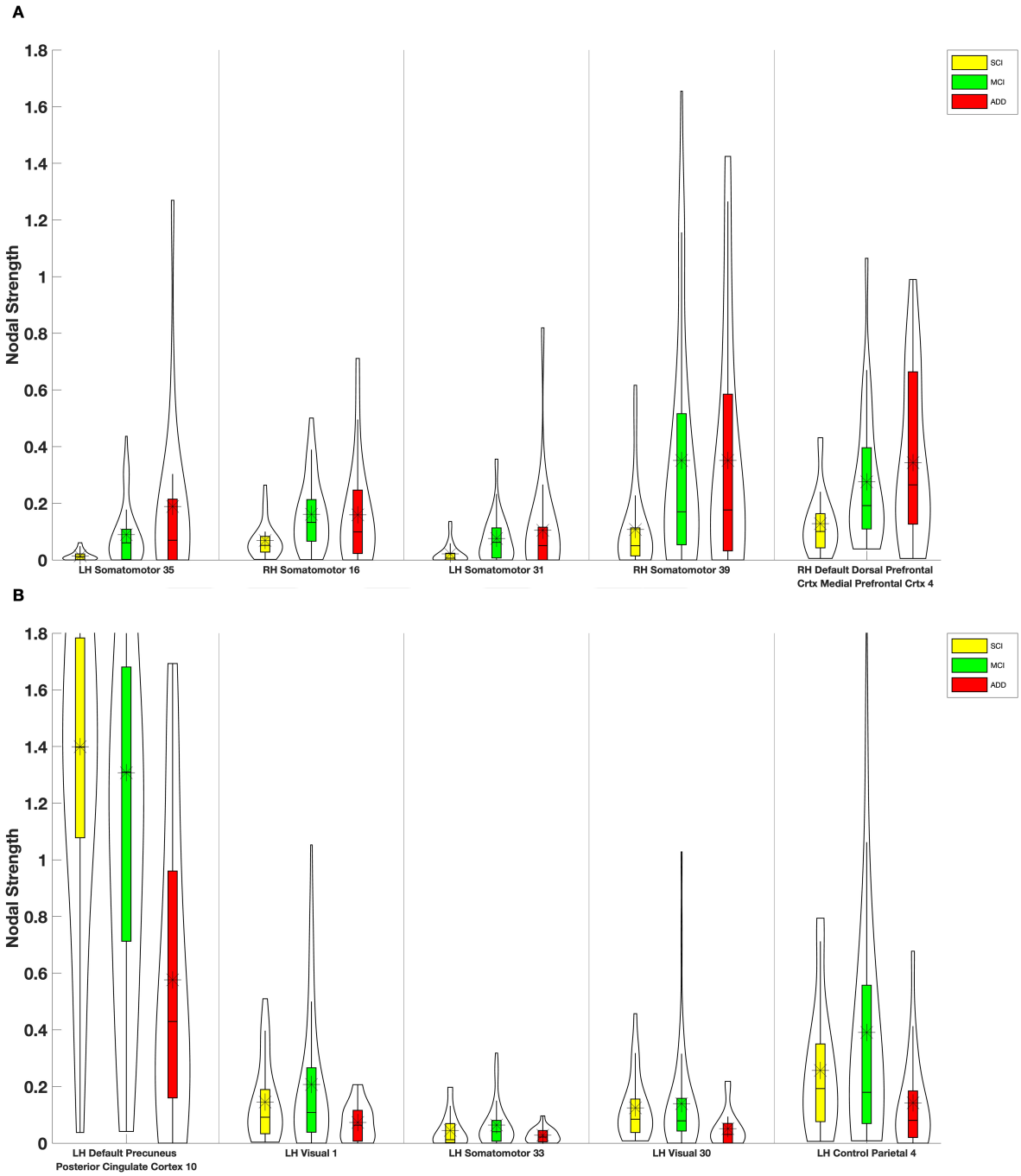

Figure 4.8. Distributions of nodal strength of the top 5 most discriminative sNET nodes are shown for SCI-vs-MCI ($p < 0.001$) at the top panel and for MCI-vs-ADD ($p < 0.008$) at the bottom panel. A statistically significant increase in nodal strength is observed in the transition from SCI to MCI. In contrast, a statistically significant decrease is observed in the transition from MCI to ADD.

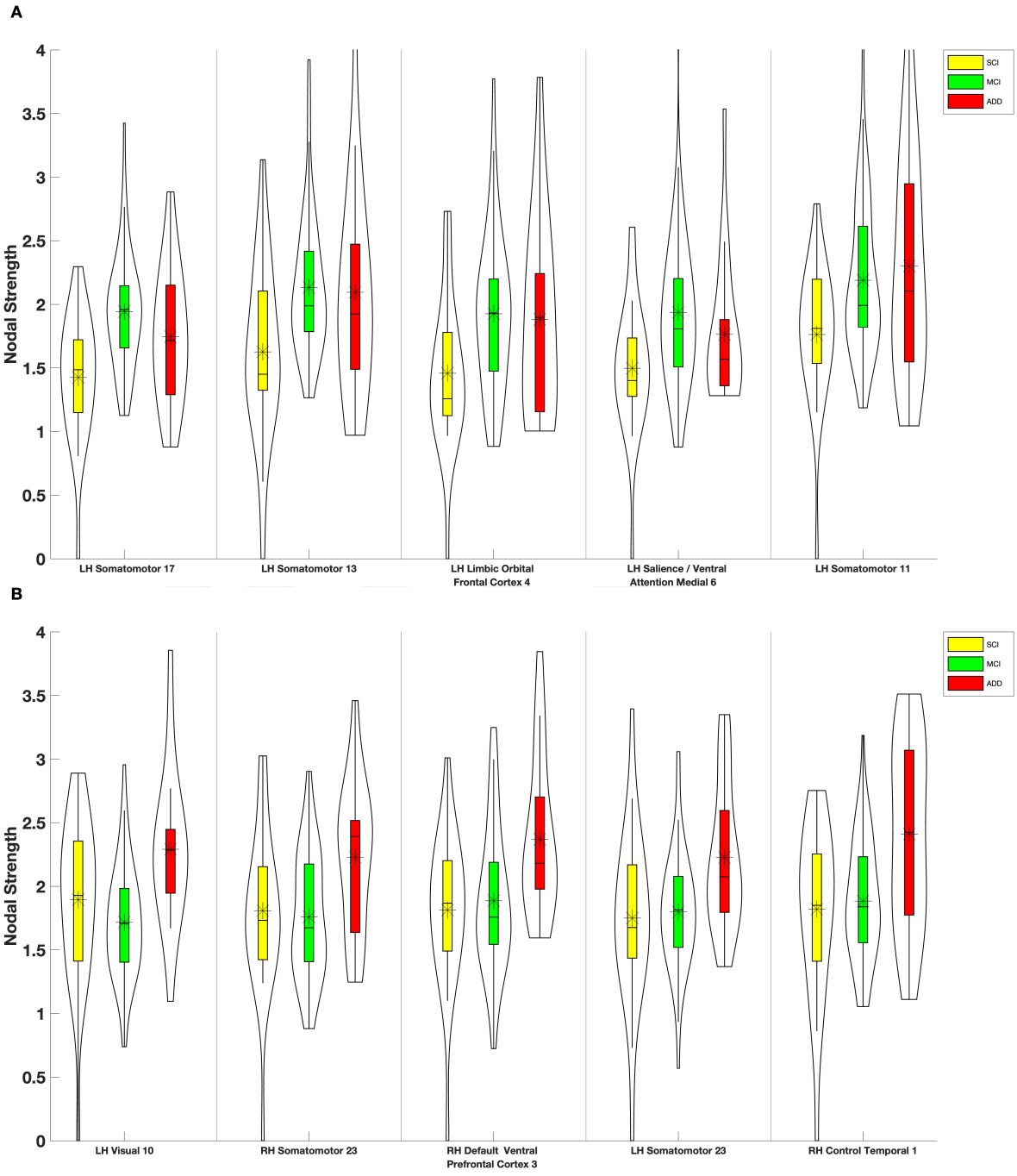

Figure 4.9. Distributions of nodal strength of the top 5 most discriminative fNET nodes are shown for SCI-vs-MCI ($p < 0.006$) at the top panel and for MCI-vs-ADD ($p < 0.001$) at the bottom panel. A statistically significant increase in nodal strength is observed throughout the disease progression in fNET, albeit at mutually exclusive sets of nodes (cortical regions).

Figure 4.8 reports the distribution of the nodal strength of selected sNET nodes across all 3 groups. Figure 4.8A reveals a significant increase in the nodal strength as the severity of cognitive decline increases from SCI to MCI ($p < 0.001$) for all sNET nodes that are in the top 5 in terms of their statistical significance for SCI-MCI classification. The consistent upward trend observed in the early stages of the disease changes to a downward trend during the transition from MCI to ADD, the second stage of the disease. The top 5 sNET nodes with the highest discriminative power for MCI vs. ADD classification demonstrate a decrease from MCI to ADD ($p < 0.008$), as illustrated in Figure 4.8B. It is noteworthy that these two sets of nodes are mutually exclusive. MCI-vs-ADD classification show an increase from MCI to ADD ($p < 0.003$), as shown in Figure 4.6B. These two sets of nodes are mutually exclusive.

Figure 4.9 reports the identical statistical analysis of nodal strength for fNETs. Similarly to sNETs, data in Figure 4.9A reveals a statistically significant increase in nodal strength of selected fNET nodes as the severity of cognitive decline increases from SCI to MCI ($p < 0.006$). Unlike sNET, the top 5 fNET nodes with the highest discriminative power for MCI-vs-ADD classification show an increase from MCI to ADD ($p < 0.001$), as shown in Figure 4.9B. These two sets of nodes are also mutually exclusive.

4.3.3. Nodal Clustering Coefficient

Figure 4.10 illustrates the differential nodal clustering coefficient maps that display the statistically significant locations across the sNET and fNET for the SCI-vs-MCI and MCI-vs-ADD comparisons. Using Welch's t-test, nodes with significant differences in clustering coefficients were identified for each comparison, shedding light on network reorganization patterns that accompany cognitive decline. Specifically, the comparison between SCI and MCI identified significant differences in 36 out of 400 sNET nodes ($p < 0.05$), highlighting areas where structural organization changes during early disease stages.However, comparing MCI and ADD revealed fewer significant differences, with only 21 out of 400 sNET nodes showing significant changes ($p < 0.05$),

suggesting that structural changes may slow down as the disease progresses.

In the fNET, a contrasting pattern was observed. Welch's t-test revealed only 10 significant nodes in the SCI-vs-MCI comparison, suggesting limited fNET reorganization between these initial stages. However, in the MCI-vs-ADD comparison, a substantially higher count of 56 nodes ($p < 0.05$), out of 400, exhibited significant clustering coefficient differences, signaling a more extensive alteration in fNET clustering as the disease progresses to the ADD stage. This sharp increase in affected nodes within the fNET suggests an adaptive or compensatory reorganization within functional connections as structural deterioration intensifies.

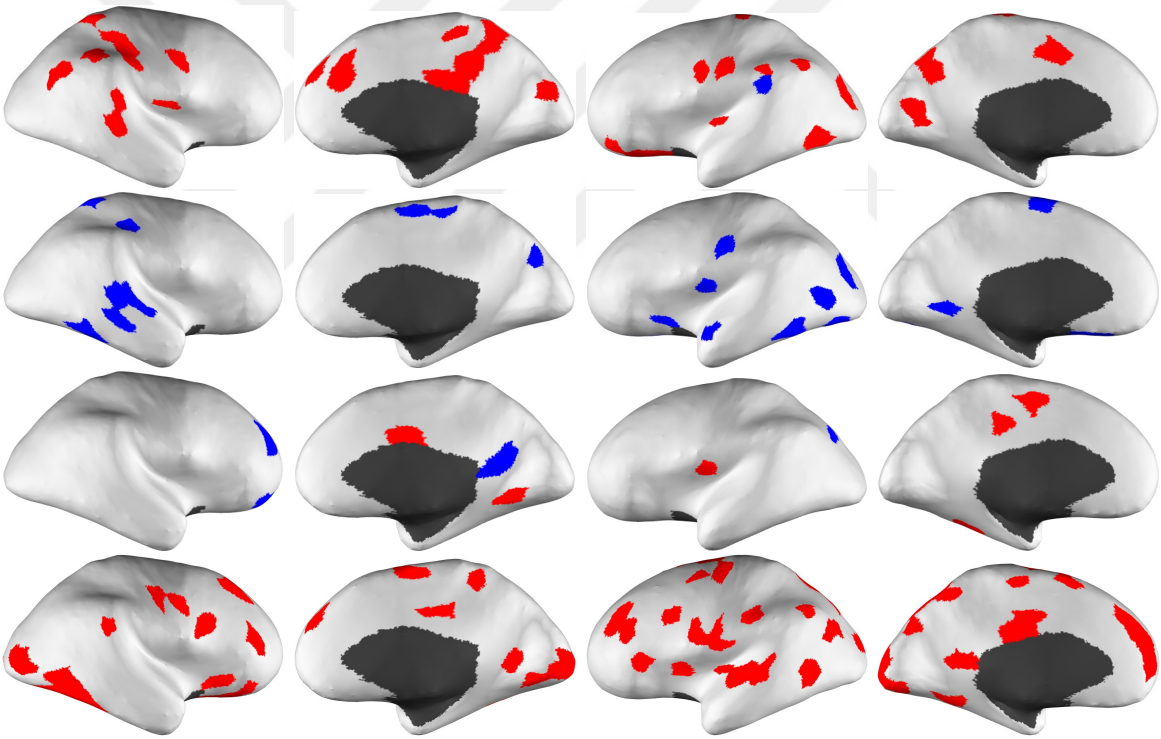

Figure 4.10. Differential nodal clustering coefficient maps of the statistically significant sNET locations for SCI-vs-MCI (1st row), MCI-vs-ADD (2nd row) discrimination and fNET locations for SCI-vs-MCI (3rd row), MCI-vs-ADD (4th row) discrimination. In the SCI-to-MCI transition, sNET shows substantial clustering changes with 36 significant nodes, while fNET has limited changes.

In the SCI-vs-MCI comparison, nodes with increased clustering in both networks may reflect early compensatory mechanisms, attempting to maintain local connectivity as cognitive decline begins. Conversely, the MCI-vs-ADD comparison highlights areas with reduced clustering, likely indicating the breakdown of local network cohesion due to advancing neurodegeneration. These findings suggest that clustering coefficient changes in the sNET occur earlier in the disease course, while the fNET exhibits more extensive reorganization in later stages, reflecting a complex interplay between structural degradation and functional adaptation in the progression of Alzheimer's disease.

Statistical assessment of the discriminative power of nodal clustering coefficients revealed right hemisphere default dorsal prefrontal cortex medial prefrontal cortex (7), right somatomotor (18), left somatomotor (35), left control precuneus (1), left somatomotor (14), as the top 5 significant sNET nodes, left somatomotor (16), right somatomotor (23), right salience / ventral attention temporal occipital parietal (6), right salience / ventral attention medial (6), right default parietal (2), as the top 5 significant fNET nodes for SCI-vs-MCI classification. The corresponding top 5 significant sNET and fNET nodes for MCI-vs-ADD classification are left salience / ventral attention medial (7), left control ventral prefrontal cortex (1), right salience / ventral attention medial (7), right visual (28), right somatomotor 2, and right salience / ventral attention temporal occipital parietal (6), left default prefrontal cortex 6, right somatomotor (16), left salience / ventral attention frontal operculum insula (2), left Control Lateral prefrontal Cortex (7), respectively.

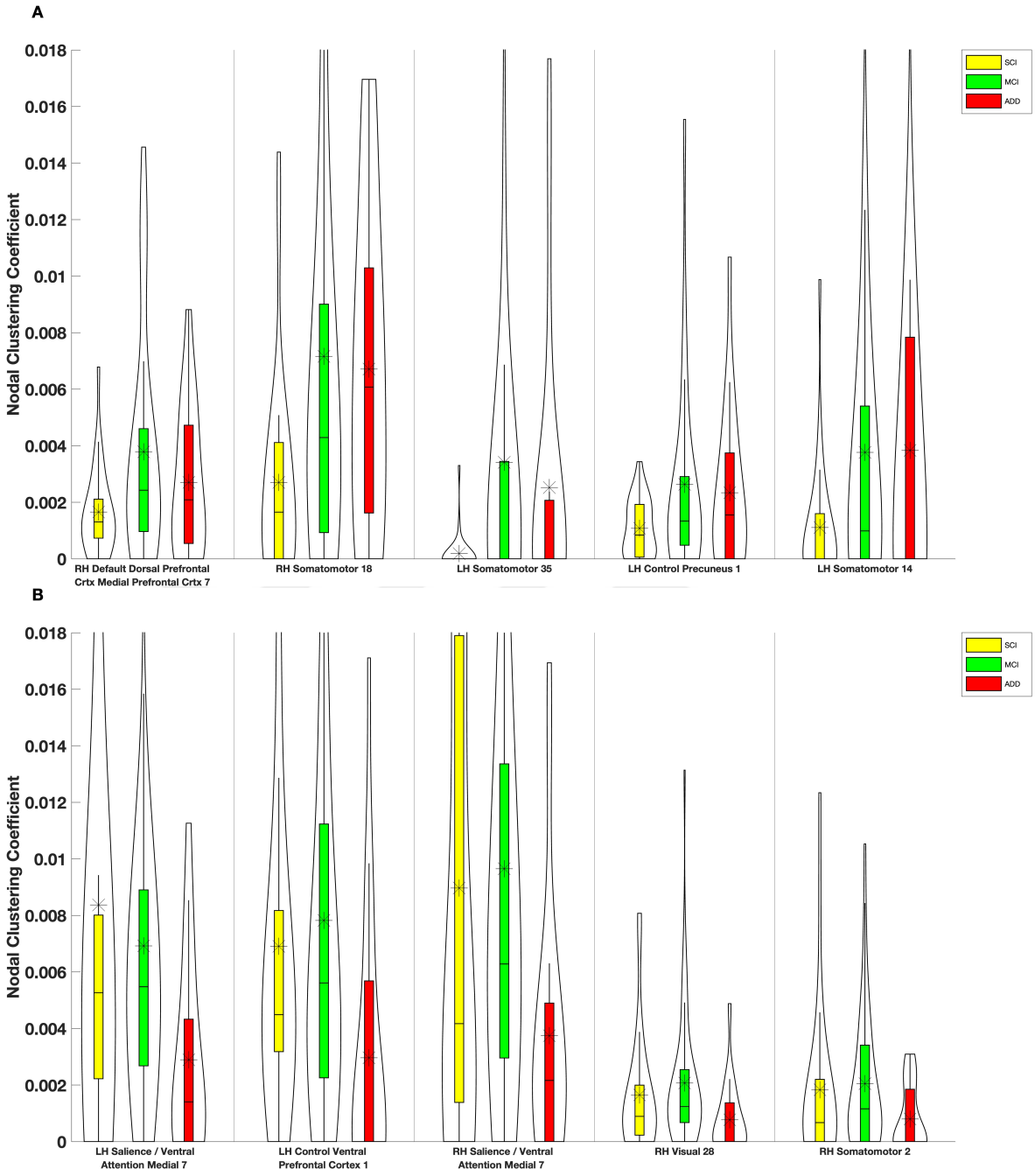

Figure 4.11. Distributions of nodal clustering coefficient of the top 5 most discriminative sNET nodes are shown for SCI-vs-MCI ($p < 0.011$) at the top panel and for MCI-vs-ADD ($p < 0.009$) at the bottom panel. A statistically significant increase in the nodal clustering coefficient is observed during the SCI to MCI transition, while a decrease is observed during the MCI to ADD transition.

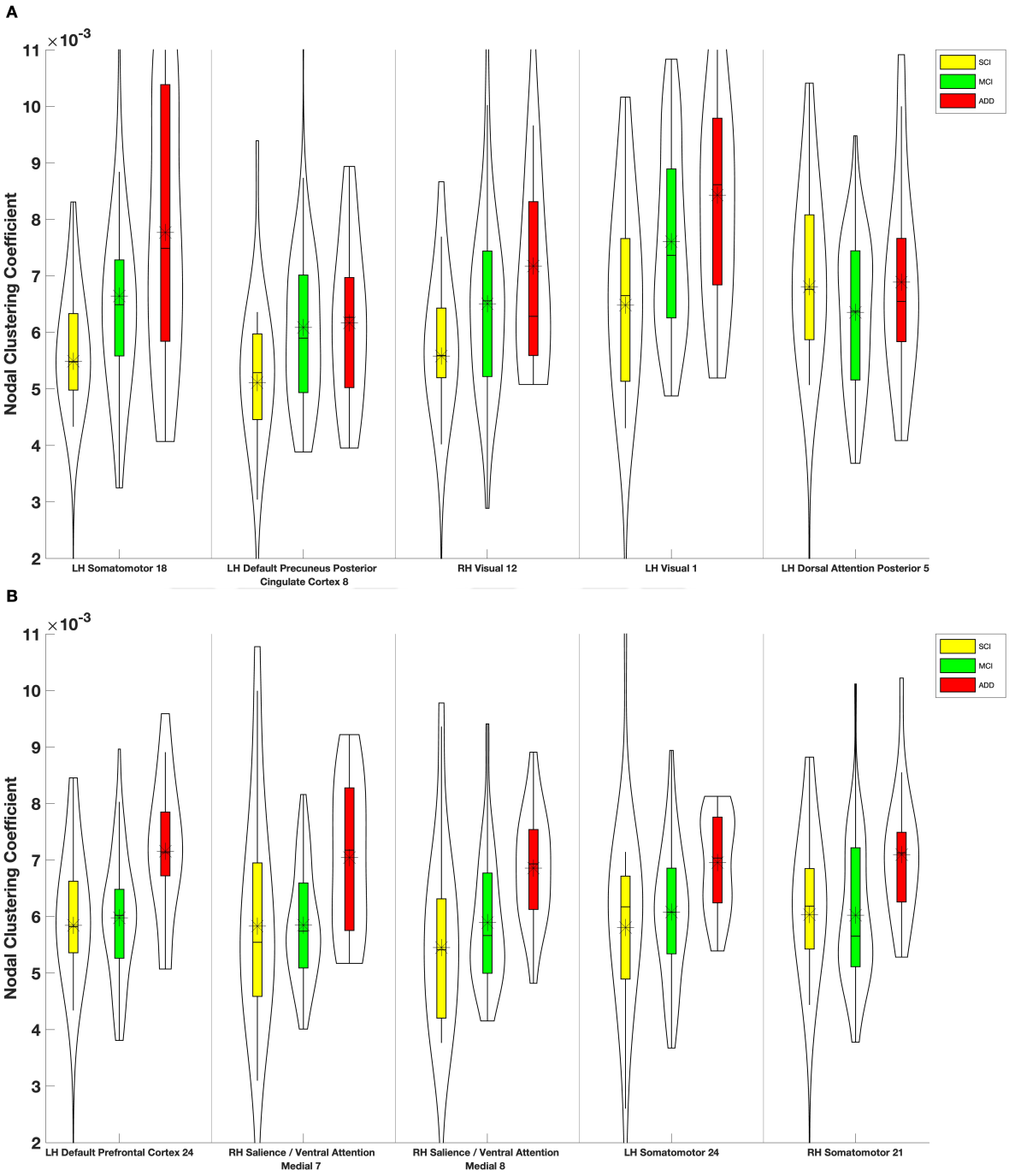

Figure 4.12. Distributions of nodal clustering coefficient of the top 5 most discriminative fNET nodes are shown for SCI-vs-MCI ($p < 0.031$) at the top panel and for MCI-vs-ADD ($p < 0.003$) at the bottom panel. A statistically significant increase in nodal clustering coefficient is observed in the transition from SCI to MCI, and MCI to ADD, albeit at mutually exclusive sets of nodes.

Figure 4.11 reports the distribution of the nodal clustering coefficient of selected sNET nodes across all 3 groups. Figure 4.11A reveals a significant increase in the nodal clustering coefficient as the severity of cognitive decline increases from SCI to MCI ($p < 0.011$) for all sNET nodes that are in the top 5 in terms of their statistical significance for SCI-MCI classification. The consistent upward trend observed in the early stages of the disease changes to a downward trend during the transition from MCI to ADD, the second stage of the disease. The top 5 sNET nodes with the highest discriminative power for MCI vs. ADD classification demonstrate a decrease from MCI to ADD ($p < 0.009$), as illustrated in Figure 4.11B. It is noteworthy that these two sets of nodes are mutually exclusive.

Figure 4.12 reports the identical statistical analysis of the nodal clustering coefficient for fNETs. Similarly to sNETs, data in Figure 4.12A reveals a statistically significant increase in the clustering coefficient of selected fNET nodes as the severity of cognitive decline increases from SCI to MCI ($p < 0.031$). Unlike sNET, the top 5 fNET nodes with the highest discriminative power for MCI-vs-ADD classification show an increase from MCI to ADD ($p < 0.003$), as shown in Figure 4.12B. These two sets of nodes are also mutually exclusive.

4.3.4. Nodal Betweenness Centrality

Betweenness centrality provides insights into nodes that serve as communication bridges within the network. Figure 4.13 illustrates the differential maps of nodal betweenness centrality, highlighting regions with statistically significant differences between the SCI-vs-MCI and MCI-vs-ADD stages in both sNET and fNET. Using Welch's t-test, the analysis identified specific nodes with altered betweenness centrality, reflecting changes in the central roles that particular nodes play within the network as Alzheimer's disease progresses.

Out of 400 nodes, 16 significant nodes (p-value < 0.05) were identified, and the majority of these nodes exhibited increased betweenness centrality. This increase

could reflect an early compensatory mechanism, where specific structural pathways become more central to support connectivity as mild cognitive impairment begins. This increase might be an attempt by the network to redirect connectivity through alternative pathways in response to the initial stages of degeneration. In the fNET for the SCI-vs-MCI comparison, 19 nodes exhibited significant differences in betweenness centrality, underscoring functional adaptations occurring alongside structural changes. The predominance of nodes with increased betweenness centrality likely reflects compensatory mechanisms intended to preserve network connectivity in response to early neurodegeneration.

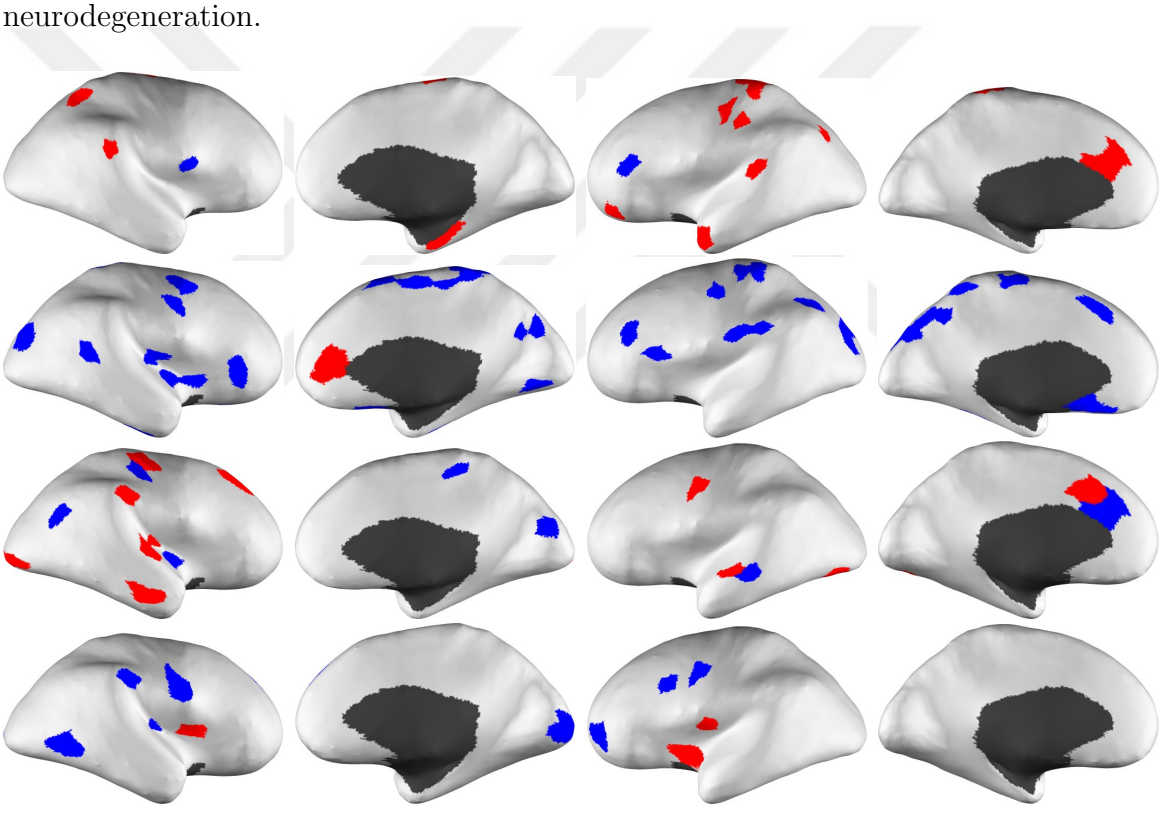

Figure 4.13. Differential nodal betweenness centrality maps of the statistically significant sNET and fNET locations for SCI-vs-MCI (1st and 3rd row) and MCI-vs-ADD (2nd and 4th row) discrimination, respectively. Betweenness centrality increases in 36 sNET and 19 fNET significant nodes during the early disease stage, but decreases in 39 sNET and 12 fNET significant nodes during the later stage.

In the MCI-vs-ADD comparison, 39 nodes were identified with significant changes in betweenness centrality in the sNET. Many of these nodes showed decreased betweenness centrality, reflecting a substantial breakdown in the structural integrity of the network as the disease advances. This loss of centrality indicates that previously crucial pathways are deteriorating, making the network less resilient and adaptable. In the fNET for the MCI-vs-ADD stage, 12 nodes exhibited significant changes in betweenness centrality, with only 3 nodes showing increased centrality. This limited increase suggests that as neurodegeneration advances, the network's ability to compensate functionally is severely constrained. The majority of nodes demonstrated decreased betweenness centrality, indicating a widespread loss of functional integration and connectivity. This imbalance reflects the network's reduced adaptability, as fewer nodes can adjust their roles to support connectivity, marking a progression from early compensatory mechanisms to a stage where functional decline predominates.

Statistical assessment of the discriminative power of nodal betweenness centrality revealed left default prefrontal cortex (12), left somatomotor (29), right limbic temporal pole (7), left somatomotor (36), right somatomotor (39) as the top 5 significant sNET nodes, left Somatomotor (16), right Somatomotor (23), right salience / ventral attention temporal occipital parietal (6), right salience / ventral attention medial (6), right default parietal (2), as the top 5 significant fNET nodes for SCI-vs-MCI classification. The corresponding top 5 significant sNET and fNET nodes for MCI-vs-ADD classification are left hemisphere default precuneus posterior cingulate cortex (10), left hemisphere visual (1), left hemisphere somatomotor (33), left hemisphere visual (30), left hemisphere control parietal (4), and right salience / ventral attention temporal occipital parietal (6), left default prefrontal cortex (6), right somatomotor (16), left salience / ventral attention frontal operculum insula (2), left control lateral prefrontal cortex (7), respectively.

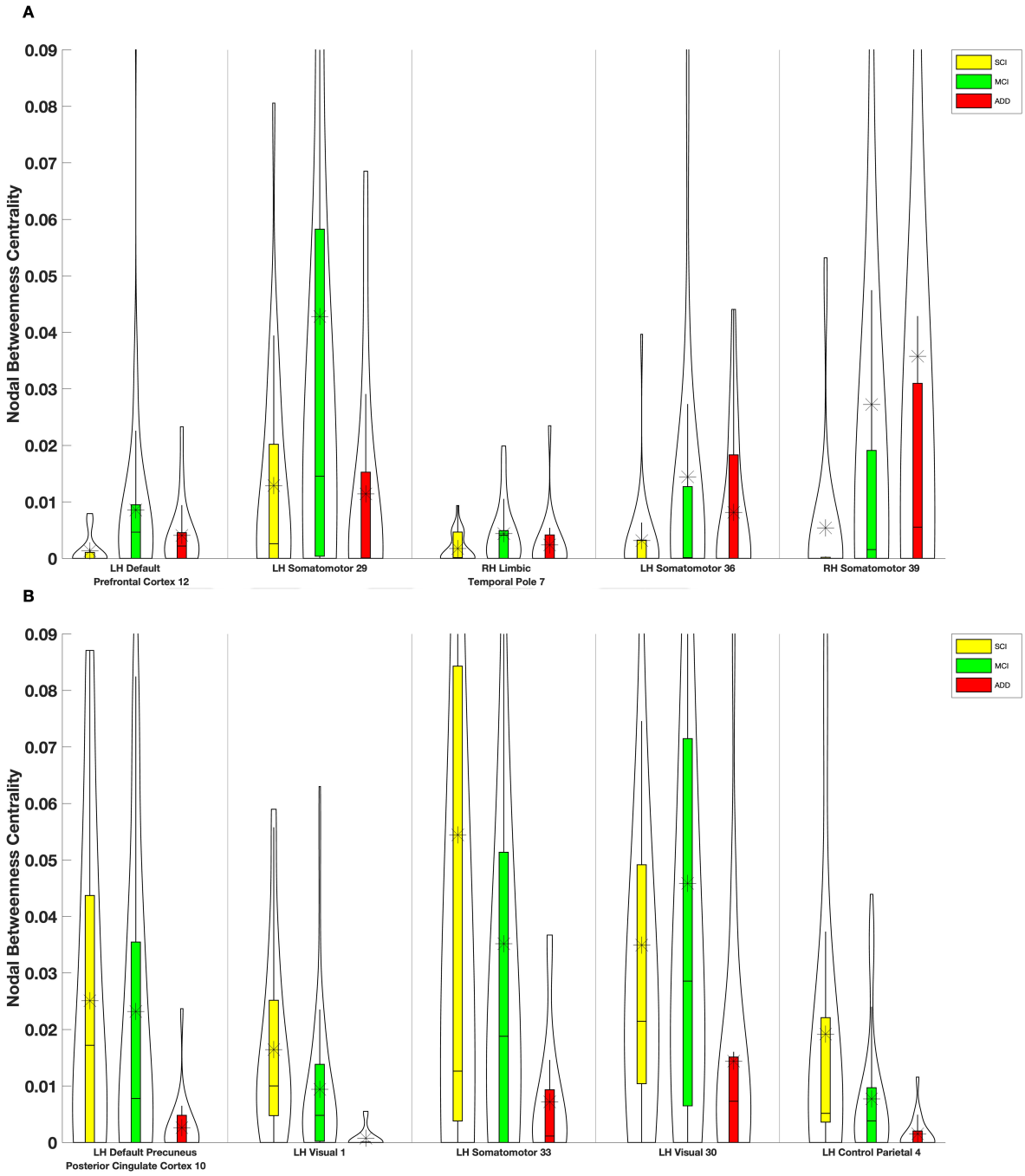

Figure 4.14. Distributions of nodal betweenness centrality of the top 5 most discriminative sNET nodes are shown for SCI-vs-MCI ($p < 0.02$) at the top panel and for MCI-vs-ADD ($p < 0.001$) at the bottom panel. A statistically significant increase in nodal clustering coefficient is observed in the transition from SCI to MCI, while a statistically significant decrease is observed in the transition from MCI to ADD.

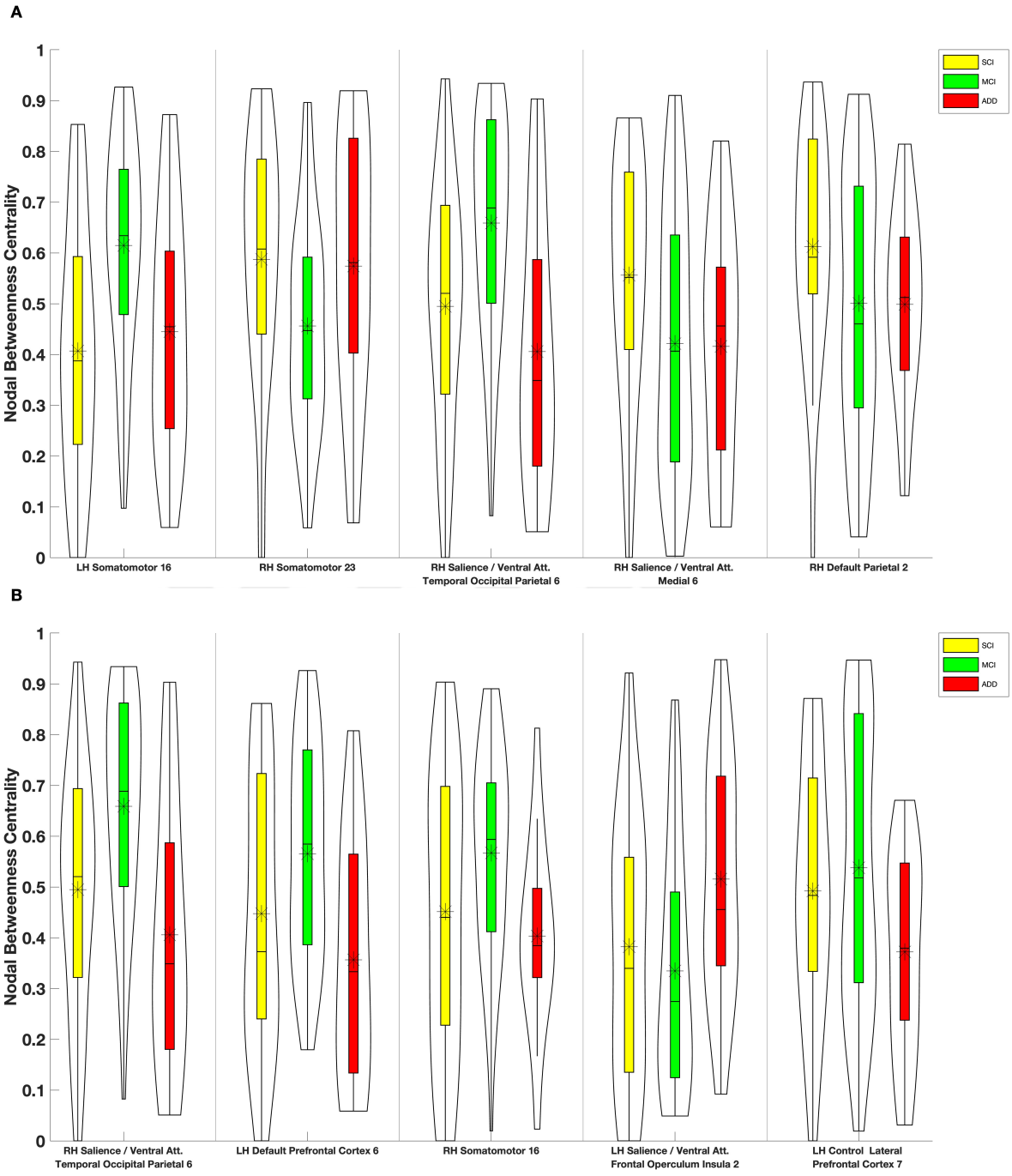

Figure 4.15. Distributions of nodal betweenness centrality of the top 5 most discriminative fNET nodes are shown for SCI-vs-MCI ($p < 0.001$) and MCI-vs-ADD ($p < 0.01$), respectively. There is no consistent increase or decrease in nodal betweenness centrality during the SCI to MCI transition, while a statistically significant decrease is observed during the MCI to ADD transition, except one node.

Figure 4.14 reports the distribution of the nodal betweenness centrality of selected sNET nodes across all 3 groups. Figure 4.14A reveals a significant increase in the nodal betweenness centrality as the severity of cognitive decline increases from SCI to MCI ($p < 0.021$) for all sNET nodes that are in the top 5 in terms of their statistical significance for SCI-MCI classification. The consistent upward trend observed in the early stages of the disease changes to a downward trend during the transition from MCI to ADD, the second stage of the disease. The top 5 sNET nodes with the highest discriminative power for MCI vs. ADD classification demonstrate a decrease from MCI to ADD ($p < 0.002$), as illustrated in Figure 4.14B. It is noteworthy that these two sets of nodes are mutually exclusive.

Figure 4.15 reports the identical statistical analysis of nodal betweenness centrality for fNETs. Data in Figure 4.15A reveals no consistent increase or decrease in nodal betweenness centrality of selected fNET nodes as the severity of cognitive decline increases from SCI to MCI ($p < 0.009$). Unlike the first stage of the disease, the top 5 fNET nodes with the highest discriminative power for MCI-vs-ADD classification show a decrease from MCI to ADD ($p < 0.011$) except one node, left salience / ventral attention frontal operculum insula (2), as shown in Figure 4.15B. These two sets of nodes are also mutually exclusive.

4.3.5. Nodal Assortativity

Figure 4.16 presents differential nodal assortativity maps derived from Welch's t-test, showing statistically significant differences in nodal assortativity between stages of cognitive decline (SCI-vs-MCI and MCI-vs-ADD) across both sNET and fNET. In the sNET, 19 nodes were identified with significant p-values (p ¡ 0.05) in the SCI-vs-MCI comparison, while 42 nodes reached significance in the MCI-vs-ADD comparison, out of 400 nodes. For the fNET, the analysis revealed 47 significant nodes in the SCI-vs-MCI comparison and 24 significant nodes in the MCI-vs-ADD comparison.

In the SCI-to-MCI comparison, a significant decrease in nodal assortativity appears for 19 nodes in the sNET and 47 nodes in the fNET. Nodes with a decrease in assortativity signify a shift toward disassortative connectivity, which tends to increase vulnerability on a local scale. This disassortative pattern is often linked to higher vulnerability at the nodal level, as nodes diversify their connections and play a more central role in communication. This pattern is particularly noticeable in the SCI-to-MCI transition, suggesting that certain nodes are actively adjusting to early neurodegenerative disruptions by establishing alternative communication pathways, which may facilitate faster local interactions. In the MCI-to-ADD comparison, a notable increase in nodal assortativity is observed for 42 nodes in the sNET and 24 nodes in the fNET. This increase reflects a shift towards more assortative connections, where similar nodes preferentially connect. Such a pattern may indicate reduced network flexibility and resilience as the disease advances, as the brain relies on more homogeneous connectivity among similar regions.

Statistical assessment of the discriminative power of nodal assortativities, as described in Section 3.3 revealed right control medial posterior prefrontal cortex (1), right dorsal attention frontal eye fields (2), right default dorsal prefrontal cortex medial prefrontal cortex (5), left default temporal (8), left salience / ventral attention medial (6), as the top 5 significant sNET nodes, right control lateral prefrontal cortex (10), right somatomotor (13), left visual (21), right default precuneus posterior cingulate cortex (3), right default precuneus posterior cingulate cortex (1), as the top 5 significant fNET nodes for SCI-vs-MCI classification. The corresponding top 5 significant sNET and fNET nodes for MCI-vs-ADD classification are left default precuneus posterior cingulate cortex (11), salience / ventral attention medial (3), left default precuneus posterior cingulate cortex (3), right visual (16), left visual (25) and left somatomotor (22), right default dorsal prefrontal cortex medial prefrontal cortex (9), left limbic temporal pole (8), left control parietal (5), left somatomotor (5), respectively.

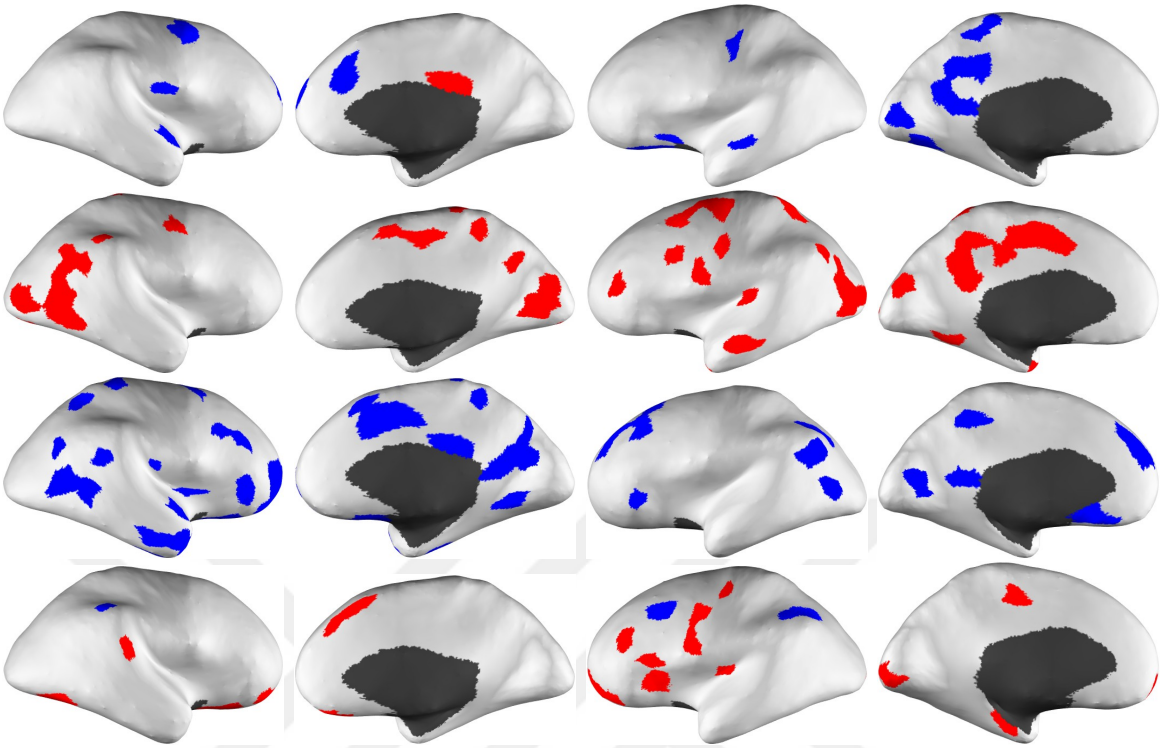

Figure 4.16. Differential nodal assortativity maps of the statistically significant sNET and fNET locations for SCI-vs-MCI (1st and 3rd row) and MCI-vs-ADD (2nd and 4th row) discrimination, respectively. In general, nodal assortativity decreases early in cognitive decline, reflecting vulnerability, but increases later, indicating enhanced local connectivity and resilience.

Figure 4.17 reports the distribution of the nodal assortativity coefficients of selected sNET nodes across all 3 groups. Figure 4.17A reveals a significant reduction in the nodal assortativity as the severity of cognitive decline increases from SCI to MCI ($p < 0.018$), for all sNET nodes that are in the top 5 in terms of their statistical significance for SCI-MCI classification. Conversely, the top 5 sNET nodes with the highest discriminative power for MCI-vs-ADD classification show an increase from MCI to ADD ($p < 0.004$), as shown in Figure 4.17B. It is noteworthy that these two sets of nodes are mutually exclusive.

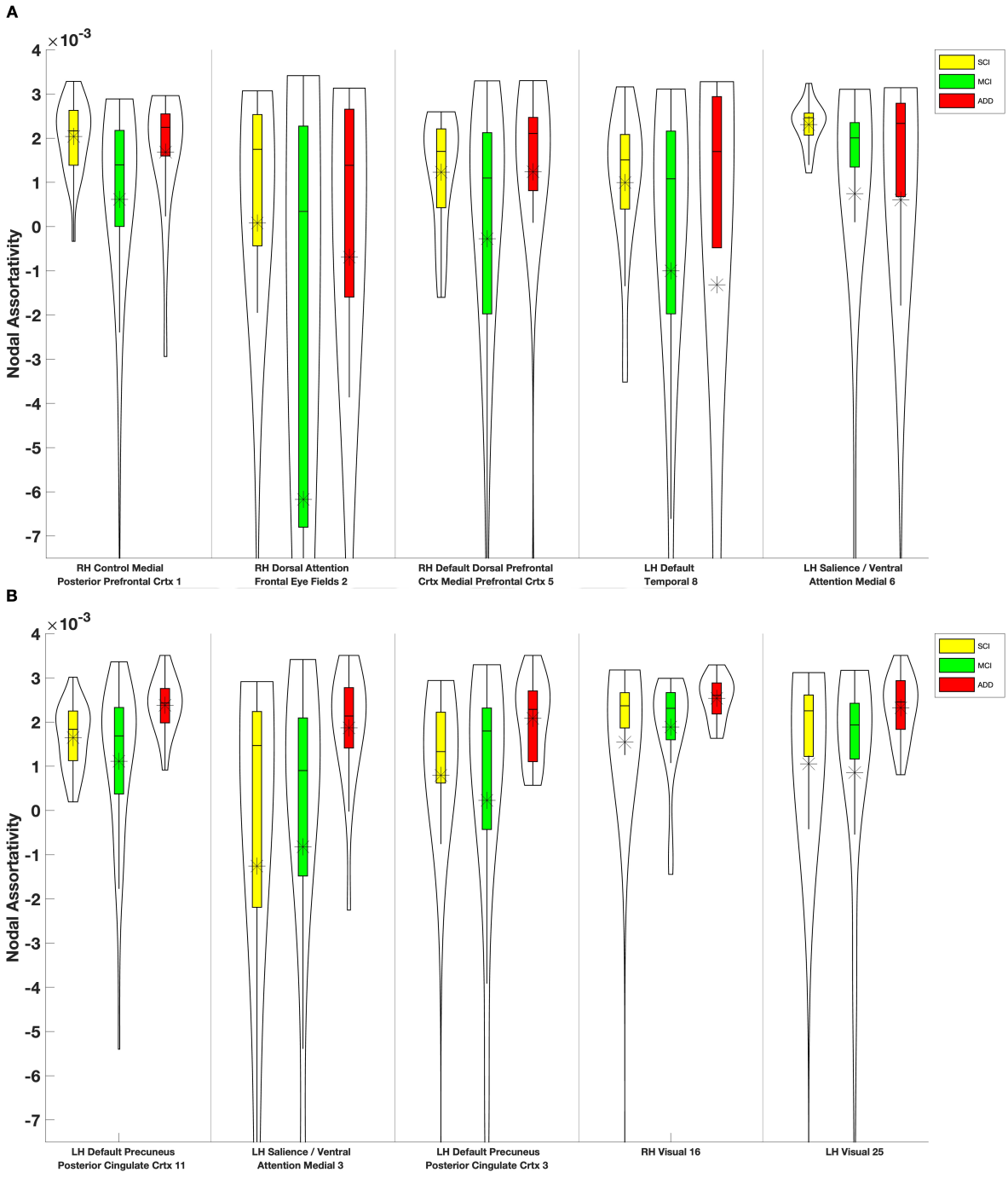

Figure 4.17. Distributions of nodal assortativity coefficients of the top 5 most discriminative sNET nodes are shown for SCI-vs-MCI ($p < 0.018$) at the top panel and for MCI-vs-ADD ($p < 0.004$) at the bottom panel. A statistically significant decrease in nodal assortativity is observed in the transition from SCI to MCI, while a statistically significant increase is observed in the transition from MCI to ADD.

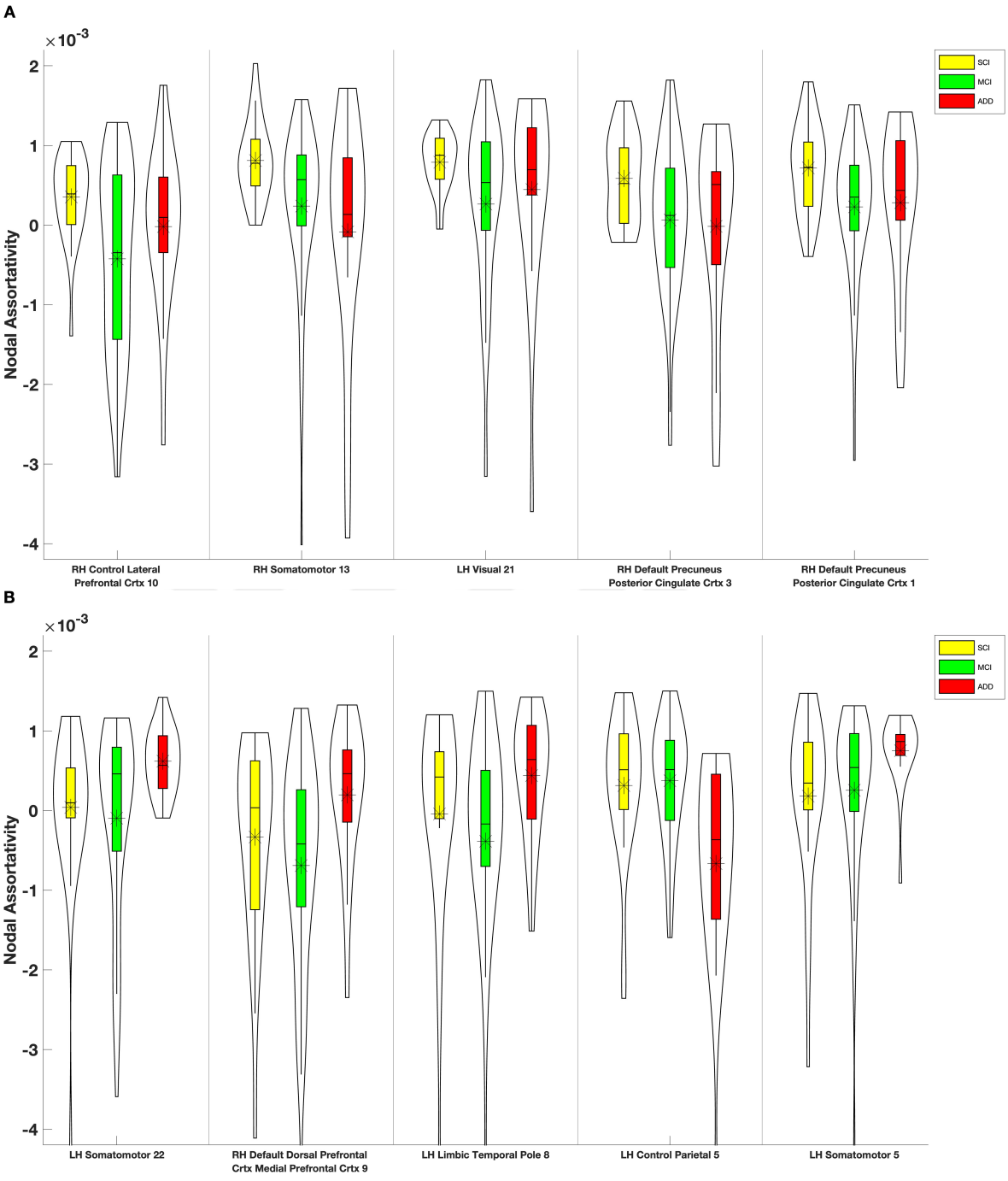

Figure 4.18. Distributions of nodal assortativity coefficients of the top 5 most discriminative fNET nodes are shown for SCI-vs-MCI ($p < 0.002$) at the top panel and for MCI-vs-ADD ($p < 0.012$) at the bottom panel. A statistically significant decrease in nodal assortativities is observed in the transition from SCI to MCI, while a statistically significant increase is observed in the transition from MCI to ADD.

Figure 4.18 reports the identical statistical analysis of nodal assortativity for fNETs. Similarly to sNETs, data in Figure 4.18A reveals a statistically significant decrease in nodal assortativity of selected fNET nodes as the severity of cognitive decline increases from SCI to MCI ($p < 0.002$). As the disease progresses from MCI to ADD, 4 of the top 5 fNET nodes again display an increasing nodal assortativity ($p < 0.012$), while one node (Control Parietal 5 in the left hemisphere) has the opposite trend, as shown in Figure 4.18B. These two sets of nodes are also mutually exclusive.

4.4. Global and Nodal Network Measures as a Diagnostic Biomarker

In order to verify the relevance of the selected nodes as potential low dimensional (hence robust) diagnostic biomarkers, we trained linear SVM classifiers and tested them separately for each classification task (SCI-vs-MCI and MCI-vs-ADD) and each connectome type (structural and functional) by using leave-one-out experiments. Since the majority of prior work focuses on SCI-vs-ADD classification, we report the classification performance on this task as well for comparison. Additionally, experiments were conducted using the full-connectome[5] (leading to 400-D feature vectors) which is also a common approach reported in literature [32]. Finally, all experiments were conducted using multiple popular nodal features within complex network analysis—including clustering coefficient (CC), betweenness centrality (BC), node strength (NS), and node degree (ND)—in addition to nodal assortativity, allowing a comprehensive comparison across these different metrics.

Table 4.4 lists the accuracy values for all the experiments conducted. The results indicate that the $5D$ feature vectors derived from a select subset of nodes are consistently superior to high-dimensional, whole network representations, irrespective of the particular network measure chosen. It is also observed that, on average, using nodal assortativity performs better than using other local network characteristics in SCI-MCI-ADD classification. Employing the nodal assortativity of the selected nodes yielded an accuracy value in the range of $0.75 - 0.90$ in all three classification tasks

[5]The experiments with a 400-D feature vector are denoted with a (*) in Table 4.4

and for both types of connectome. The results are reported in Table 4.4, together with the results obtained using the true labels.

The observed superiority of nodal assortativity is further supported by its unique ability to reveal structural shifts in connectivity that other metrics may overlook. Nodal assortativity offers a unique insight into how individual nodes adapt their connectivity in response to early neurodegeneration, as seen in the SCI to MCI transition. Unlike metrics like degree or strength, which simply measure the amount or intensity of connectivity, nodal assortativity reveals a shift in the type of connections that nodes make. A decrease in nodal assortativity, where a node begins connecting with a wider variety of nodes rather than similar ones, indeed makes that node more "vulnerable" or susceptible to overload. However, this adjustment can be advantageous for the network as a whole. By diversifying its connections, the node supports a more flexible and adaptable network structure. Although this change puts more strain on the individual node, potentially increasing its risk, it actually strengthens the overall resilience of the network by distributing connections more evenly across different regions. This shift allows the network to better handle disruptions, maintaining functionality even as certain nodes are under increased stress. Thus, while lower nodal assortativity might signal higher vulnerability for specific nodes, it can enhance the robustness and adaptability of the network as a whole. This adaptation, specific to nodal assortativity, suggests an early strategy for maintaining network robustness that is not as clearly captured by other metrics.

In MCI to ADD, In the sNET, nodal degree, strength, and clustering coefficient all decrease, reflecting a loss in structural connectivity, likely due to advancing neurodegeneration. In contrast, these same metrics increase in the fNET, which may indicate that the brain is attempting to preserve function through enhanced connectivity in the functional network. Betweenness centrality, however, decreases in both sNET and fNET, suggesting that the importance of key nodes for efficient network communication diminishes as the disease progresses. This points to a reduced ability of the network to effectively route information through central hubs. However, as assortativity rises from

MCI to ADD, it signals a shift towards homogeneity, where nodes increasingly connect to those with similar connectivity levels. This increase in assortativity indicates a consolidating network that, although more uniform, becomes less flexible and resilient. In this way, assortativity offers a unique perspective: it captures not just connection density or local group clustering but the pattern of connectivity adaptation. It reveals how the network loses its adaptability as it shifts from a diverse, flexible structure to a more rigid, homogenous one—a sign of advancing neurodegeneration that isn't as clearly reflected by other metrics alone.

Table 4.4. Linear SVM accuracies were computed for SCI-vs-MCI, MCI-vs-ADD, and SCI-vs-ADD tasks on sNETs and fNETs using $5D$ (specific node features) and $400 - D$ (full connectome) feature vectors (Nodal Assortativity/NA, Clustering Coefficient/CC, Betweenness Centrality/BC, Node Strength/NS, Node Degree/ND). † Results of random shuffling experiments are reported only for nodal assortativity.

	Task	NA	NA†	CC	BC	NS	ND
sNET	SCI-MCI	0.75 / 0.54*	0.49 / 0.54*	0.77 / 0.60*	0.73 / 0.55*	0.74 / 0.53*	0.70 / 0.56*
	MCI-ADD	0.80 / 0.50*	0.48 / 0.44*	0.66 / 0.53*	0.74 / 0.60*	0.66 / 0.55*	0.72 / 0.64*
	SCI-ADD	0.85 / 0.56*	0.54 / 0.60*	0.75 / 0.52*	0.82 / 0.52*	0.75 / 0.68*	0.78 / 0.75*
fNET	SCI-MCI	0.81 / 0.52*	0.47 / 0.48*	0.78 / 0.48*	0.78 / 0.58*	0.70 / 0.50*	0.68 / 0.53*
	MCI-ADD	0.75 / 0.46*	0.53 / 0.45*	0.65 / 0.62*	0.66 / 0.43*	0.76 / 0.57*	0.70 / 0.52*
	SCI-ADD	0.90 / 0.57*	0.41 / 0.48*	0.72 / 0.65*	0.78 / 0.45*	0.77 / 0.50*	0.72 / 0.53*

Additionally, to ensure that nodal assortativity findings are not influenced by age, we examined the correlation between age and nodal assortativity measurements across the identified nodes. In order to investigate the potential influence of age as a covariant on nodal assortativity findings, Pearson's correlation coefficient was computed between age (as an independent variable) and each of the five identified nodal assortativities (as dependent variables), and linear regression analysis was also performed. The absolute values of Pearson's correlation coefficients ranged from 0.01 to 0.30. The significance of the linear regression models was assessed using R^2 statistics and F-test p-values, with ranges of $[0.0001, 0.04]$ and $[0.08, 0.93]$, respectively. These results indicate that

the predictive power of the five nodal assortativity measurements does not show a statistically significant correlation with age. Please refer to the Appendix Table A.1 for all results.

5. DISCUSSION

The global assortativity of sNETs and fNETs exhibits a significant disparity across three distinct spatial resolutions (Schaefer 200, 400, and 800), irrespective of the clinical stage of cognitive decline, with sNETs consistently displaying higher global assortativity than fNETs. This finding aligns with existing literature, reinforcing the conclusion that the global assortativity of either sNETs or fNETs lacks sufficient discriminative power to serve as a reliable diagnostic biomarker. In contrast, the mesoscale (subnetwork) assortativity analysis offers a more nuanced approach to capturing stage-dependent alterations in network integrity within key brain regions. This level of analysis enhances the potential for tracking Alzheimer's disease progression, as it identifies more specific structural and functional disruptions that evolve with the disease.

The mesoscale analysis reveals that the changes in assortativity are not consistent across sNETs and fNETs, but vary depending on the stage of cognitive decline and the specific brain regions involved. At the Schaefer 200 scale, the Limbic network in sNET shows a decrease in assortativity as the transition from SCI to MCI. This decrease suggests a weakening in the network's ability to maintain cohesive, similarly connected nodes, which is indicative of the structural and functional disruptions occurring within the limbic network. As highlighted in previous studies, the limbic network is among the first regions to undergo degeneration in the early stages of Alzheimer's disease, playing a critical role in the disease's progression [75]. This finding aligns with the well-established role of the hippocampus and its surrounding structures in-memory processing, one of the earliest cognitive functions disrupted by Alzheimer's disease. The decreased assortativity observed in this network reflects a deterioration in network integrity, consistent with Lin et al.'s findings of significant changes in connectivity and tract-specific diffusivity in limbic connections [76]. These alterations in network cohesiveness further underscore the vulnerability of the limbic system during early-stage cognitive decline. The Salience/Ventral Attention network (SVN) shows increased assortativity during the transition from MCI to ADD in sNET.

This could indicate compensatory mechanisms, where the network becomes more integrated as a response to increasing cognitive demands, reflecting the brain's attempt to maintain function despite advancing neurodegeneration [77]. In contrast, fNET shows increased assortativity in the somatomotor network from MCI to ADD. In contrast, fNET shows increased assortativity in the Somatomotor network (SMN) during the transition from MCI to ADD, suggesting compensatory changes in motor-related brain regions as Alzheimer's disease progresses. This increase in assortativity indicates that nodes within the network are becoming more connected to similarly connected nodes, reflecting heightened internal integration. This aligns with the findings of Wang et al., who observed that centrality in the SMN increased in MCI and ADD [21]. In ADD the SMN becomes more interconnected, as indicated by the increased assortativity, suggesting a compensatory response to preserve motor function. However, this increased connectivity was found to be negatively correlated with cognitive performance, meaning that despite the network's attempt to adapt, it does not result in improved cognitive outcomes. Initially, the rise in assortativity might help support motor-related functions, but as the neurodegeneration progresses, this compensatory mechanism may become less effective, ultimately failing to protect cognitive health.

At the Schaefer 400 scale, sNET exhibits decreased assortativity in the Default Mode Network (DMN) during both the transitions from SCI to MCI and MCI to ADD, reflecting a progressive weakening of internal network connectivity. This is consistent with growing evidence that the DMN is particularly vulnerable in the early stages of Alzheimer's disease. The DMN plays a critical role in memory and self-referential thought, both of which are severely impacted as Alzheimer's progresses. In addition to the changes in nodal assortativity, previous studies have also reported disruptions in the white matter fiber tract integrity of the DMN in both MCI and ADD. For instance, Zhou et al. and Weiler et al. demonstrated that white matter tract integrity degeneration within the DMN contributes to its functional decline [78, 79]. As the white matter integrity deteriorates, the reduced assortativity observed in sNET reflects the network's diminishing ability to maintain cohesive, similarly connected nodes, further contributing to the cognitive decline seen in both MCI and AD. fNET exhibits a decreased

assortativity in the Limbic network, indicating a weakening of internal connectivity within this region, which is essential for memory processing and emotional regulation. As one of the earliest areas impacted by ADD, the Limbic network undergoes significant functional disruptions. In the MCI group, studies have shown that functional connectivity within this network is altered [80,81]. The decline in assortativity suggests that previously well-connected nodes within the network are losing their structural and functional integrity, reflecting the network's diminishing capacity to maintain cohesive interactions. This weakening of local connectivity patterns likely contributes to the cognitive and emotional impairments characteristic of ADD, particularly in its early stages

At the Schaefer 800 scale, fNET displays decreased assortativity in the SVN from SCI to MCI and the SMN from MCI to ADD. The SVN plays a critical role in detecting and adapting to salient external stimuli and internal events, which is essential for cognitive flexibility and attention regulation [77, 82]. Disruptions in this network have been observed in MCI, reflecting early-stage cognitive impairment and its effects on attention and cognitive control [83]. Similarly, the SMN shows decreased assortativity during the transition from MCI to ADD, suggesting that motor-related brain regions also experience declining functional connectivity as ADD progresses. it is clear that sensory and motor regions of the central nervous system are affected by ADD pathology and that interventions targeting amelioration of sensory-motor deficits in ADD may enhance patient function as ADD progresses [84].

The mesoscale analysis across different Schaefer scales highlights the importance of selecting an appropriate resolution for detecting network changes related to Alzheimer's disease. The Schaefer 200 scale captures broad alterations and early compensatory mechanisms, but it lacks the granularity required for the precise staging of cognitive decline. Conversely, the Schaefer 800 scale is well-suited to identifying fine-grained functional changes within specific networks but may overlook broader structural alterations crucial for understanding ADD progression. The Schaefer 400 scale, however, offers a balanced resolution, making it particularly effective for detecting both

early disruptions and late-stage declines across structural and functional networks. Its capacity to capture progressive declines in core networks, such as the DMN and Limbic network, positions it as an optimal choice for further research on ADD biomarkers.

Despite the insights gained from mesoscale analysis, our findings highlight its limitations in classification performance. While it provides valuable information on ADD progression, its discriminative power is somewhat constrained, as evidenced by the classification AUC not exceeding 0.70, as reported in Table 4.2 Moreover, the optimal scale for distinguishing between stages of cognitive decline can vary depending on specific cases, emphasizing the need for a tailored approach. Nevertheless, the proposed local (nodal) assortativity analysis revealed statistically significant differences between different stages of clinical cognitive decline, albeit at varying locations and nature for structure and function. The results in Table 4.3 further support the Schaefer 400 scale as the most optimal choice for nodal assortativity, demonstrating superior accuracy in classification outcomes.

The most significant sNET nodal assortativity changes in the first half of the clinical cognitive decline spectrum, namely from SCI to MCI states, are observed most conspicuously in the left precuneus posterior cingulate cortex (pCunPCC) in DMN, the left orbital frontal (Limbic), the right medial posterior prefrontal cortex (control network - CON), the right frontal eye fields (Dorsal Attention network - DAN), the left posterior (DAN) and in the right cingulate (CON) with a significant decrease in nodal assortativity except the last one. Ide et al. pointed out that nodes with a high relative vulnerability tend to exhibit disassortativity (decreased assortativity) [85]. Murakami et al., on the other hand, had associated decreased local assortativity with shorter (and faster) local communication paths [86]. Hence, our observations suggest that certain nodes in sNETs take over increased roles in communication, resulting in greater local vulnerability. In contrast, the most significant sNET nodal assortativity changes from MCI to ADD manifest themselves in the form of local assortativity increase. The most conspicuous regions where such an increase is observed are the left pCunPCC and right parietal (DMN), the left lateral prefrontal (CON), the left temporal pole

(Limbic), the somatomotor cortices (SMN), the midcingulate cortex (salience-ventral attention network - SVN) in the right and left hemispheres, the right lingual gyrus & cuneus, the occipitotemporal junction (visual network - VN) and the left occipital pole (VN).

These observations can be interpreted as a compensatory response to connectivity disruptions observed in MCI, in the form of alternative connections among brain regions. The increase in nodal assortativity in the temporal and frontal regions can be linked to a decrease in nodal efficiency which indicates a reduction in the efficiency of information flow, predominantly identified in the frontal and temporal lobes, as reported in literature [15]. Jones et al. suggested that the initial disruption of the posterior DMN could eventually lead to enhanced connections between the posterior DMN and other central hubs in the brain [87]. This is partially supported by our results which indicate spatially different regions undergoing local changes of different nature across the spectrum. The importance and effectiveness of tracking local changes are also supported by the high diagnostic power of the selected nodal assortativities.

Similar changes are observed in fNETs, albeit mostly in different locations than the ones in sNETs. A significant decrease in fNET nodal assortativity from SCI to MCI was most conspicuous in the bilateral pCunPCC (DMN), the left prefrontal cortex (DMN), the bilateral parietal (DMN), the right lateral prefrontal cortex (CON), the right cingulate (CON), the left & right orbital frontal (limbic), the right temporal pole (limbic), the right MCC (SVN), the right posterior (DAN), the somatomotor cortices, the right occipitotemporal junction (VN) and the left cuneus (VN). It should be noted that fNETs are models of correlative function. Hence, this decrease in nodal fNET assortativity, which is a wider spread phenomenon compared to that of sNETs in the first half of the spectrum, is not necessarily indicative of an increase in local vulnerability but, rather, may be the result of a functional re-organization of the brain where certain nodes start orchestrating function. A possible explanation, in parallel with the explanation suggested for the local assortativity decreases from SCI to MCI, is that few new subnetworks may have been built. These findings are also in agreement

with the loss of functional connectivity in DMN and the bilateral orbital frontal cortex within the limbic network [81,88]. The nodal assortativity increase from MCI to ADD, on the other hand, is spatially more limited. This increase is most conspicuous in the right dorsal prefrontal cortex medial prefrontal cortex (DMN), the left prefrontal cortex (DMN), the right & left orbital frontal (limbic), the left temporal pole (limbic), and the right & left lateral prefrontal cortex (PFCl) (CON), the left frontal operculum insula (SVN) and the lateral & somatomotor cortices, accompanied by a nodal assortativity decrease in the left parietal (CON). The increase in nodal assortativity within the temporal pole can potentially be due to increased functional connectivity in this region reported for ADD [89]. The observed increase in assortativity in the prefrontal cortex, which is in agreement with prior findings reported in the literature, suggests that ADD may be making an effort to enhance prefrontal connectivity in order to sustain cognitive efficiency in the face of limited DMN resources [88]. In the transition from MCI to ADD, increased assortativity within the Visual Network in both sNET and fNET may reflect a compensatory mechanism, stabilizing connectivity in less affected regions to support overall network resilience under neurodegenerative stress. Yu et al. indicate that the visual network is among the final regions to experience neurodegenerative effects in Alzheimer's progression, underscoring its relative preservation in structure and function as the disease unfolds [90].

Irrespective of the underlying topological changes in brain connectome (network) organization, it is clear that the brain's structural topology and functional organization undergo local changes in spatially segregated regions across the clinical cognitive decline spectrum. The change is consistent with the stage of the cognitive decline, but spatially different in different stages and (to a great extent) between structure and function. The observed spatial differences in sNETs and fNETs should be interpreted with caution as these two types of connectomes represent different aspects of brain organization. While the observations in sNETs can be attributed to local topology and communication efficiency, the observations in fNETs are more likely to be associated with the functional organization, eg. in terms of functional units.

These findings highlight that local network measures, particularly nodal assortativity, offer distinctive insights into the progression of cognitive decline and have greater diagnostic strength than global measures across various stages of neurodegeneration. Local measures demonstrate higher diagnostic accuracy than whole-network (400-D) analyses at different stages of disease. As shown in Table 4.4, local measures consistently surpass whole-network approaches in terms of diagnostic precision. Among all local measures, the nodal (local) assortativity is the single measure with a strong discriminative power across the clinical cognitive decline spectrum. Hence, although other measures can capture certain changes in certain stages of cognitive decline, nodal assortativity singles out as a potentially powerful measure for not only diagnosis but also disease progress monitoring.

6. CONCLUSION

Clinical cognitive decline, leading to Alzheimer's Disease Dementia (ADD), has long been considered as a disconnection syndrome manifesting itself in the structural and functional brain organization. Despite the evidence in literature with regard to significant changes in (primarily functional) brain connectome models, these efforts have not yet provided a coherent insight into underlying mechanisms, nor offered strong biomarkers. We investigated changes in local structural and functional reorganization of the brain at different stages of clinical cognitive decline, using local (nodal) assortativity as a quantitative measure. We observed statistically significant local reorganization of the brain that not only varies with the progress of the cognitive condition but also differs in nature between structure and function that manifested in the form of spatially varying hyper and hypo-assortativity in sNETs and fNETs.

In the early stages of cognitive decline (from SCI to MCI), hypo-assortativity suggests that certain brain regions are becoming more functionally and structurally isolated, indicating an increased vulnerability to disconnection as these regions struggle to maintain their original connectivity patterns. In the sNET, hypo-assortativity is especially notable in nodes within the Control Network and the Default Mode Network (DMN), where this reduction may weaken these networks' resilience to neurodegenerative effects. The DMN, responsible for memory and self-referential thought, is frequently impacted in Alzheimer's, contributing to memory impairment even in the early stages. Lower DMN assortativity within sNET can reflect a failure in the ability of the network to integrate information, which can cause memory and self-awareness disturbances. In the fNET, hypo-assortativity is prominent across nodes in the DMN, Control Network, and Limbic Network. The Control Network, which is essential for executive functions like attention and decision-making, may experience decreased assortativity, impacting cognitive regulation and aligning with symptoms such as decreased attention and impaired judgment in early Alzheimer's stages. Meanwhile, the Limbic Network, which supports memory processing and emotional regulation, also shows re-

duced assortativity in fNET, indicating a possible weakening of these emotional and memory-related pathways. This reduction in assortativity within these networks suggests a shift in nodal roles, with individual nodes diversifying their connections beyond similar nodes. While this reorganization may improve local communication efficiency via shorter paths, it also comes at the potential expense of network robustness and adaptability as nodes move away from more cohesive, specialized connectivity. Specifically, in the DMN, Control, and Limbic Networks in fNET, reduced assortativity may reflect an adaptive reorganization of roles that, although it potentially enhances local efficiency, could make these nodes more susceptible to overload, ultimately compromising the overall resilience of the network.

Conversely, in the later stages (transitioning from MCI to ADD), hyper-assortativity suggests an adaptive reorganization wherein nodes increasingly connect with other similarly connected nodes. This trend may represent an attempt to create a more cohesive but rigid network structure, particularly in regions such as the DMN and somatomotor networks, where heightened assortativity could help stabilize connectivity as neurodegeneration advances. The somatomotor regions, which govern sensory and motor processing, often show compensatory connectivity increases in later stages of Alzheimer's, reflecting attempts to maintain motor coordination and sensory processing. However, this consolidation of connectivity patterns also reduces the flexibility of the network, as the reliance on internally consistent homogeneous connectivity diminishes the ability of the network to dynamically adapt to further changes. This increase in assortativity may initially serve as a compensatory mechanism, preserving function by relying on robust, similarly connected nodes. However, it ultimately limits its adaptability and can contribute to a decrease in network flexibility as the disease progresses.

In both sNET and fNET, particularly during the AD-MCI transition, an increase in assortativity within the Visual Network is also notable, although vision is generally not affected by Alzheimer's disease. This increase in assortativity may suggest compensatory reorganization in the Visual Network as it adapts to broader neurodegenerative

changes occurring in other networks. As Alzheimer's affects interconnected networks responsible for cognition, memory, and executive function, the Visual Network may adapt by reinforcing connectivity among similarly connected nodes, increasing its assortativity. This phenomenon could imply that the Visual Network is attempting to stabilize its structure to maintain functionality as other networks deteriorate. By forming more cohesive, homogeneous connections, the Visual Network may be compensating for the reduced efficiency or reliability in surrounding networks, preserving cognitive and sensory processing as the disease progresses. Thus, this increase in assortativity might not directly relate to visual function but rather reflect the larger effort of the brain to maintain functional stability under neurodegenerative stress.

Reorganization is more prominent in function in the early stages and in structure in the later stages. Despite some common regions that undergo both structural and functional reorganization, a significant variation in regions affected from functional and structural perspectives was observed. It is imperative to emphasize the significance of analyzing both spatial and temporal dimensions to achieve a comprehensive understanding of the clinical cognitive decline leading to Alzheimer's Disease. Our preliminary findings suggest a complex and variable (non-monotonous) reorganization that may hint at simultaneously active degenerative and compensatory mechanisms. Further research from such a multi-dimensional perspective on a larger dataset, and ideally with follow-up data, has the potential to provide an alternative picture of the brain's reorganization during the course of cognitive decline.

REFERENCES

1. Chowdhary, N., C. Barbui, K. J. Anstey, M. Kivipelto, M. Barbera, R. Peters, L. Zheng, J. Kulmala, R. Stephen, C. P. Ferri, Y. Joanette, H. Wang, A. Comas-Herrera, C. Alessi, K. Suharya (Dy), K. J. Mwangi, R. C. Petersen, A. A. Motala, S. Mendis, D. Prabhakaran, A. Bibi Mia Sorefan, A. Dias, R. Gouider, S. Shahar, K. Ashby-Mitchell, M. Prince and T. Dua, "Reducing the Risk Of Cognitive Decline and Dementia: Who Recommendations", *Frontiers in Neurology*, Vol. 12, 2022.

2. Gaugler, J., B. James, T. Johnson, J. Reimer, M. Solis, J. Weuve, R. F. Buckley and T. J. Hohman, "2022 Alzheimer's Disease Facts and Figures", *Alzheimer's & Dementia*, Vol. 18, No. 4, pp. 700–789, 2022.

3. Nichols, E., C. E. Szoeke, S. E. Vollset, N. Abbasi, F. Abd-Allah, J. Abdela, M. T. E. Aichour, R. O. Akinyemi, F. Alahdab, S. W. Asgedom *et al.*, "Global, Regional, and National Burden of Alzheimer's Disease and Other Dementias, 1990–2016: A Systematic Analysis for the Global Burden of Disease Study 2016", *The Lancet Neurology*, Vol. 18, No. 1, pp. 88–106, 2019.

4. Conceição, S. d. S., D. S. B. d. Carvalho, J. E. T. Batista, A. O. Lyrio, E. S. Souza, P. J. d. S. d. Matos, A. M. Hintz, S. S. d. Cruz, I. S. Gomes-Filho and A. C. M. G. Figueiredo, "Temporal Trends in Mortality from Alzheimer's Disease in Federal District, Brazil: An Ecological Study (2010–2018)", *International Journal of Environmental Research and Public Health*, Vol. 20, No. 18, p. 6713, 2023.

5. Breijyeh, Z. and R. Karaman, "Comprehensive Review on Alzheimer's Disease: Causes and Treatment", *Molecules*, Vol. 25, No. 24, p. 5789, 2020.

6. Hanseeuw, B. J., R. A. Betensky, H. I. L. Jacobs, A. P. Schultz, J. Sepulcre, J. A. Becker, D. M. O. Cosio, M. Farrell, Y. T. Quiroz, E. C. Mormino *et al.*, "Association of Amyloid and Tau with Cognition in Preclinical Alzheimer's Disease:

A Longitudinal Study", *JAMA Neurology*, Vol. 76, No. 8, pp. 915–924, 2019.

7. Alirezaei, Z., M. H. Pourhanifeh, S. Borran, M. Nejati, H. Mirzaei and M. Hamblin, "Neurofilament Light Chain as a Biomarker, and Correlation with Magnetic Resonance Imaging in Diagnosis of CNS-Related Disorders", *Molecular Neurobiology*, Vol. 57, No. 1, pp. 469–491, 2020.

8. Delbeuck, X., M. Van der Linden and F. Collette, "Alzheimer's Disease as a Disconnection Syndrome?", *Neuropsychology Review*, Vol. 13, pp. 79–92, 2003.

9. Buckner, R. L., A. Z. Snyder, B. J. Shannon, G. LaRossa, R. Sachs, A. F. Fotenos, Y. I. Sheline, W. E. Klunk, C. A. Mathis, J. C. Morris *et al.*, "Molecular, Structural, and Functional Characterization of Alzheimer's Disease: Evidence for a Relationship Between Default Activity, Amyloid, and Memory", *Journal of Neuroscience*, Vol. 25, No. 34, pp. 7709–7717, 2005.

10. Sporns, O., G. Tononi and R. Kötter, "The Human Connectome: A Structural Description of the Human Brain", *PLOS Computational Biology*, Vol. 1, No. 4, p. e42, 2005.

11. Le Bihan, D., J.-F. Mangin, C. Poupon, C. A. Clark, S. Pappata, N. Molko and H. Chabriat, "Diffusion Tensor Imaging: Concepts and Applications", *Journal of Magnetic Resonance Imaging: An Official Journal of the International Society for Magnetic Resonance in Medicine*, Vol. 13, No. 4, pp. 534–546, 2001.

12. Van Essen, D. C., K. Ugurbil, E. Auerbach, D. Barch, T. E. Behrens, R. Bucholz, A. Chang, L. Chen, M. Corbetta, S. W. Curtiss *et al.*, "The Human Connectome Project: A Data Acquisition Perspective", *NeuroImage*, Vol. 62, No. 4, pp. 2222–2231, 2012.

13. Xia, M., J. Wang and Y. He, "BrainNet Viewer: A Network Visualization Tool for Human Brain Connectomics", *PLoS ONE*, Vol. 8, No. 7, p. e68910, 2013.

14. Sporns, O., "Structure and Function of Complex Brain Networks", *Dialogues in clinical neuroscience*, Vol. 15, No. 3, pp. 247–262, 2013.

15. Lo, C.-Y., P.-N. Wang, K.-H. Chou, J. Wang, Y. He and C.-P. Lin, "Diffusion Tensor Tractography Reveals Abnormal Topological Organization in Structural Cortical Networks in Alzheimer's Disease", *Journal of Neuroscience*, Vol. 30, No. 50, pp. 16876–16885, 2010.

16. Reijmer, Y. D., A. Leemans, K. Caeyenberghs, S. M. Heringa, H. L. Koek, G. J. Biessels, U. V. C. I. S. Group *et al.*, "Disruption of Cerebral Networks and Cognitive Impairment in Alzheimer's Disease", *Neurology*, Vol. 80, No. 15, pp. 1370–1377, 2013.

17. Tzourio-Mazoyer, N., B. Landeau, D. Papathanassiou, F. Crivello, O. Etard, N. Delcroix, B. Mazoyer and M. Joliot, "Automated Anatomical Labeling of Activations in SPM Using a Macroscopic Anatomical Parcellation of the MNI MRI Single-Subject Brain", *NeuroImage*, Vol. 15, No. 1, pp. 273–289, 2002.

18. Coninck, J. C. P., F. A. S. Ferrari, A. S. Reis, K. C. Iarosz, I. L. Caldas, A. M. Batista and R. L. Viana, "Network Properties of Healthy and Alzheimer's brains", *Physica A: Statistical Mechanics and Its Applications*, Vol. 547, p. 124475, 2020.

19. Fischer, F. U., D. Wolf, A. Scheurich, A. Fellgiebel, A. D. N. Initiative *et al.*, "Altered Whole-Brain White Matter Networks in Preclinical Alzheimer's Disease", *NeuroImage: Clinical*, Vol. 8, pp. 660–666, 2015.

20. Pereira, J. B., D. Van Westen, E. Stomrud, T. O. Strandberg, G. Volpe, E. Westman and O. Hansson, "Abnormal Structural Brain Connectome in Individuals with Preclinical Alzheimer's Disease", *Cerebral Cortex*, Vol. 28, No. 10, pp. 3638–3649, 2018.

21. Wang, T., F. Shi, Y. Jin, P.-T. Yap, C.-Y. Wee, J. Zhang, C. Yang, X. Li, S. Xiao

and D. Shen, "Multilevel Deficiency of White Matter Connectivity Networks in Alzheimer's Disease: A Diffusion MRI Study with DTI and HARDI Models", *Neural Plasticity*, Vol. 2016, pp. 1–12, 2016.

22. John, M., T. Ikuta and J. Ferbinteanu, "Graph Analysis of Structural Brain Networks in Alzheimer's Disease: Beyond Small World Properties", *Brain Structure and Function*, Vol. 222, pp. 923–942, 2017.

23. Supekar, K., V. Menon, D. Rubin, M. Musen and M. D. Greicius, "Network Analysis of Intrinsic Functional Brain Connectivity in Alzheimer's Disease", *PLOS Computational Biology*, Vol. 4, No. 6, p. e1000100, 2008.

24. Sanz-Arigita, E. J., M. M. Schoonheim, J. S. Damoiseaux, S. A. R. B. Rombouts, E. Maris, F. Barkhof, P. Scheltens and C. J. Stam, "Loss of 'Small-World' Networks in Alzheimer's Disease: Graph Analysis of fMRI Resting-State Functional Connectivity", *PLOS ONE*, Vol. 5, No. 11, p. e13788, 2010.

25. Zhao, X., Y. Liu, X. Wang, B. Liu, Q. Xi, Q. Guo, H. Jiang, T. Jiang and P. Wang, "Disrupted Small-World Brain Networks in Moderate Alzheimer's Disease: A Resting-State fMRI Study", *PLOS ONE*, Vol. 7, No. 3, p. e33540, 2012.

26. Liu, Z., Y. Zhang, H. Yan, L. Bai, R. Dai, W. Wei, C. Zhong, T. Xue, H. Wang, Y. Feng *et al.*, "Altered Topological Patterns of Brain Networks in Mild Cognitive Impairment and Alzheimer's Disease: A Resting-State fMRI Study", *Psychiatry Research: Neuroimaging*, Vol. 202, No. 2, pp. 118–125, 2012.

27. Xiang, J., H. Guo, R. Cao, H. Liang and J. Chen, "An Abnormal Resting-state Functional Brain Network Indicates Progression towards Alzheimer's Disease", *Neural regeneration research*, Vol. 8, No. 30, pp. 2789–2799, 2013.

28. Li, Y., Y. Qin, X. Chen and W. Li, "Exploring the Functional Brain Network of Alzheimer's Disease: Based on the Computational Experiment", *PLOS ONE*,

Vol. 8, No. 9, p. e73186, 2013.

29. Luo, Y., T. Sun, C. Ma, X. Zhang, Y. Ji, X. Fu and H. Ni, "Alterations of Brain Networks in Alzheimer's Disease and Mild Cognitive Impairment: A Resting State fMRI Study Based on a Population-Specific Brain Template", *Neuroscience*, Vol. 452, pp. 192–207, 2021.

30. Filippi, M., S. Basaia, E. Canu, F. Imperiale, G. Magnani, M. Falautano, G. Comi, A. Falini and F. Agosta, "Changes in Functional and Structural Brain Connectome along the Alzheimer's Disease Continuum", *Molecular Psychiatry*, Vol. 25, No. 1, pp. 230–239, 2020.

31. Yıldırım, Z., F. Delen, D. Berron, H. Baumeister, G. Ziegler, H. Schütze, W. Glanz, L. Dobisch, O. Peters, S. Freiesleben, L. Schneider, J. Priller, E. Spruth, A. Schneider, K. Fliessbach, J. Wiltfang, B. Schott, D. Meiberth, K. Buerger and E. Duzel, "Brain Reserve Contributes to Distinguishing Preclinical Alzheimer's Stages 1 and 2", *Alzheimer's Research & Therapy*, Vol. 15, p. 43, 2023.

32. Schouten, T. M., M. Koini, F. de Vos, S. Seiler, M. de Rooij, A. Lechner, R. Schmidt, M. van den Heuvel, J. van der Grond and S. A. R. B. Rombouts, "Individual Classification of Alzheimer's Disease with Diffusion Magnetic Resonance Imaging", *NeuroImage*, Vol. 152, pp. 476–481, 2017.

33. Ebadi, A., J. L. Dalboni da Rocha, D. B. Nagaraju, F. Tovar-Moll, I. Bramati, G. Coutinho, R. Sitaram and P. Rashidi, "Ensemble Classification of Alzheimer's Disease and Mild Cognitive Impairment Based on Complex Graph Measures from Diffusion Tensor Images", *Frontiers in Neuroscience*, Vol. 11, p. 56, 2017.

34. Khazaee, A., A. Ebrahimzadeh and A. Babajani-Feremi, "Identifying Patients with Alzheimer's Disease Using Resting-state fMRI and Graph Theory", *Clinical Neurophysiology*, Vol. 126, No. 11, pp. 2132–2141, 2015.

35. Schaefer, A., R. Kong, E. M. Gordon, T. O. Laumann, X.-N. Zuo, A. J. Holmes, S. B. Eickhoff and B. T. T. Yeo, "Local-Global Parcellation of the Human Cerebral Cortex from Intrinsic Functional Connectivity MRI", *Cerebral Cortex*, Vol. 28, No. 9, pp. 3095–3114, 2017.

36. Tench, C., P. Morgan, M. Wilson and L. Blumhardt, "White matter mapping using diffusion tensor MRI", *Magnetic Resonance in Medicine: An Official Journal of the International Society for Magnetic Resonance in Medicine*, Vol. 47, No. 5, pp. 967–972, 2002.

37. Yüksel Dal, D., Z. Yıldırım, H. Gürvit, A. Kabakçıoğlu and B. Acar, "Reorganization of brain connectivity across the spectrum of clinical cognitive decline", *Neurological Sciences*, Vol. 45, No. 12, pp. 5719–5730, 2024.

38. Fonov, V., A. Evans, K. Botteron, C. Almli, R. Mckinstry and L. Collins, "Unbiased average age-appropriate atlases for pediatric studies", *NeuroImage*, Vol. 54, No. 1, pp. 313–327, 2011.

39. "Preprocessing Pipeline", https://vavlab.boun.edu.tr/brainet-structural-and-functional-brain-network-analysis, 2019, accessed on September 6, 2024.

40. "FSL Toolbox", `https://fsl.fmrib.ox.ac.uk/fsl/fslwiki/FSL`, 2019, accessed on September 6, 2024.

41. "FreeSurfer Toolbox", `https://surfer.nmr.mgh.harvard.edu/`, 2019, accessed on September 6, 2024.

42. "Tortoise Toolbox", `https://tortoise.nibib.nih.gov/`, 2019, accessed on September 6, 2024.

43. Glasser, M. F., S. N. Sotiropoulos, J. A. Wilson, T. S. Coalson, B. Fischl, J. L. Andersson, J. Xu, S. Jbabdi, M. Webster, J. R. Polimeni *et al.*, "The Minimal Preprocessing Pipelines for the Human Connectome Project", *NeuroImage*, Vol. 80,

pp. 105–124, 2013.

44. "Human Connectome Project Pipeline Scripts", `https://github.com/Washington-University/HCPpipelines`, 2019, accessed on September 6, 2024.

45. Greve, D. N. and B. Fischl, "Accurate and Robust Brain Image Alignment Using Boundary-Based Registration", *NeuroImage*, Vol. 48, No. 1, pp. 63–72, 2009.

46. "Recon-all steps", `https://surfer.nmr.mgh.harvard.edu/fswiki/recon-all`, 2024, accessed on September 6, 2024.

47. Smith, S. M. and J. M. Brady, "SUSAN—a New Approach to Low Level Image Processing", *International Journal of Computer Vision*, Vol. 23, No. 1, pp. 45–78, 1997.

48. Yeo, B. T., F. M. Krienen, J. Sepulcre, M. R. Sabuncu, D. Lashkari, M. Hollinshead, J. L. Roffman, J. W. Smoller, L. Zöllei, J. R. Polimeni, B. Fischl, H. Liu and R. L. Buckner, "The Organization of The Human Cerebral Cortex Estimated by Intrinsic Functional Connectivity", *Journal of Neurophysiology*, Vol. 106, No. 3, pp. 1125–1165, 2011.

49. Tillem, S., K. Harenski, C. Harenski, J. Decety, D. Kosson, K. A. Kiehl and A. Baskin-Sommers, "Psychopathy is Associated with Shifts in the Organization of Neural Networks in a Large Incarcerated Male Sample", *NeuroImage: Clinical*, Vol. 24, p. 102083, 2019.

50. Kucyi, A., M. Esterman, J. Capella, A. Green, M. Uchida, J. Biederman, J. D. Gabrieli, E. M. Valera and S. Whitfield-Gabrieli, "Prediction of Stimulus-Independent and Task-unrelated Thought from Functional Brain Networks", *Nature Communications*, Vol. 12, No. 1, p. 1793, 2021.

51. Huang, X., D. Lu, D. M. Ricciuto, P. J. Hanson, A. D. Richardson, X. Lu, E. Weng,

S. Nie, L. Jiang, E. Hou, I. F. Steinmacher and Y. Luo, "A Model-Independent Data Assimilation (MIDA) Module and its Applications in Ecology", *Geoscientific Model Development*, Vol. 14, No. 8, pp. 5217–5238, 2021.

52. Vandewouw, M. M., J. Brian, J. Crosbie, R. J. Schachar, A. Iaboni, S. Georgiades, R. Nicolson, E. Kelley, M. Ayub, J. Jones, M. J. Taylor, J. P. Lerch, E. Anagnostou and A. Kushki, "Identifying Replicable Subgroups in Neurodevelopmental Conditions Using Resting-state Functional Magnetic Resonance Imaging Data", *JAMA Network Open*, Vol. 6, No. 3, pp. e232066–e232066, 2023.

53. "Schaefer Atlas Github", `https://github.com/ThomasYeoLab/CBIG/tree/master/stable_projects/brain_parcellation/Schaefer2018_LocalGlobal`, accessed on September 6, 2024.

54. Westin, C.-F., S. Maier, H. Mamata, A. Nabavi, F. Jolesz and R. Kikinis, "Processing and Visualization of Diffusion Tensor MRI", *Medical Image Analysis*, Vol. 6, No. 2, pp. 93–108, 2002.

55. Moyer, D., B. A. Gutman, J. Faskowitz, N. Jahanshad and P. M. Thompson, "Continuous Representations of Brain Connectivity Using Spatial Point Processes", *Medical Image Analysis*, Vol. 41, pp. 32–39, 2017.

56. Bowman, F. D., L. Zhang, G. Derado and S. Chen, "Determining Functional Connectivity using fMRI Data with Diffusion-Based Anatomical Weighting", *NeuroImage*, Vol. 62, No. 3, pp. 1769–1779, 2012.

57. Lim, S., F. Radicchi, M. P. van den Heuvel and O. Sporns, "Discordant Attributes of Structural and Functional Brain Connectivity in a Two-Layer Multiplex Network", *Scientific Reports*, Vol. 9, No. 1, p. 2885, 2019.

58. Tibshirani, R., "Regression Shrinkage and Selection via the Lasso", *Journal of the Royal Statistical Society Series B: Statistical Methodology*, Vol. 58, No. 1, pp.

267–288, 1996.

59. Hoerl, A. E. and R. W. Kennard, "Ridge Regression: Biased Estimation for Nonorthogonal Problems", *Technometrics*, Vol. 12, No. 1, pp. 55–67, 1970.

60. Barabási, A.-L. and R. Albert, "Emergence of Scaling in Random Networks", *Science*, Vol. 286, No. 5439, pp. 509–512, 1999.

61. Watts, D. J. and S. H. Strogatz, "Collective Dynamics of 'Small-World' Networks", *Nature*, Vol. 393, No. 6684, pp. 440–442, 1998.

62. Bullmore, E. and O. Sporns, "Complex Brain Networks: Graph Theoretical Analysis of Structural and Functional Systems", *Nature Reviews Neuroscience*, Vol. 10, No. 3, pp. 186–198, 2009.

63. Rubinov, M. and O. Sporns, "Complex Network Measures of Brain Connectivity: Uses and Interpretations", *NeuroImage*, Vol. 52, No. 3, pp. 1059–1069, 2010.

64. Freeman, L. C., "Centrality in Social Networks Conceptual Clarification", *Social Networks*, Vol. 1, No. 3, pp. 215–239, 1978.

65. Newman, M. E., "Assortative Mixing in Networks", *Physical Review Letters*, Vol. 89, No. 20, p. 208701, 2002.

66. Thedchanamoorthy, G., M. Piraveenan, D. Kasthuriratna and U. Senanayake, "Node Assortativity in Complex Networks: An Alternative Approach", *Procedia Computer Science*, Vol. 29, pp. 2449–2461, 2014.

67. Albert, M., S. DeKosky, D. Dickson, B. Dubois, H. Feldman, N. Fox, A. Gamst, D. Holtzman, W. Jagust, R. Petersen, P. Snyder, M. Carrillo, B. Thies and C. Phelps, "The Diagnosis of Mild Cognitive Impairment due to Alzheimer's Disease: Recommendations from the National Institute on Aging-Alzheimer's Association Workgroups on Diagnostic Guidelines for Alzheimer's Disease", *Alzheimer's*

& Dementia: The Journal of the Alzheimer's Association, Vol. 7, pp. 270–279, 2011.

68. Buschke, H., "Selective Reminding for Analysis of Memory and Learning", *Journal of Verbal Learning and Verbal Behavior*, Vol. 12, No. 5, pp. 543–550, 1973.

69. Grober, E., A. Sanders, C. Hall and R. Lipton, "Free and Cued Selective Reminding Identifies Very Mild Dementia in Primary Care", *Alzheimer Disease and Associated Disorders*, Vol. 24, pp. 284–290, 2010.

70. McKhann, G., D. Knopman, H. Chertkow, B. Hyman, C. Jack, C. Kawas, W. Klunk, W. Koroshetz, J. Manly, R. Mayeux, R. Mohs, J. Morris, M. Rossor, P. Scheltens, M. Carrillo, B. Thies, S. Weintraub and C. Phelps, "The Diagnosis of Dementia due to Alzheimer's Disease: Recommendations from the National Institute on Aging-Alzheimer's Association Workgroups on Diagnostic Guidelines for Alzheimer's Disease", *Alzheimer's & Dementia: The Journal of the Alzheimer's Association*, Vol. 7, pp. 263–269, 2011.

71. Li, C., J. Neugroschl, X. Luo, C. Zhu, P. Aisen, S. Ferris and M. Sano, "The Utility of the Cognitive Function Instrument (CFI) to Detect Cognitive Decline in Non-Demented Older Adults", *Journal of Alzheimer's Disease*, Vol. 60, pp. 1–11, 2017.

72. Jack, C. R., D. S. Knopman, W. J. Jagust, L. M. Shaw, P. S. Aisen, M. W. Weiner, R. C. Petersen and J. Q. Trojanowski, "Hypothetical Model of Dynamic Biomarkers of the Alzheimer's Pathological Cascade", *The Lancet Neurology*, Vol. 9, No. 1, pp. 119–128, 2010.

73. Villemagne, V. L., S. Burnham, P. Bourgeat, B. Brown, K. A. Ellis, O. Salvado, C. Szoeke, S. L. Macaulay, R. Martins, P. Maruff *et al.*, "Amyloid β Deposition, Neurodegeneration, and Cognitive Decline in Sporadic Alzheimer's Disease: a Prospective Cohort Study", *The Lancet Neurology*, Vol. 12, No. 4, pp. 357–367,

2013.

74. Teghipco, A., "BrainSurfer", , 2022, `https://zenodo.org/record/7271544`, accessed on September 6, 2024.

75. Braak, H. and E. Braak, "Neuropathological Staging of Alzheimer-related Changes", *Acta Neuropathologica*, Vol. 82, No. 4, pp. 239–259, 1991.

76. Lin, S.-Y., C.-P. Lin, T.-J. Hsieh, C.-F. Lin, S.-H. Chen, Y.-P. Chao, Y.-S. Chen, C.-C. Hsu and L.-W. Kuo, "Multiparametric Graph Theoretical Analysis Reveals Altered Structural and Functional Network Topology in Alzheimer's Disease", *NeuroImage: Clinical*, Vol. 22, p. 101680, 2019.

77. Seeley, W. W., V. Menon, A. F. Schatzberg, J. Keller, G. H. Glover, H. Kenna, A. L. Reiss and M. D. Greicius, "Dissociable Intrinsic Connectivity Networks for Salience Processing and Executive Control", *Journal of Neuroscience*, Vol. 27, No. 9, pp. 2349–2356, 2007.

78. Zhou, B., X. Dou, W. Wang, H. Yao, F. Feng, P. Wang, Z. Yang, N. An, B. Liu, X. Zhang and Y. Liu, "Structural and Functional Connectivity Abnormalities of the Default Mode Network in Patients with Alzheimer's Disease and Mild Cognitive Impairment within Two Independent Datasets", *Methods*, Vol. 205, pp. 29–38, 2022.

79. Weiler, M., B. M. de Campos, M. H. Nogueira, B. P. Damasceno, F. Cendes and M. L. F. Balthazar, "Structural Connectivity of the Default Mode Network and Cognition in Alzheimer's Disease", *Psychiatry Research: Neuroimaging*, Vol. 223, No. 1, pp. 15–22, 2014.

80. Cai, S., T. Chong, Y. Peng, W. Shen, J. Li, K. M. von Deneen, L. Huang and A. D. N. Initiative, "Altered Functional Brain Networks in Amnestic Mild Cognitive Impairment: A Resting State fMRI Study", *Brain Imaging and Behavior*,

Vol. 11, pp. 619–631, 2017.

81. Badhwar, A., A. Tam, C. Dansereau, P. Orban, F. Hoffstaedter and P. Bellec, "Resting-state Network Dysfunction in Alzheimer's Disease: A Systematic Review and Meta-analysis", *Alzheimer's & Dementia: Diagnosis, Assessment & Disease Monitoring*, Vol. 8, pp. 73–85, 2017.

82. Menon, V., "Developmental Pathways to Functional Brain Networks: Emerging Principles", *Trends in Cognitive Sciences*, Vol. 17, No. 12, pp. 627–640, 2013.

83. Brier, M. R., J. B. Thomas, A. Z. Snyder, T. L. Benzinger, D. Zhang, M. E. Raichle, D. M. Holtzman, J. C. Morris and B. M. Ances, "Loss of Intranetwork and Internetwork Resting State Functional Connections with Alzheimer's Disease Progression", *Journal of Neuroscience*, Vol. 32, No. 26, pp. 8890–8899, 2012.

84. Albers, M. W., G. C. Gilmore, J. Kaye, C. Murphy, A. Wingfield, D. A. Bennett, A. L. Boxer, A. S. Buchman, K. J. Cruickshanks, D. P. Devanand *et al.*, "At the Interface of Sensory and Motor Dysfunctions and Alzheimer's Disease", *Alzheimer's & Dementia*, Vol. 11, No. 1, pp. 70–98, 2015.

85. Ide, K., H. Sato, T. Quang and A. Namatame, "Risk Diffusion Modeling and Vulnerability Quantification on Japanese Human Mobility Network from Complex Network Analysis Point of View", *International Journal of Advanced Computer Science and Applications*, Vol. 7, No. 2, 2016.

86. Murakami, M., S. Ishikura, D. Kominami, T. Shimokawa and M. Murata, "Robustness and Efficiency in Interconnected Networks with Changes in Network Assortativity", *Applied Network Science*, Vol. 2, pp. 1–21, 2017.

87. Jones, D. T., D. S. Knopman, J. L. Gunter, J. Graff-Radford, P. Vemuri, B. F. Boeve, R. C. Petersen, M. W. Weiner and C. R. Jack Jr, "Cascading Network Failure Across the Alzheimer's Disease Spectrum", *Brain*, Vol. 139, No. 2, pp.

547–562, 2016.

88. Agosta, F., M. Pievani, C. Geroldi, M. Copetti, G. B. Frisoni and M. Filippi, "Resting State fMRI in Alzheimer's Disease: Beyond the Default Mode Network", *Neurobiology of Aging*, Vol. 33, No. 8, pp. 1564–1578, 2012.

89. Qi, Z., Y. An, M. Zhang, H.-J. Li and J. Lu, "Altered Cerebro-Cerebellar Limbic Network in AD Spectrum: A Resting-state fMRI Study", *Frontiers in Neural Circuits*, Vol. 13, p. 72, 2019.

90. Yu, M., O. Sporns and A. J. Saykin, "The Human Connectome in Alzheimer's Disease—Relationship to Biomarkers and Genetics", *Nature Reviews Neurology*, Vol. 17, No. 9, pp. 545–563, 2021.

APPENDIX A: AGE EFFECTS ON NODAL ASSORTATIVITY ACROSS COGNITIVE STAGES

The statistical analysis examines age as a covariate in relation to nodal assortativity within sNET and fNET across the stages of clinical cognitive decline, from SCI to MCI and MCI to ADD. Linear regression and Pearson's correlation analyses were applied to determine whether age significantly influences assortativity values at key nodes.

Table A.1. Linear regression and Pearson's correlation analysis results for the relationship between age and assortativity in sNET and fNET, comparing SCI vs MCI and MCI vs ADD.

		Node name	**R-squared**	**p-value**	**r**	β
sNET	**SCI-MCI**	RH_Cont_PFCmp_1	0.01	0.39	-0.10	-1.59±0.07
		RH_DorsAttn_FEF_2	0.04	0.08	-0.20	-1.46±0.06
		RH_Default_PFCdPFCm_5	0.004	0.70	-0.04	-1.20±0.06
		LH_Default_Temp_8	0.01	0.51	-0.07	-1.38±0.10
		LH_SalVentAttn_Med_6	0.002	0.81	-0.02	-0.8±0.06
	MCI-ADD	LH_Default_pCunPCC_11	0.03	0.14	0.18	1.34±0.13
		LH_SalVentAttn_Med_3	0.03	0.15	0.17	1.33±0.13
		LH_Default_pCunPCC_3	0.04	0.09	0.16	1.21±0.11
		RH_Vis_16	0.0005	0.85	0.02	0.76±0.15
		LH_Vis_25	0.0079	0.48	0.08	0.68±0.16
fNET	**SCI-MCI**	RH_Cont_PFCl_10	0.0001	0.93	-0.01	-1.21±0.044
		RH_SomMot_13	0.04	0.08	-0.30	-0.90±0.042
		LH_Vis_21	0.0071	0.48	0.08	-1.00±0.043
		RH_Default_pCunPCC_3	0.02	0.15	-0.17	-0.89±0.043
		RH_Default_pCunPCC_1	0.01	0.38	0.10	-1.04±0.043
	MCI-ADD	LH_SomMot_22	0.008	0.45	0.09	1.37±0.079
		RH_Default_PFCdPFCm_9	0.006	0.52	-0.08	1.16±0.144
		LH_Limbic_TempPole_8	0.02	0.15	0.15	1.27±0.128
		LH_Cont_Par_5	0.03	0.11	-0.19	-1.06±0.079
		LH_SomMot_5	0.01	0.28	-0.13	1.23±0.074

The results, summarized in Table A.1, reveal generally low R-squared values and non-significant p-values across nodes in both sNET and fNET, indicating no statistically significant correlation between age and nodal assortativity. Thus, age appears to have a negligible effect on assortativity changes, supporting the view that observed patterns in nodal assortativity are more directly related to disease progression than to age.